Classification and origin of vein-related Cu-Ag-Pb-Zn mineralization at Salkeld Lake, Nonacho Basin, Northwest Territories, Canada

By Anna Terekhova

A thesis submitted to Saint Mary's University, Halifax, Nova Scotia in partial fulfillment of the requirements for the Degree of Master of Science in Applied Science

November 29th, 2021, Halifax, Nova Scotia

Approved: Dr. Jacob Hanley
Supervisor
Department of Geology
Saint Mary's University

Approved: Dr. Erin Adlakha
Supervisory Committee
Department of Geology
Saint Mary's University

Approved: Dr. Robert Singer
Supervisory Committee
Department of Chemistry
Saint Mary's University

Approved: Mr. Hendrik Falck
Supervisory Committee
Government of Northwest Territories

Approved: Dr. Stefanie Brueckner
External Reviewer
Department of Earth Sciences
University of Manitoba

November 29, 2021

Table of Contents

Abstract

Classification and origin of vein-related Cu-Ag-Pb-Zn mineralization at Salkeld Lake, Nonacho Basin, Northwest Territories, Canada

By Anna Terekhova

The Paleoproterozoic Nonacho Basin, Northwest Territories, Canada, contains a variety of poorly characterized mineral deposits, including hydrothermal Cu-Ag-(Pb-Zn) mineralization with one of the most representative examples at Salkeld Lake. The mineralization occurs in breccias, veins and disseminations within fracture networks and shear zones, cross-cutting granitic gneiss, metasedimentary rocks and alkali granitoids. Utilizing a variety of bulk and microanalytical methods, this study provides the first genetic constraints for, and a classification of, the mineralization at Salkeld Lake.

The results of fluid inclusion and stable O isotope analyses of quartz and calcite suggest mixing, dilution and oxidation of a carbonic-aqueous mineralizing fluid by the introduction of cooler meteoric water, which led to metal precipitation. End-stage mineralizing conditions were at near surface P and T ~150-180 ^{o}C. The Cu-Ag-(Pb-Zn) mineralization formed at ~1831 ± 2 Ma (laser Ar-Ar of pre- to syn-mineralization muscovite) and is classified as an intrusion-related, sediment-hosted vein- and breccia-related Cu-Ag-(Pb-Zn) deposit. Possible heat and metal sources are the calc-alkalic mafic Sparrow Dykes or related magmatic events, timed with the waning stages of Trans-Hudson Orogen (~2.0-1.8 Ga).

November 29, 2021

Acknowledgements

I would like to first of all thank my supervisor Dr. Jacob Hanley for not only providing me with incredible research opportunities to grow and evolve as a scientist but also for putting trust in me to endure the trying world of academia. His wisdom, guidance, immense patience and kind understanding made the inevitable difficulties, failures and challenges of research bearable and, most importantly, educational. I would also like to thank the members of my committee Dr. Erin Adlakha, Dr. Robert Singer and Mr. Hendrik Falck for all their help throughout the thesis. I also want to separately thank Dr. Mitch Kerr for noticing my interest in, and affinity for, geology early on and luring me into the department with fancy samples; Dr. Erin Adlakha for inspiring me to pursue a career in academia and for being a great role model; Mr. Hendrik Falck for teaching me the ropes in the field and keeping it cool in the face of imminent danger posed by my questionable boating skills. I would like to acknowledge and thank the Government of Northwest Territories for their help, support and funding, and for allowing me to take part in the multidisciplinary research, as well as interact and work alongside fantastic scientists.

I want to thank my best friends Isobel and Grace, who stuck with me through thick and thin, for being the closest thing to sisters I will ever have. And last but not least, I am eternally grateful to my wonderful family: my parents, for giving me a shot at a better life, for supporting my every decision and for their unconditional love. My partner's family, Julie, Dale and Aaron, for accepting me so easily and treating me like their own. My fiancé Alex, for all the unforgettable experiences, silly jokes and sweet moments, and of course, for inspiring me to be a better person, to never doubt myself and always strive for greater

things in life. I am extremely fortunate to have all these people in my life, without whom this work would not have been completed.

List of Figures

In Chapter 2

In Chapter 4

List of Tables in Appendices

Chapter 1: Introduction

1.1 Thesis structure and objectives

This thesis consists of six chapters: Chapter 1 contains a brief overview of the study and its structure, research goals and objectives and an introduction to deposits hosted in intracratonic basins globally and in Canada. Chapter 2 details the regional and local geological setting, as well as the exploration history of the study area. Chapter 3 describes the methods utilized throughout the study (geochemistry, petrography, fluid inclusion and stable O and S isotope analyses and geochronology) to characterize the Cu-Ag-(Pb-Zn) mineralization. Chapter 4 is dedicated to the results of the study, whereas Chapter 5 discusses the development of a paragenetic sequence, constrains the fluid evolution and possible metal and fluid sources, and timing of the mineralized system; it concludes with a classification of the style of mineralization. Chapter 6 lists the main conclusions and proposes future work that would aid in further understanding the origin of proposed "hybrid-type" intrusion-related sediment-hosted Cu-Ag-(Pb-Zn) occurrences in the study area and similar environments globally.

Data were obtained using a combination of analytical techniques including bulk rock geochemistry, petrography, SEM-EDS and electron microprobe analysis, LA-ICP-MS, hot cathode cathodoluminescence, fluid inclusion microthermometry, stable isotope analysis, and Re-Os and laser Ar-Ar geochronology.

1.2 List of Abbreviations

Abbreviation	Definition
BSE	backscattered electron
cal	calcite
carb	carbonic fluid composed of dominantly CO_2
CL	cathodoluminescence
DDH	diamond drill hole
EPMA	electron probe micro-analyzer
FI	fluid inclusion
FIA	fluid inclusion assemblage
LA-ICP-MS	laser ablation inductively-coupled plasma mass spectrometry
L_{aq}	aqueous liquid phase
L_{carb}	carbonic liquid phase
polymetallic	in this study, Cu-Ag-(Pb-Zn)
SIMS	secondary ion mass spectrometry
SSC	sediment-hosted stratiform copper
Th_{total}	homogenization temperature of a fluid inclusion
Th_{carb}	homogenization temperature of a carbonic phase
T_m^{ice}	final ice melting temperature
T_m^{clath}	final clathrate melting temperature
V_{aq}	vapour (aqueous)
V_{carb}	carbonic vapour
V-CDT	Vienna Canyon Diablo Troilite

V-PDB	Vienna Pee Dee Belemnite
V-SMOW	Vienna Standard Mean Ocean Water
wt %	weight percentage
wt % NaCl eq.	fluid inclusion bulk salinity in weight percentage NaCl equivalent

1.3 Intracratonic basin-related mineral deposits

Intracratonic sedimentary basins (e.g., Parana, Brazil; Michigan Basin, USA; Hudson Basin, Canada; Salamat Basin, Central African Republic; Chad Basin, Chad; Allen & Armitage, 2012; Daly et al., 2018; Kyser, 2007) occur in the anorogenic domains of cratons, at a significant distance from the craton margin extending across hundreds of kilometers. They are typically circular to oval-shaped shallow sags located on relatively thick stretches of the continental lithosphere, and characterized by subsidence, depression below original crustal level and relatively thick packages of preserved strata (Southard, 2007; Burgess et al., 2019). Intracratonic basins show a wide range in size, age distribution (from Proterozoic to Cretaceous) and subsidence rates. Geodynamically and tectonically the formation of the sag basins remains poorly understood, although the timing of the formation is broadly coeval with global plate tectonics, specifically, continental accretion and break-up i.e., the Wilson Cycle (Middleton, 1989; Allen & Armitage, 2012; Allen, 2015). The sediment fill consists of shallow-water cratonal sediments, including shales, sandstones and carbonates, with a distinction made between terrigenous basins, dominated by continental clastics, and marine, carbonate-dominated basins (Selley, 2015). Basinal processes including heat and fluid flow, global and local-scale tectonic and magmatic events can create favourable settings for metal

precipitation (Deb & Pal, 2015; Kyser, 2007), as well as formation of oil and gas reservoirs, dominantly in shallow marine, carbonate-dominated basins. Rifting in a basinal setting allows for deeper hydrothermal circulation due to greater subsidence and lower basal heat flow, which can promote the formation of large mineral deposits (Hoggard et al., 2020).

The mineral deposit types most commonly associated with the intracratonic sedimentary basins include:

Unconformity-type uranium deposits that often occur below, along or above the unconformable contact between an Archean to Paleoproterozoic crystalline basement with highly reducing lithological units and oxidized siliciclastic sediments (red beds) of Proterozoic age (le Roux, 1982; Cuney, 2005). Unconformity type deposits make up for 25% of all global uranium production (IAEA, 2018). Examples include the deposits in the Athabasca Basin (Canada) and Yeneena Basin (Western Australia).

Mississippi Valley-Type deposits which account for 24% of the global resources of Pb and Zn in sediment- and volcanic-hosted deposits (Leach et al., 2010). It is a major class of ore deposits characterized by large concentrations of sphalerite, galena and iron sulfides, commonly stratabound and stratiform, hosted in carbonate rocks (Paradis et al., 2007). Examples include Pine Point (Canada), Upper Silesia (Poland), and the Viburnum Trend and Old Lead Belt (USA).

Bedded-sedimentary barite deposits that are found in the intracratonic basins within sedimentary successions that typically contain organic-rich shale, mudstone, or chert. They often occur as stratiform bodies of massive or near-massive barite, and can

be interbedded with sulfides (Maynard, 1991; Robinson, 1992, Hutchinson, 1983). E.g.: Tom and Jason deposits in the Selwyn basin (northwestern Canada), the Meggen and Rammelsberg deposits (Germany), and the Ballynoe and Silvermines deposits (Ireland) (Johnson et al., 2017).

Sediment-hosted stratabound deposits which are characterized by disseminated sandstone uranium, sandstone lead and stratiform-hosted copper in marine, lacustrine and continental rocks at or near a redox boundary (Hutchinson, 1983; Bell, 1996; Liu et al., 2017; Cheng, 2020). Recent studies show the global distribution of giant sediment-hosted base metal deposits within intracratonic basins is linked to the transition between the thick and thin lithosphere (Hoggard et al., 2020). Examples include the Washakie Basin, Green River Basin sandstone uranium deposits in Wyoming (USA); Songliao Basin (NE China), and the Kupferschiefer Cu-Ag deposits (Poland) (Oszczepalski et al., 2019).

Other types of deposits found in intracratonic basins include fluorite, banded iron formation and variety of minor quartz vein-hosted, polymetallic deposits (Hutchinson, 1983).

Basin formation may take over a hundred million years, tied to the tectonics and rifting (McKenzie, 1978; Allen, 2015; Selley, 2015). The longevity of sedimentary basins and their permeability (in particular the upper crustal faulted layers, creating fluid pathways) allows for a variety of depositional processes to occur. The complexity of these metal-bearing systems depends on the underlying magmatism that prevails in anorogenic continental rift settings (Winter, 2001), tectonic processes, lithology and fluid interactions (Kyser, 2007).

1.4 Motivation and goal of study

Proterozoic intracratonic sedimentary basins have received increased attention from the mineral resources industry and academic researchers alike due to their high potential to host economically viable deposits of metals and metalloids recently deemed critical priorities by the Canadian federal government (e.g., Zn, U, Cu, In, Sn). In Canada, several intracratonic basins host world-class hydrothermal mineral deposits. These include deposits within the Thelon Basin, Nunavut (e.g., Kiggavik, Bong and Andrew Lake unconformity-related U deposits: Sharpe et al., 2015; Shabaga et al., 2017, 2020, 2021), Athabasca Basin, Saskatchewan (e.g., Rabbit Lake, Millenium, Centennial and McArthur River unconformity-related U deposits: Hoeve & Sibbald, 1978; Tremblay, 1982; Kotzer & Kyser, 1990; Ruzicka, 1996; Jefferson et al., 2007; Alexandre et al., 2005, 2009, 2012; Tuncer et al., 2006; Cloutier et al., 2009; Richard et al., 2010; Ng et al., 2013; Kyser, 2014); Wernecke Basin, Yukon (e.g., Wernecke Breccia IOCG deposit: Bell, 1986; Hunt, 2004; Hunt et al., 2005; Blende carbonate-hosted polymetallic Ag–Pb–Zn deposit: Turner & Long, 2008; Moroskat, 2015), and Selwyn Basin, Yukon (e.g., sedimentary-exhalative deposits: Tom and Jason Late Devonian Zn–Pb–Ba deposits; Magnall et al., 2016; Sack et al., 2017; Howards Pass; Gadd et al., 2016).

A relatively lesser characterized basin in terms of mineral deposit potential is the Paleoproterozoic (~1.9-1.83 Ga; Neil, 2021) Nonacho Basin, Northwest Territories, Canada. The focus of a recent multidisciplinary mapping project funded by the Government of Northwest Territories is to provide new understanding of the basin evolution, including the timing and genesis of mineralization styles. The Nonacho Basin is known to host a variety of mineral commodities, including U and Cu-Ag deposits, and

for the latter, few studies are available that attempted to classify their deposit style. Additionally, there are currently no genetic models that elucidate the probable fluid, metal and heat sources responsible for the Cu-Ag-(Pb-Zn) mineralization.

Copper deposits containing the metal association Cu-Ag are relatively common within intracratonic basins. Such deposits are most commonly considered part of the broader sediment-hosted, stratiform copper (SSC) family of deposits (Kirkham, 1996). These formed coincident with major tectonic events namely the break-up of supercontinents Rodinia in late Proterozoic and Pangea in Permian, creating extensive rift basins with thick sedimentary and evaporitic sequences (Brown, 1997; Hitzman et al. 2010). They contain red beds, which are abundant in Paleoproterozoic rocks (age of the Nonacho Basin). Two main sub-types of SSC are distinguished, known as Kupferschiefer-type and red bed-type deposits, with examples including the Kupferschiefer, central Europe (Wagner, 2009; Sawlowicz, 2018; Oszczepalski et al., 2005, 2019; Mikulski et al., 2019); the Central African Copper Belt (Schneider et al., 2007; Haest et al., 2009); and the Redstone Copperbelt, NWT, Canada (Milton, 2015). These deposits are characterized by the occurrence of disseminated sulfides at redox fronts involving anoxic (marine or lacustrine) rocks within the continental red-beds, often overlying evaporitic sequences. Another related deposit type, volcanic redbed-type Cu deposits, occur in fault-bound subaerial volcanic rocks, commonly flood basalts, but can also occur in island-arc related rhyolites, characterized by a simple mineralogy consisting of disseminated Cu, minor Ag and an apparent lack of Fe-sulfides (Kirkham, 1996). Volcanic-redbed Cu deposits include those in the Coppermine River area (Kindle, 1972; Carriere & Kirkham, 1993) and Natkusiak Formation, Victoria Island, Northwest Territories

(Canada), the native Cu and Cu sulfide of the Keweenaw Peninsula, Michigan (White, 1968; Weege & Pollack, 1972), Cu sulfide deposits at Mamainse Point, Ontario (Canada) (Richards & Spooner, 1989), and native copper mineralization at Mont Alexandre, Quebec (Canada) (Cabral & Beaudoin, 2007). Lastly, there are the enigmatic Messina-type Cu deposits (Sawkins, 1977; Sawkins & Rye, 1987) that have a magmatic lineage, and are hosted in gneiss and folded granulite-facies metasediments.

This study employs petrography, mineral and whole rock geochemistry, fluid inclusion microthermometry, stable O and S isotope analysis and Ar-Ar/ Re-Os geochronology to characterize an unclassified Cu-Ag-(Pb-Zn) mineralization locality at Salkeld Lake, within the Salkeld sub-basin (Aspler, 1985) of the Nonacho Basin, NWT. The study develops a first genetic model for this style of mineralization, applicable to the broader Nonacho basin and beyond. In particular, the study resolves several uncertainties, including ambiguity about fluid and metal/S sources, and the absolute timing and triggers for deposit formation.

Chapter 2: Geological setting

2.1 Regional geology

The Nonacho Basin is an intracratonic molassoid strike-slip sedimentary basin of early Paleoproterozoic age (1.90-1.83 Ga; Bostock, 1992, 1994, 2013; Neil, 2021) located on the western edge of the Rae domain, in the northwestern Churchill Structural Province, NWT, Canada. The Churchill Province (Figure 2.1) is comprised of 2.0-1.75 Ga Meso- to Neo-Archean rocks reworked by the early assembly of Laurentia, and is bound by Taltson-Thelon orogen to the west and Trans-Hudson orogen to the east-southeast. The Churchill Province is divided into the Rae and Hearne domains by the Snowbird tectonic zone (~1.9 Ga), a belt of medium to high-grade metamorphic rocks, stretching for approximately 2800 km (Berman et al., 2007, 2013; Rainbird, 2010; Thiessen et al., 2020). This collision is presumed to be an accretionary stage of Hudsonian Orogeny (pre-1.865 Ga phase), and globally coincides with the early stages of accretion and amalgamation of Laurentia and the supercontinent Nuna (Zhao et al., 2004; Rainbird, 2010).

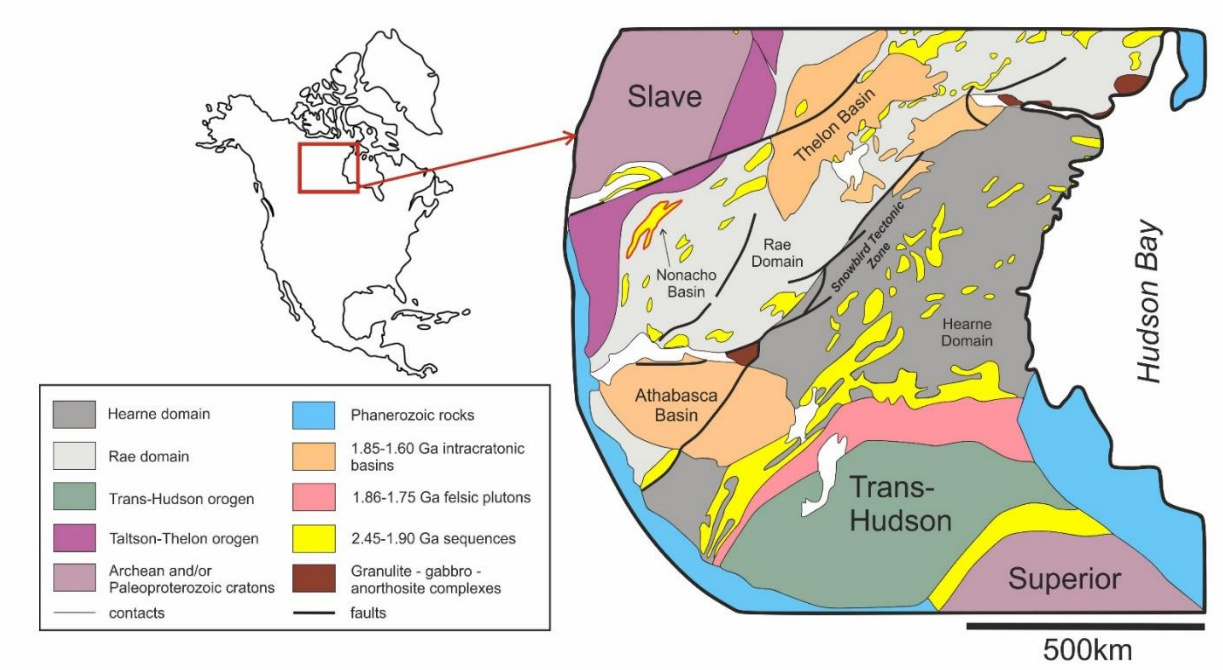

Figure 2.1: Simplified regional geology of the western Churchill Province, Canadian Shield, NWT, Canada, showing the location of the Nonacho basin within the Rae domain. Modified after Rainbird et al. (2010).

The Rae domain, located in the western part of the Churchill Province is comprised of mainly Meso- to Neoarchean granitoid gneisses (amphibolite to granulite facies), overlain by volcano-sedimentary sequences (2.9-2.63 Ga; 2.45-1.75 Ga) and intruded by granitic magma suites at 1.83 to 1.75 Ga (Berman et al., 2010). The Rae domain has been shaped and deformed by numerous orogenies and magmatic events between 2.70 and 1.80 Ga: Arrowsmith Orogeny (2.5-2.3 Ga), Buffalo Head Terrane (2.4-2.0 Ga), Thelon Tectonic Zone (2.07-1.96 Ga, 1.92-1.89 Ga), Taltson Magmatic Zone (3.2-3.0 Ga basement, 1.98-1.92 Ga metamorphism and magmatism), Trans-Hudson Orogeny (2.0-1.8 Ga) and Trans-Hudson-related Snowbird Orogeny (1.90-1.86 Ga) separating the Rae from the Hearne domain (Kellet, 2020; Regis, 2021). In particular, 1.95-1.78 Ga collisional orogenesis associated with the Trans-Hudson events endowed the Nuna interior in the Rae domain with a diversity of mineral deposits: volcanogenic massive sulfide (VMS), orogenic gold, sediment-hosted exhalative Pb-Zn, intrusion-related Au-Cu, basinal Cu-U and REE deposit-systems (Peterson & van Breeman, 1999; Peterson et al., 2002; Gandhi et al., 2005; Pehrsson et al., 2015).

Globally, the tectono-metamorphic events that shaped the Rae domain coincide with the accretion and break-up of ancient supercontinents (i.e., Nuna; Zhao et al., 2002). At 1.83-1.82 Ga the western Churchill Province underwent a period of extensive brittle to brittle–ductile deformation that resulted in the formation of trans-tensional basins and dyke emplacement, related to an east-west stress regime attributed to the accretion of the Nahanni-Fort Simpson Terrane to the west and terminal collision in the Trans-Hudson Orogen to the east (Ashton et al., 2009). Regional magmatism is represented by the presence of multiple igneous formations across the Churchill Province. The Christopher

Island Formation of the Baker Lake basin hosts ultrapotassic rocks that extend across the Snowbird zone and are implied to be emplaced at 1.83 Ga (Cousens et al., 2001).

Figure 2.2 (following page): Geology of the Nonacho Basin, showing sedimentary units, major contacts, faults and mineral showings, differentiated by principal commodity (inset). Modified after Aspler (1986) and NORMIN (2018). Main map shows location of the Salkeld Lake deposit (this study) and the Crest deposit, another significant Cu-Ag showing.

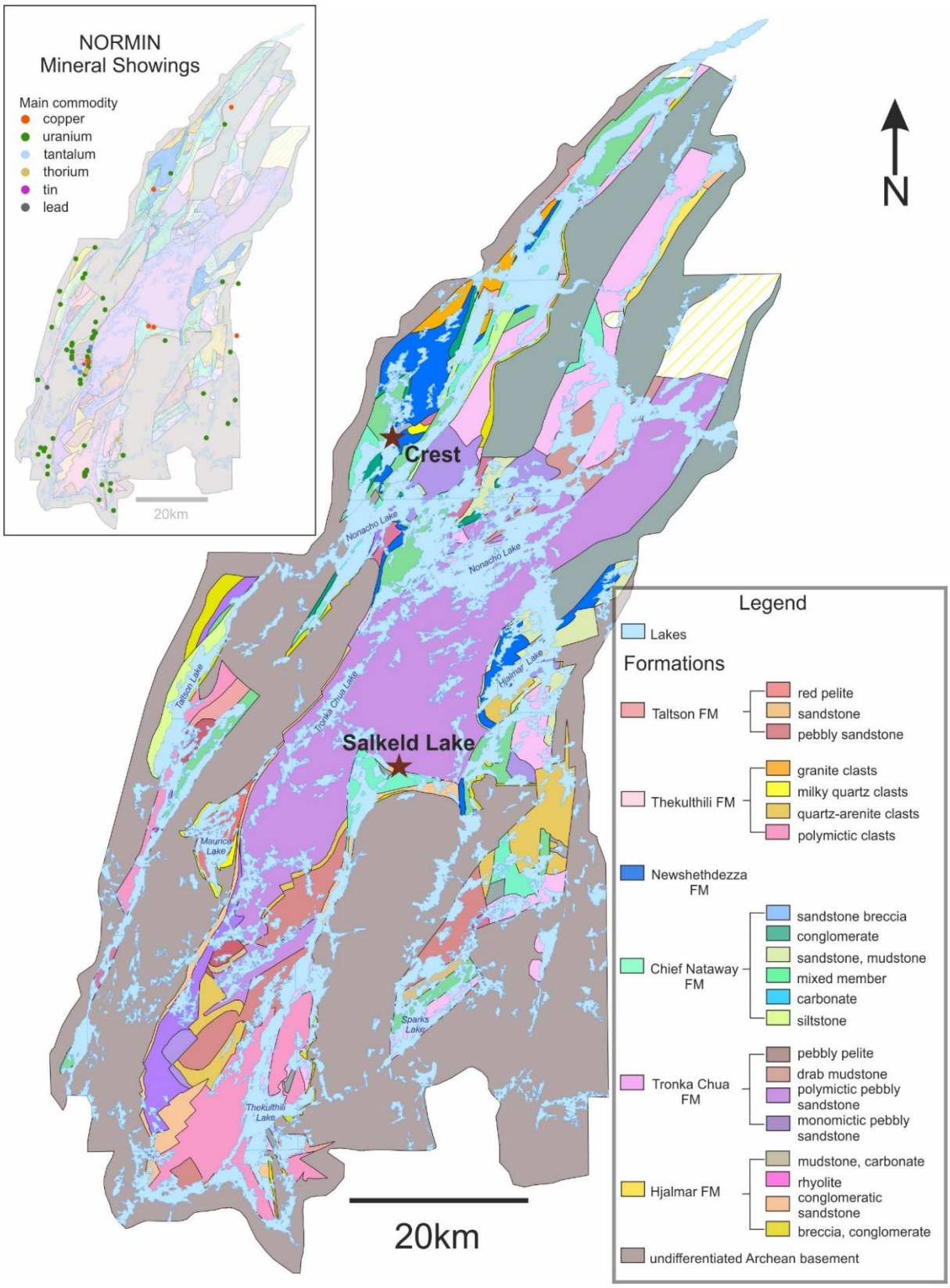
NORMIN
Mineral Showings
Main commodity
copper
uranium
tantalum
thorium
tin
lead
20km
N
Crest
Salkeld Lake
Nonacho Lake
Nonacho Lake
Taltson Lake
Tronka Chua Lake
Hjalmar Lake
Maunce Lake
Sparks Lake
Thekulthili Lake
20km
Legend
Lakes
Formations
Taltson FM
red pelite
sandstone
pebbly sandstone
Thekulthili FM
granite clasts
milky quartz clasts
quartz-arenite clasts
polymictic clasts
Newshethdezza FM
Chief Nataway FM
sandstone breccia
conglomerate
sandstone, mudstone
mixed member
carbonate
siltstone
Tronka Chua FM
pebbly pelite
drab mudstone
polymictic pebbly sandstone
monomictic pebbly sandstone
Hjalmar FM
mudstone, carbonate
rhyolite
conglomeratic sandstone
breccia, conglomerate
undifferentiated Archean basement

Nonacho Group sedimentary rocks unconformably overlay an erosional surface of Archean and early Proterozoic basement gneisses and granitoids. The basin is thought to have formed from foreland molasse, attributed to the Trans-Hudson Orogen. The paleo-setting was interpreted to be that of alluvial fans, braided streams, delta fans, beaches (Aspler, 1985). Sedimentary sequence was differentiated and split into 6 formations, from youngest to oldest: Hjalmar, Tronka Chua, Chief Nataway, Newshethdezza, Thekulthili and Taltson Formation, and the deposition occurred under cool, wet conditions with brief dry periods (Aspler, 1985). Map of the Nonacho Basin (Figure 2.2) illustrates the sedimentary sequences and their spatial association with the basement and intrusive units. Recent reappraisal of the basin (Ielpi, 2021) provides evidence of marine flooding and marine sediments indicators (wave- and bimodal-ripple, hummocky-cross, and flaser stratification), therefore the origin of the Nonacho Group Sediments is now considered not entirely terrestrial, as previously thought. The basin is divided into wedge- and rhomb- and rectangular-shaped sub-basins, (i.e., MacInnis, Taltson, Sparks, Naskethey, Salkeld) associated with, and separated by, basement uplift; sub-basins are believed to have developed in the sinistral strike-slip movement. North-northeast trending fault system extends from south of Athabasca Lake to the northern Nonacho. Within the Nonacho Basin, continental clastic succession of conglomerates, sandstones and mudstones are metamorphosed to lower greenschist facies and are intruded at 1.827 by Sparrow mafic dykes (Jerome Lake, southern Nonacho), and 1.813 Ga Thekulthili granitic stock (Bostock et al., 1992, 1994).

The Nonacho Basin is a frontier, poorly-studied area (initial mapping completed in 1985 by L. Aspler), located approximately 240 km east-southeast of Yellowknife, and is

known to host a variety of polymetallic (i.e., Cu-Ag-U-Pb-Zn) occurrences that have not been characterized.

Uranium is the major commodity in the basin, however, Ta, Th, Sn and Pb showings are identified as well. Table 1 summarizes all the identified mineral showings in the Nonacho Basin, characterized by their principal commodity and host lithologies. Significant concentration of U occurrences is found along the western margin of the basin, specifically around Maurice, MacInnis and Taltson lakes, as illustrated in the inset of the Nonacho Basin map (Figure 2.2). Several U showings in the basin (KULT-82, Hope, Cole) are being characterized and share many characteristics (mineralogy, alteration, geochemistry) with a metasomatic alkali-iron calcic-style deposit (Landry, 2020). Copper showings are less abundant in the basin, though disseminated chalcopyrite and bornite are found at U showings in minor concentrations. Salkeld Lake (central Nonacho Basin), Crest (North of the Nonacho Lake) and Ugly Lake (Eastern part of the Basin) are the major occurrences reported in the basin, though this project's focus is dedicated mostly to Salkeld Lake.

2.2 Local geology

The Salkeld Lake sub-basin is located approximately in the central part of the Nonacho Basin and is bound by two major faults. The study area shows exposures of Archean gneissic basement, overlain unconformably by metamorphosed sandstones (i.e., meta-arkoses) and of the Tronka Chua and pelites of the Chief Nataway Formations, which are partially intruded by younger alkali red granitoid (Christopher, 1993).

The mineralization at Salkeld post-dates granitic gneisses, arkoses and granitoid units, exposed at the outcrops and trenches (Figure 2.3). The area is divided into two

mineralized zones, first mentioned by Goad and Webb (1988), and then continuously referred to as shear-hosted and stockwork in the following reports by Webb (1989) and Christopher (1993, 1994), respectively. Both zones expose the aforementioned host rocks, where the mineralization is manifested in three distinct styles: fracture-hosted disseminations, vug infillings and breccias. Several faults have been mapped by Christopher in 1993, though during the field season of 2019 their exact location and relationship with the units was not identified. Exposed rocks show evidence of extensive quartz veining comprising several quartz generations, silification and epidotization (Christopher, 1993; field observations, this study). Areas with evident shearing (mostly granitic gneiss) are truncated and separated by zones of incohesive, unfoliated quartz-sulfide breccias. Surficial weathering of sulfides is manifested as malachite and azurite staining, pervasive across the trenches and outcrops, and overprints the main sulfide mineralization. Unlike other mineral showings in the Nonacho Basin (KULT-82, Hope, Crest), the Salkeld Lake deposit lacks iron oxides – no mention of hematite and magnetite appears in the reports and no evidence of these minerals was observed in the field or thin sections.

Figure 2.3 (following page): Local geology, outcrops and DDH collar locations at the Salkeld Lake deposit. Areas containing mineralized zones and trenches are highlighted, with sample numbers for surface samples collected from each zone indicated. DDH core samples came from holes with collars labelled in bold font in the mapped area. Modified after Christopher (1993).

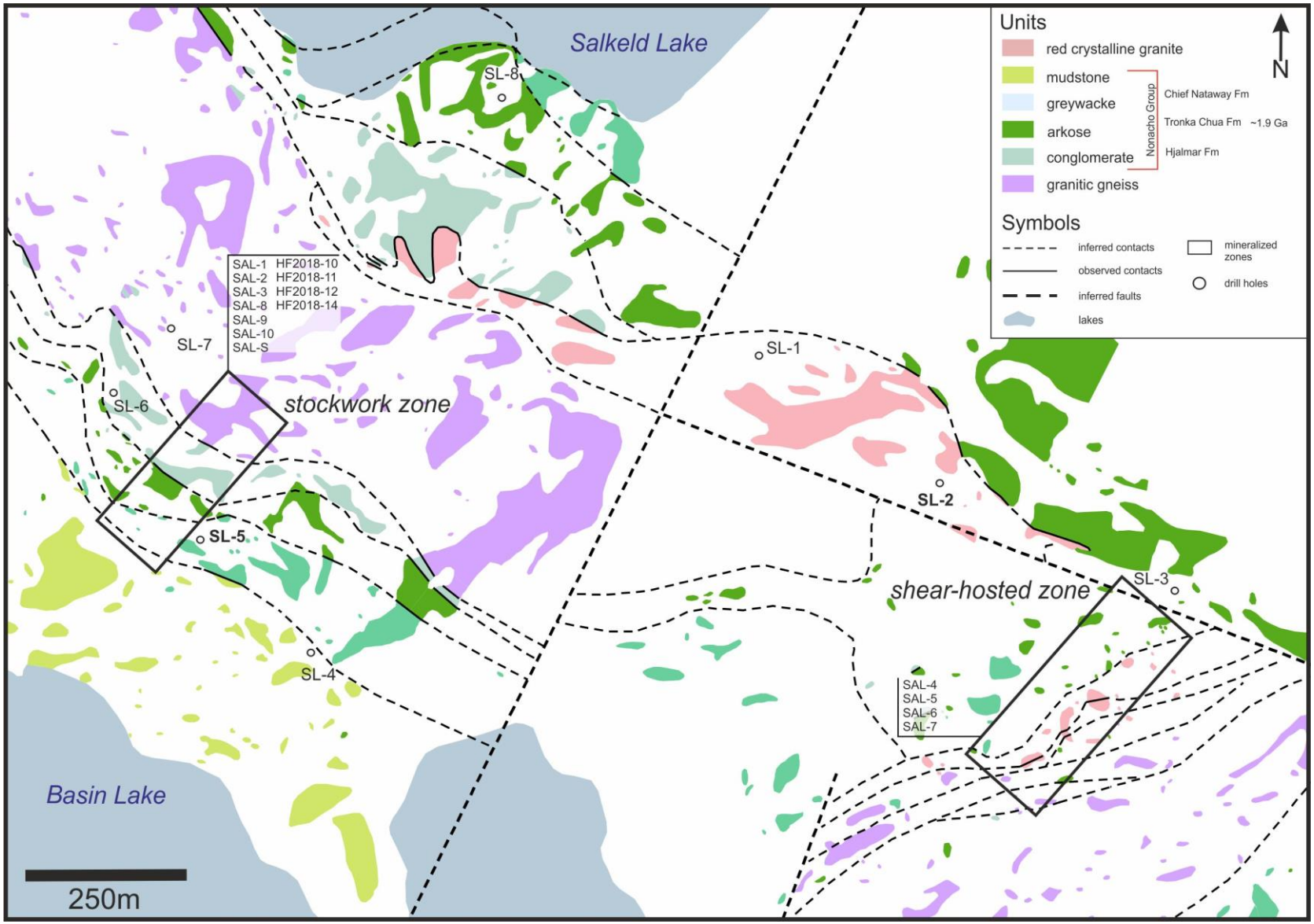
Salkeld Lake
Basin Lake
SL-8
SL-7
SL-6
SL-5
SL-4
SL-1
SL-2
SL-3
SAL-1 HF2018-10
SAL-2 HF2018-11
SAL-3 HF2018-12
SAL-8 HF2018-14
SAL-9
SAL-10
SAL-S
stockwork zone
shear-hosted zone
SAL-4
SAL-5
SAL-6
SAL-7
250m
N
Units
red crystalline granite
mudstone
greywacke
arkose
conglomerate
granitic gneiss
Nonacho Group
Chief Nataway Fm
Tronka Chua Fm ~1.9 Ga
Hjalmar Fm
Symbols
inferred contacts
observed contacts
inferred faults
lakes
mineralized zones
drill holes

2.3 Exploration history

The study area first attracted the attention of the exploration companies in the 1950s, initially looking for the U deposits in the Nonacho Basin. These efforts led to the discovery of the Ag and sulfide mineralization at the Salkeld property. During 1952, high-grade Ag, Cu, Pb and Zn were discovered by Frobisher Limited. Prospecting and exploration have been done over the 1950s by several groups, including McPhar Geophysics Incorporated, that conducted a geophysical survey and prospecting of the showing in 1956, however, failed to identify the extent of the mineralization. Assay results of the samples returned 12 wt% Cu and 274 ppm Ag. Drilling in the area was done by International Nickel Company of Canada Limited (Inco) in 1961, reporting low-grade Cu and Ni mineralization, and later in 1967, by Jason Explorers Limited, trenching and prospecting the property. Grade reported from a composite sample from trenching yielded 12 wt% Cu, 1.5 wt% Pb, 4.7 wt% Zn, 685 ppm Ag, and 2.7 ppm Au. During the 1970s U exploration, the area was covered by at least two airborne geophysical surveys, although the period between 1967 to 1988 has little evidence of any work carried out around Salkeld Lake. The property was optioned to Fortune Minerals in 1988 and a preliminary property review and examination was conducted. Two known areas of mineralization were evaluated, and two distinct styles of mineralization were noted. Teck Corporation entered a joint venture with Fortune Minerals and in 1993 mapped and prospected the Salkeld Lake area. Using values reported by Fortune Minerals from drill holes and trenches, property resource was calculated. A resource of 58,426 tonnes at an average grade of 0.63 wt% Cu was reported for the stockwork-hosted mineralization. Using slightly different criteria for the shear- hosted mineralization, a resource of 53,524 tonnes of 59.65

ppm Ag, and 1.42 wt% Cu were reported. No allowance for dilution or mining methods was factored into the resource calculation. No other work has been reported since, as diamond drill core assay results provided lower than anticipated concentrations of major minerals of interest (Cu, Ag, Zn, Pb). During the winter of 2006-2007 the Northwest Territories Geological Survey had an aeromagnetic survey flown over the Nonacho Basin region using a 400-metre nominal linespacing.

Since 1994, no further prospecting and exploration has been done at Salkeld Lake, and the relationship of Cu to the U showings in the Nonacho Basin, the age and type of Cu mineralization remained unknown, although several deposit types were proposed to characterize the occurrence, most notably, Olympic Dam-type (Webb, 1989) and stratiform-hosted copper (Christopher, 1993), based solely on field observations and available assay data.

Chapter 3: Methods

3.1 Sample collection

During the field seasons of 2018 and 2019, trenches and outcrops at the Salkeld Lake deposit within stockwork and shear-hosted mineralized zones were sampled (11 samples), additionally, four samples were provided by Mr. Hendrik Falck from a previous field season for detailed study (Table 2). Samples were selected encompassing different styles of mineralization and host rocks, including barren and mineralized quartz veins and all varieties of breccias. An additional 16 samples were collected from DDH core pallets left from the 1993-1994 exploration program in order to study intersections with the mineralization at ~100-150 m depth; 3 of these were studied in detail, summarized in Table 2. The sampling strategy for the core was to collect the representative material from split mineralized sections, as well as most to least altered host rocks. Samples were cut, trimmed and separated into groups for further geochemical, petrographic and microanalysis at Saint Mary's University, Halifax and collaborating laboratories.

3.2 Mineralogy and textural study

3.2.1 Optical petrography

Mineralogical and textural investigations were carried out using Olympus BX51 and Nikon Eclipse 50i polarizing microscopes at Saint Mary's University. The dominant ore minerals were identified utilizing reflected light; gangue and accessory minerals as well as fluid inclusions in quartz and carbonate were characterized using transmitted light. Photographs were taken using microscope-mounted high resolution digital cameras.

3.2.2 Scanning electron microscopy (SEM) - energy dispersive spectroscopy (EDS)

A TESCAN MIRA 3 LMU VPS field emission SEM at Saint Mary's University equipped with a backscattered electron (BSE) detector was used to gain a textural understanding of the samples. Energy dispersive spectroscopy (EDS) was used to aid in mineral identification, specifically for optically ambiguous sulfide and accessory phases, as well as to provide preliminary compositional analyses of the minerals. An Oxford Instruments X-max 80mm^2 silicon drift detector was used for EDS analysis. Analytical conditions were a 20 kV accelerating voltage, a 40 µA beam current, and a 17 mm working distance. The software package INCA (ETAS Embedded Systems Canada Inc.) was used for EDS analysis control and data reduction for mineral chemical analyses.

3.2.3 Electron probe micro-analysis (EPMA)

Electron microprobe analyses of sulfides (Cu-Fe sulfides and sphalerite, galena) were performed using a JEOL JXA-8200 'Superprobe', equipped with a W filament source and five wavelength-dispersive (WD)-spectrometers (three equipped with flow-proportional counters, two equipped with sealed Xe-counters), at Dalhousie University, Halifax, Nova Scotia. LDE1, LDE2 and LDE5H diffractor crystals were used for light element analysis (B, C, N, O, F). TAP, TAPH, LiF, LiFH, PETJ and PETH diffractor crystals were used for main group and heavy elements. The instrument was operating at 20 kV accelerating voltage with a 20 nA beam current, and a beam diameter (spot size) of 1 µm. Elements and corresponding X-ray lines measured were as follows: Fe Kα, S Kα, Zn Kα, Cu Kα, Pb Mα, Cd Lα, Ag Lα. Counting times for all elements were 20 seconds on X-ray peaks and 10 seconds on both lower and upper backgrounds. All X-ray count intensity data were acquired using the Probe for EPMA Software$^{(TM)}$ package by John

Donovan (2020) and reduced using the standard ZAF matrix correction method in the software package (after Pichou & Poirier, 1984). The calibration and peak positioning standards used for each element analyzed were as follows: Fe, S – pyrrhotite; Zn – sphalerite; Cu – chalcopyrite; Pb – galena; Cd – pure Cd metal; Ag – pure Ag metal. The reference materials used for calibration, were also analyzed between each group of sample analyses. Three to four analyses per grain were done, totalling 41 spots for chalcopyrite, 50 spots in idaite, 72 in bornite, 23 in chalcocite, 16 in galena, 28 in sphalerite, including 6 spots in very Ag-rich sulfides.

3.2.4 Laser ablation inductively-coupled plasma mass spectrometry (LA-ICP-MS)

Trace element analysis (n=22) of sphalerite by LA-ICP-MS was done at the Department of Earth Sciences, University of New Brunswick. The measurements were acquired using a pulsed (20 ns) 193 nm ArF Excimer laser ablation system (Resonetics RESOlution M-50) coupled to an Ar^- plasma quadrupole ICP-MS (Thermo Scientific X Series II). The ablation system at UNB employs a two-volume Laurin Technic sample cell. Measurements were conducted with a 10 ms dwell time for each analyte isotope, except ^{55}Mn, ^{57}Fe, ^{69}Ga, ^{73}Ge, ^{115}In and ^{113}In that were measured with a 30 ms dwell time. A forward torch power of 1450 W was used, with gas flow rates of 0.8 l/min, 0.65 l/min and 6 ml/min for Ar, He and N_2, respectively, an ablation pit diameter of 90 microns and a laser fluence of 6 J/cm^2. A very large pit size was used to minimize LOD. Routine detection limits varied by isotope (Table 8). The raw data (in cps vs. time) were quantified using the Iolite software package (Paton et al. 2011), with synthetic MASS1 (USGS; Fe-Cu-Zn-S pressed sulfide) and Ge7 (University of Toronto; Liu et al., 2017) used as external reference materials to calibrate analyte sensitivities, SRM610 (NIST; glass) to

monitor instrument drift, and natural sphalerite (Pine Point, Canada) and synthetic sulfide (UQAC FeS1; Savard et al., 2018) as quality control standards. Standard reference materials for calibration and QC were measured at the start, end, and midpoint of the unknown blocks of analyses. Comparison of expected values for trace elements in FeS-1 and Ge7 to concentrations obtained, quantified using MASS-1 as external calibrant yielded uncertainties of < 20% (relative) for all elements except Mn (< 31%), As (< 25%), Se (< 22%), Cu (< 23%), and Au (< 22%). For the majority of analyses, uncertainties were < 10%. Based on EPMA analyses showing that sphalerite from the Salkeld Lake deposit is near-end member ZnS (Table 4), an internal standard value from EPMA of 65.8 wt% Zn was used for quantification.

3.3 Fluid inclusion petrography and microthermometry

Double-polished thick sections were examined by optical microscopy (Olympus BX51) to identify and characterize fluid inclusions in quartz and carbonate using the fluid inclusion assemblage approach ("FIA"; Goldstein & Reynolds, 1994). Fluid inclusion characteristics (shape, size, phase ratios) were recorded at room T. Selected samples (n=8), chosen based on abundance and diversity of types of fluid inclusions, were cut into small chips for microthermometric analysis and removed from the glass substrate in a room T acetone bath (24 hours).

Fluid inclusion assemblages in quartz and calcite were identified and photographed. Recorded measurements included final melting temperatures of the carbonic phase (T_m^{carb}), ice (T_m^{ice}) and clathrate (T_m^{clath}). The homogenization temperature of the carbonic phase (Th_{carb}) and total homogenization temperature (Th_{total}) were also measured. Values

of Th_{total} represent temperatures at which all phases in the inclusion homogenize to a single phase and represent minimum trapping temperature conditions.

Microthermometric measurements conducted on with a Linkam FTIR600 heating-freezing stage mounted on an Olympus BX51 microscope at Saint Mary's University. Uncertainties for the microthermometric measurements are ±0.2°C for measurements around 0°C, and ± 0.5 °C for measurements over 300 °C at a heating rate of 1°C/min. The heating-freezing stage was calibrated using synthetic fluid inclusion standards of pure H_2O (melting at 0 °C and homogenization at the critical point of 374.1 °C), and pure CO_2 (melting at -56.6 °C).

The volume estimation for the gas and fluid phases was done using ImageJ (Rasband, 2012). For three-phase, carbonic-aqueous inclusions volume estimation was based on photos taken at the temperature of carbonic phase homogenization. The salinities were calculated using BULK (Bakker, 2003), using clathrate melting temperature to get salinity of the aqueous phase, and homogenization temperatures of carbonic phase. Isochores we calculated by two independent programs: ISOC (Bakker, 2003); ProBrine (Steele-MacInnis, 2018). For two-phase, aqueous inclusions, SoWat (Driesner & Heinrich 2007) was used to plot the isochores. The carbonic-aqueous and aqueous inclusions were modelled in the $NaCl\text{-}CO_2\text{-}H_2O$ and $NaCl\text{-}H_2O$ systems, respectively.

3.4 Cathodoluminescence

Quartz from 12 samples, as the primary host for fluid inclusions, was studied using hot cathode cathodoluminescence (CL) imaging at Saint Mary's University. The equipment included Lumic HC4-LM hot cathode cathodoluminescence (CL) microscope with a Varian turbomolecular vacuum pump, Olympus BXFM focusing unit, and a Kappa

DX40C Peltier-cooled camera equipped with a Kappa camera control at Saint Mary's University. Differences in luminescence (intensity and colour) were used to identify and differentiate between the several generations of quartz. The CL was operated at an acceleration voltage of 10.0 kV, a beam current between 0.12 and 0.15 mA, a filament current of 2.3 A, a deflection of 10 V and a focus of 5.5 V. Exposure times of 2–7 s were used to optimize colour intensity.

3.5 Raman microspectroscopy

A Jobin-Yvon Horiba LabRam HR confocal Raman microscope with an 800 mm spectrograph and Synapse 1024 x 256 pixel CCD detector, (Saint Mary's University), was used to analyze quartz-hosted fluid inclusions. A 600 grooves/mm grating with a spectral resolution of 0.5 cm^{-1}, and an 80 µm confocal hole size were used during spectrum collection. A 532 -nm (green) Nd-YAG laser (~2 mW at sample surface) was used for excitation, directed through a 100x objective. Frequency calibration was performed using a Horiba Scientific SP-RCO-XP calibration objective (patent reference: FR2934367) employing a NIST-traceable compound in a sealed objective body. Spectra were collected over the range 100–2500 cm^{-1} with three accumulations of 30s-long acquisitions per measured spectrum. Analyses were performed on non-aqueous phases (e.g., vapour bubbles, carbonic phases) to determine the volatile composition of those phases. A Horiba reference standard calibration objective (Standard Pro) was used as a frequency calibration standard.

3.6 Secondary ion mass spectrometry (SIMS)

Stable O isotope ratios ($^{18}O/^{16}O$) of vein quartz and calcite, and S isotope ratios ($^{34}S/^{32}S$) of chalcopyrite were collected in-situ using a CAMECA IMS 7f SIMS at the

Department of Earth Sciences, University of Manitoba. The instrument conditions used for O and S isotope analysis by SIMS were similar. Individual analysis locations were selected with the guidance of textural information from SEM-BSE and CL images. The instrument operated at a 300 V sample offset, -9 kV secondary accelerating voltage, and at mass resolving power of 350. A detailed description of operating conditions for O isotope analysis is provided by Fayek et al. (2002). For O isotope analyses (n=114, from 5 samples), a ~4 nA primary ion beam of cesium (Cs^+) was used, accelerated at 10 kV with a sputtering diameter of ~15 μm to generate and detect secondary ions of $^{18}O^-$ and $^{16}O^-$. Grains of University of Wisconsin Rose quartz (UWQ-1) with a $\delta^{18}O_{V\text{-}SMOW}$ value of 12.33 ± 0.14 ‰ (Kelly et al., 2007) were used as the quartz standard for oxygen isotope analysis. Spot-to-spot reproducibilities for replicate analyses of UWQ-1 were 0.5–0.8 ‰. Grains of Joplin calcite were used as calcite standard for the analyses: the measurements yielded $\delta^{18}Ov\text{-}_{PDB}$ = - 24.38 ± 0.12‰ (Mahon et al., 1998) and overall spot-to-spot reproducibility for replicate analysis was ~0.8‰. SIMS results from the reference materials were compared to accepted isotopic compositions in order to calculate correction factors that were applied to the unknowns measured during the same analytical session (e.g., Holliger & Cathelineau 1988) and results are reported as $\delta^{18}O_{V\text{-}SMOW}$ (‰).

For S isotope analyses (n=22, from 1 sample), a cesium (Cs^+) primary beam with a ~2 nA current was accelerated (+10 kV) onto the sample surface with a sputtering diameter of ~20 μm to generate and detect secondary ions of $^{34}S^-$ and $^{32}S^-$. A chalcopyrite sample (Trout Lake, Manitoba) with an accepted $\delta^{34}S_{V\text{-}CDT}$ value of 0.3 ± 0.2 ‰, determined by SF_6 extraction, was used as the S isotope standard (Crowe & Vaughan, 1996). Results from the reference materials were compared to accepted isotopic

compositions in order to calculate correction factors that were applied to the unknowns measured during the same analytical session (i.e., to correct for IMF; Holliger & Cathelineau, 1988) and results are reported as $\delta^{34}S_{V\text{-}CDT}$ (‰). Spot-to-spot reproducibility for the reference material was 0.3 ‰. For a detailed description of operating conditions and strategy for correction of instrumental mass fractionation and matrix effects for S isotope analysis see Riciputi et al. (1998).

3.7 Laser Ar-Ar age dating

All $^{40}Ar/^{39}Ar$ analytical work was performed at the University of Manitoba using a multi-collector Thermo Fisher Scientific ARGUSVI mass spectrometer, linked to a stainless steel Thermo Fisher Scientific extraction/purification line, Photon Machines (55 W) Fusions 10.6 CO_2 laser and Photon Machines (Analyte Excite) 193 nm laser. Argon isotopes were measured using the following configuration: ^{40}Ar (H1; 1 x 10^{12} Ω resistor), ^{39}Ar (AX; 1 x 10^{13} Ω resistor), ^{38}Ar (L1; 1 x 10^{13} Ω resistor), ^{37}Ar (L2; 1 x 10^{13} Ω resistor) and ^{36}Ar (compact discrete dynode [CDD]). The sensitivity for Ar measurements is ~6.3 x 10^{17} moles/fA as determined from measured aliquots of Fish Canyon Sanidine (Dazé et al., 2003; Kuiper et al., 2008).

Chips from unknowns (6 samples) slices with an area of ~9 mm^2 and ~150 μm thick were cut from polished thick sections that had previously been investigated by optical microscopy and cathodoluminescence. Standards and unknowns were placed in 2 mm-deep wells in 18 mm diameter aluminium disks, with standards placed strategically so that the lateral neutron flux gradients across the disk could be evaluated. Planar regressions were fit to the standard data, and the $^{40}Ar/^{39}Ar$ neutron fluence parameter, J, interpolated for the unknowns. All specimens were irradiated in the Cd-lined, in-core

CLICIT facility of the Oregon State University TRIGA reactor. The duration of irradiation was 35 hours and using the Fish Canyon sanidine (28.201 Ma; Kuiper et al., 2008).

Reference materials were placed in a Cu sample tray, with a KBr cover slip, in a stainless-steel chamber with a differentially pumped ZnS viewport attached to a Thermo Fisher Scientific extraction/purification line and baked with an infrared lamp for 24 hours. Single crystals were fused using the CO_2 laser.

Chips from unknowns were mounted using a ceramic adhesive (PELCO®) on a quartz slide placed in a stainless-steel chamber with a sapphire viewport attached to the same stainless-steel high vacuum extraction system as the CO_2 laser, and baked with an infrared lamp for 48 hours. For this study, the 193 nm laser was operated at an energy of 7 mJ, ablating for 70 seconds over an area of 100 μm x 50 μm. Ablation pits were estimated to be ~ 40 μm deep.

Reactive gases were removed for both the standard and unknown, after 2 minutes, by two NP-10 SAES getters (one at room temperature and one at 450 °C) prior to being admitted to an ARGUS VI mass spectrometer by expansion. Five Ar isotopes were measured simultaneously over a period of 6 minutes. Measured isotope abundances were corrected for extraction-line blanks, which were determined before every sample analysis.

Detector intercalibration (IC) between the different faraday cups was monitored (using the Thermo Qtegra software) every two days by peak hopping ^{40}Ar. The intercalibration factor between H1 and the CDD was measured with the unknowns by online analysis of air pipettes (IC values can be found in Table XX). A value of 295.5 was used for the atmospheric $^{40}Ar/^{36}Ar$ ratio (Steiger and Jaëger, 1977) for the purposes of

routine measurement of mass spectrometer discrimination using air aliquots, and correction for atmospheric argon in the $^{40}Ar/^{39}Ar$ age calculation. Corrections are made for neutron-induced ^{40}Ar from potassium, ^{39}Ar and ^{36}Ar from calcium, and ^{36}Ar from chlorine (Roddick, 1983; Renne et al., 1998; Renne and Norman, 2001). Data collection and reduction was performed using Pychron (Ross, 2019). The decay constants used were those recommended by Min et al. (2000).

3.8 Re-Os age dating

Molybdenite from sample SAL-14B was dated at the Canadian Centre for Isotopic Analysis at the University of Alberta. The sample was sent for heavy mineral separation at Overburden Drilling Management Ltd., Ottawa. From the heavy mineral concentrate (HMC) a molybdenite mineral separate was made using magnetic and gravity methods. The ^{187}Re and ^{187}Os concentrations in molybdenite were determined by isotope dilution mass spectrometry using Carius-tube, solvent extraction, anion chromatography and negative thermal ionization mass spectrometry techniques. For this work, a mixed double spike containing known amounts of isotopically enriched ^{185}Re, ^{190}Os, and ^{188}Os analysis was used (Markey et al., 2007). Isotopic analysis used a ThermoScientific Triton mass spectrometer by Faraday collector. Total procedural blanks for Re and Os are less than <3 picograms and 1 picograms, respectively, which are insignificant in comparison to the Re and Os concentrations in molybdenite. The reference material 8599 Henderson molybdenite (Markey et al., 2007) is routinely analyzed as a standard, and during the past 5 years returned an average Re-Os date of 27.79 ± 0.07 Ma (n=25), indistinguishable from the reference age value of 27.66 ± 0.1 Ma (Wise and Watters, 2011). The ^{187}Re decay constant used is $1.666e\text{-}11a^{-1}$ (Smoliar et al, 1996).

Chapter 4: Results

4.1 Field observations and macroscopic textures

Two mineralized zones at the Salkeld Lake occurrence, referred to as *stockwork* and *shear-hosted zones* in the exploration reports and in this study, were observed at trenched-out areas outlined in the map of the study area (Figures 2.3, 4.1). At the outcrop scale it is evident that the mineralization, occurring mainly as *disseminated* sulfides, post-dates the three dominant host rock units (granitic gneiss, meta-arkose and red alkali granitoid). Granitic gneiss shows evidence of ductile deformation (Figure 4.2F), with sheared quartz clasts indicating a left-lateral sense of shear. However, trails of disseminated chalcopyrite are not sheared, suggesting they overprint the deformation. Meta-arkose (Figure 4.2A) is the dominant host rock, and the majority of the disseminated chalcopyrite is hosted within this meta-sedimentary rock along fractures, within quartz veins and quartz breccias. Alkali red granitoid shows evidence of pervasive potassic alteration, and similar to other lithologies hosts late, disseminated trails of chalcopyrite grains (Figure 4.2D).

General observations from the cross-cutting relationships in the field, relevant to both mineralized zones, indicate that granitic gneiss is the oldest unit, pre-dating the basin sedimentary sequences. Archean basement rocks are overlain by the metasediments of the Hjalmar and Chief Nataway formations, the two formations of the Nonacho Basin meta-sedimentary sequence exposed in the Salkeld Lake area. Younger alkali red granitoid occurs in both zones as localized intrusions, ~2-10 meters in diameter. Quartz and epidote veins are pervasive in the exposed rocks, with quartz veins ranging from 1 to 10 cm in width, and less abundant epidote veins ranging from 2 to 5 cm in width.

Observed veins do not share common orientations, making the identification of the cross-cutting relationships and relative timing of vein generations ambiguous at the outcrop scale. Mineralized areas vary in size from trench to trench, but range within the meter scale; mineralized veins generally trend south-southwest (150-210°).

Figure 4.1 (following page): Representative photos of the trenches and exposed mineralization. A. Trench exposure in the shear-zone showing area of heavily mineralized quartz-sulfide breccia fault bound by units of sheared granitic gneiss. **B.** A magnified image of the box in **A** shows the quartz-sulfide breccia next to a foliated wall-rock. The quartz-sulfide breccia does not contain clasts of the host rock, and appears to be incohesive and unfoliated, with up to 1 cm-wide quartz clasts supported in a sulfide matrix. **C.** Surface oxidation of the sulfide mineralization manifesting as malachite and azurite staining on fracture surfaces in arkose. Green and blue staining is pervasive throughout the mineralized zones and trenches. **D.** Stock-work zone trench exposure. Dashed lines highlight the disseminated fracture-hosted mineralization occupying thin fractures in areas of structural weakness in the host rock (arkose).

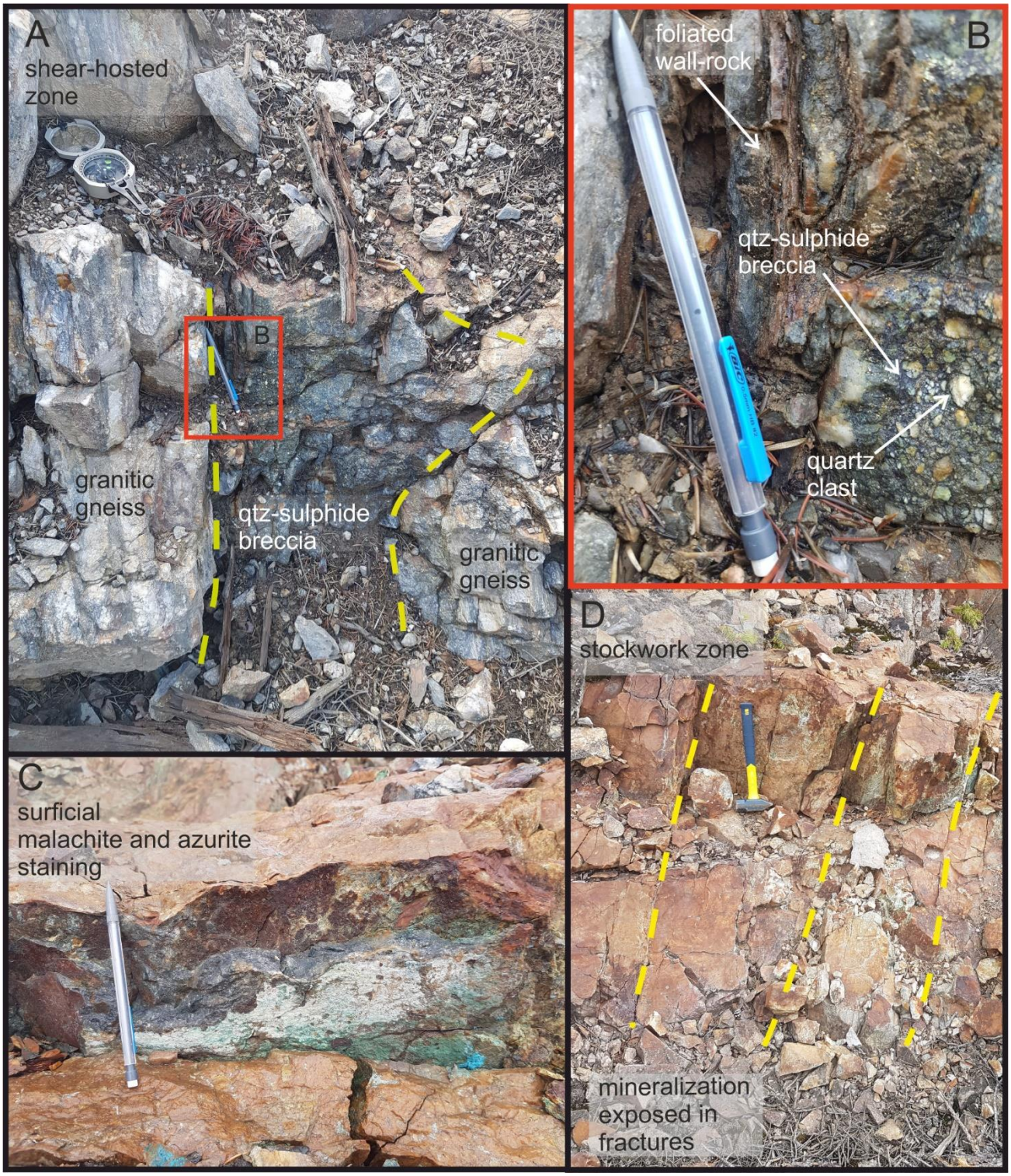
A
shear-hosted zone
B
granitic gneiss
qtz-sulphide breccia
granitic gneiss
B
foliated wall-rock
qtz-sulphide breccia
quartz clast
C
surficial malachite and azurite staining
D
stockwork zone
mineralization exposed in fractures

Figure 4.2: Images of representative hand samples of the three main lithologies and styles of the mineralization. A. *Disseminated* chalcopyrite, the most common style of the mineralization at Salkeld Lake, occupying fractures in arkose. **B.** *Massive* bornite infilling vugs in a massive quartz vein, hosted in altered, brecciated meta-arkose. **C.** Heavily mineralized sulfide-rich (sphalerite, galena, chalcopyrite, bornite) incohesive quartz *breccia*. **D.** The youngest host rock – potassic-altered reddish alkali granitoid – with minor disseminated chalcopyrite. **E.** Metamorphosed arkose, with minor

disseminated chalcopyrite. **F.** The basement host rock – granitic gneiss – with *sheared* quartz clasts and disseminated chalcopyrite. Mineral abbreviations: bn = bornite; cpy = chalcopyrite; qtz = quartz.

Abundant muscovite-epidote alteration, related to the mineralization, is present adjacent to, and enclosing, sulfides. Surface oxidation (identified by azurite and malachite) is persistent throughout the mineralized zones (Figure 4.1C). This does not occur in fresh surface samples.

For the purpose of this study, the designation of the mineralized zones shown in Figure 3 refers to the *dominant* style (breccias in stockwork and disseminated sulfides in shear-hosted zones, respectively) of the mineralization in an outcrop and trenched areas, although all three styles of identified mineralizations and three types of host rocks occur within both *stockwork* and *shear-hosted zones*.

The dominant host rocks of the *stockwork zone* (Figure 4.1D) are granitic gneiss and predominantly metasediments of the Nonacho group, mainly meta-arkoses and to a lesser extent, meta-pelites. Mineralization in the stockwork zone is found within meta-arkoses, gneisses and at the contacts with intrusive granitoid units as disseminated/fracture infilling bornite and chalcopyrite (Figure 4.2A, D, E, F), and filling vugs in quartz veins as massive bornite and chalcopyrite (Figure 4.2B). Heavily mineralized quartz-sulfide breccias are also present in the meta-arkoses. Those do not contain fragments of the host rock, are incohesive and unfoliated, with large (up to 2 cm) quartz clasts in a massive bornite-chalcopyrite-galena-sphalerite matrix (Figure 4.2C). However, the margins of the host rock in contact with the quartz-sulfide breccias are foliated and sheared.

The *shear-hosted zone* (Figure 4.1A) lies within the Chief Nataway Formation and is mostly composed of various metamorphosed Nonacho group meta-sediments, specifically meta-arkoses and meta-pelites, although meta-conglomerates were observed

as well. Relatively small (several meter-scale) outcrops of exposed basement granitic gneiss and younger intrusive red alkali granitoid were seen in this zone. Similar to the *stockwork zone*, three styles of the mineralization (disseminations, fracture fillings, and quartz-sulfide breccias) occur in the host rocks. Figure 4.1A, B illustrates an example of a ~40 cm wide mineralized quartz-sulfide breccia found in granitic gneiss and a close-up view of the breccia at the outcrop scale, bound by the foliated wall-rock. Areas of pervasive silicification near the contact between meta-sedimentary rocks and granitoid are noted and the host rocks are most altered by muscovite-epidote proximal to the heavily mineralized zones.

4.2 Ore and alteration mineralogy

4.2.1 Major sulfides

Samples collected from the Salkeld Lake showing are dominated by the ore assemblage chalcopyrite-bornite-chalcocite-covellite (all samples) ± galena-sphalerite (some samples) mineralization. Figure 4.2 shows hand sample images, revealing macroscopic textures. Disseminated sulfides can be seen fracture filling bleached, silicified, epidotized meta-arkose (Figure 4.2A), granitic gneiss (Figure 4.2F) and potassic-altered alkali red granitoid (Figure 4.2D). Massive sulfides (Figure 4.2B, C) infill vugs in intact and brecciated quartz veins. It is evident in Figure 4.2F, that disseminated chalcopyrite is late and post-dates the sheared host, therefore the *shear-hosted* term can be used only in reference to the host rocks but not the mineralization.

Of the three styles of the mineralization disseminated chalcopyrite and massive bornite-chalcopyrite infilling vugs are the most common. In the samples collected from the trenches, vein-hosted disseminated and massive sulfides show several key

microscopic textures. Notably, sequential rim replacement textures occur in the sequence chalcopyrite (earliest)→bornite→chalcocite-(djurleite-digenite)→covellite (latest) (Figure 4.3A). Although less abundant in the samples, idaite (Cu_5FeS_6), yarrowite (Cu_9S_8) and spionkopite ($Cu_{1.4}S$) show similar rim replacement with covellite. In rare, heavily mineralized quartz-sulfide breccia samples, the textures are limited to mutual grain boundaries between sphalerite, galena, chalcopyrite, idaite and, less commonly, bornite are observed, suggesting these minerals are broadly coeval (Figure 4.3B, D). In majority of the samples, bornite and chalcopyrite exhibit a variety of textures, including boxwork replacement textures, open space filling in quartz and calcite (Figure 4.3A, I), and island-mainland replacement (Figure 4.3A), where bornite is replacing chalcopyrite. These textures indicate the relative timing of mineral precipitation and aid in the delineating of the paragenetic sequence.

A distinction must be made between the samples collected from the trenches (hereafter referred as surface samples) and from the DDH (hereafter also referred as core samples). In the core samples, sulfides exhibit similar textures to those in the surface samples – rim replacement is the most common texture, with chalcopyrite replacing bornite and covellite replacing bornite (Figure 4.3H-J). Another common texture is massive bornite-chalcocite grains occurring with mutual grain boundaries (Figure 4.3H), island-mainland and boxwork replacement. Within the mineralized veins, sulfides are coeval with calcite and infill vugs and cavities in quartz (Figure 4.3J, Figure 4.4A). The major difference between surface and core samples is the relative sequence of the rim replacement textures. Figure 4.3K and Figure 4.3A show this key difference in the mineral sequence that occurs in the core samples (bornite→chalcopyrite), whereas in the surface

samples it is chalcopyrite→bornite. In fewer instances, the sequence in core samples appears as covellite→bornite→chalcocite-digenite→chalcopyrite, though this has been noted only twice in all of the examined samples. Bornite grains in the core samples show two distinct colours, purple and pink (Figure 4.3H, I), suggesting a compositional difference between bornite in contact with chalcocite and bornite in contact with chalcopyrite. Grains of native silver can be found partly enclosed in bornite and chalcopyrite (both Ag-rich) together with calcite (Figure 4.4A) infilling vugs in quartz. Notably, sphalerite and galena occur only in quartz-sulfide breccias and are absent from the majority of the samples, and never occur in the core samples.

Figure 4.3 (following page): Reflected light images showing sulfide mineralization in the surface and diamond drill hole (DDH) samples. A. Successive rim replacement showing the sequence cpy → bn → cov in the surface samples. **B**. Mutual grain boundary textures between sph, ga, id and cpy. **C-E.** Sulfide-muscovite textural relationship between early euhedral muscovite lining fractures and later Cu-Fe sulfides, infilling these fractures and spaces between musc blades. **F-H.** Inclusions of platy mol in Cu-Fe sulfides and host rock with some mol grains oriented parallel to, and included in, the musc, circled in red. **I-K.** Note colour difference between Ag-poor and Ag-rich bn grains in DDH samples where bn is cpy associated vs. cc associated. Textures in the DDH samples show cpy rimming bn filling open space in calcite. Sulfides filling in spaces in quartz and calcite. **L.** Chalcopyrite is rim replacing covellite, which occurs with chalcocite. Mineral abbreviations: ad = adularia; bn = bornite; cal = calcite; cc = chalcocite; cpy = chalcopyrite; cov = covellite; ep = epidote; ga = galena; id = idaite; mol = molybdenite; musc = muscovite; qtz = quartz; sph = sphalerite.

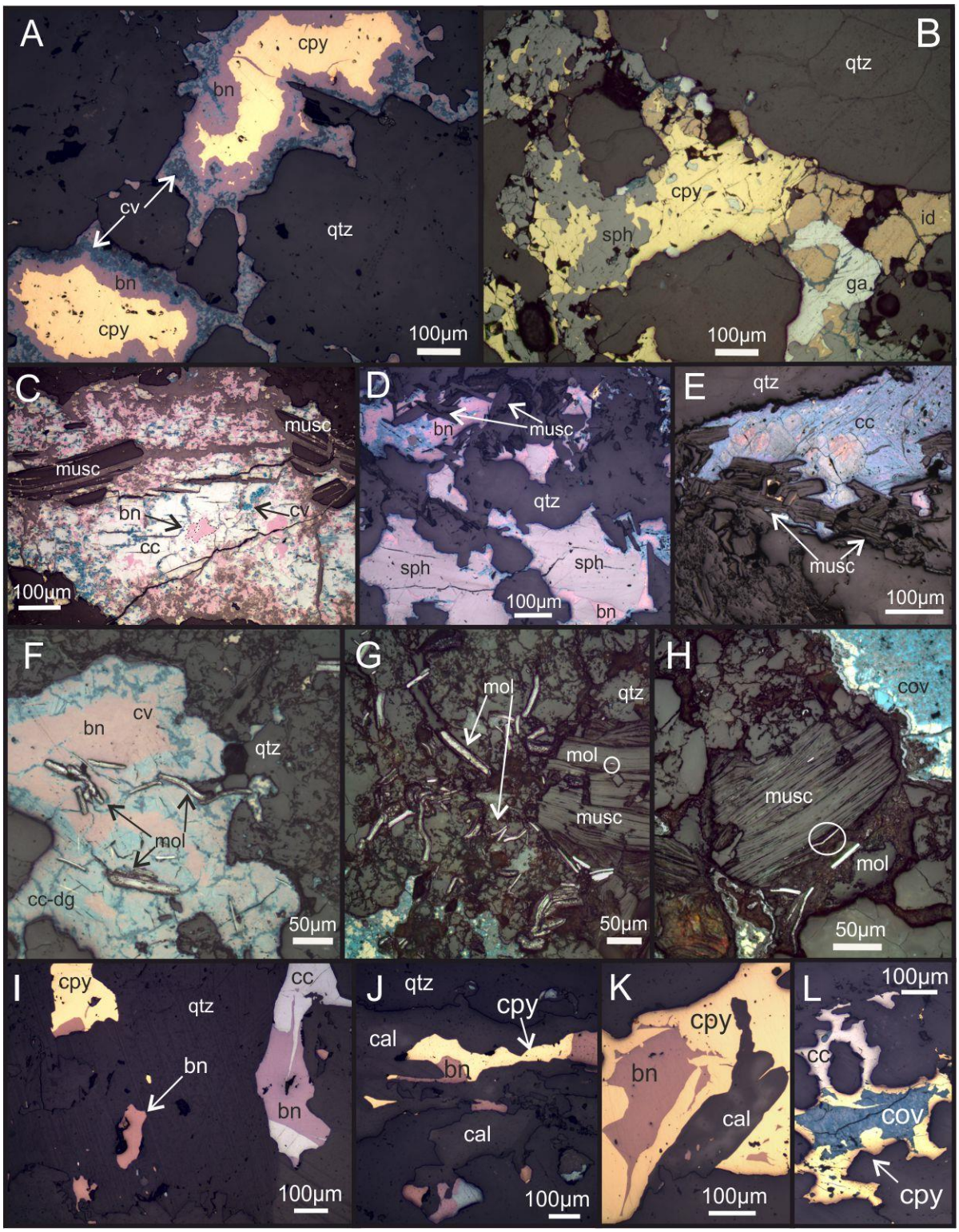
A
cpy
bn
cv
qtz
bn
cpy
100µm
B
qtz
cpy
sph
id
ga
100µm
C
musc
musc
bn
cv
cc
100µm
D
bn
musc
qtz
sph
sph
100µm
bn
E
qtz
cc
musc
100µm
F
bn
cv
qtz
mol
cc-dg
50µm
G
mol
qtz
mol
musc
50µm
H
cov
musc
mol
50µm
I
cpy
qtz
cc
bn
bn
100µm
J
qtz
cpy
cal
bn
cal
100µm
K
cpy
bn
cal
100µm
L
100µm
cc
cov
cpy

Figure 4.4 (following page): SEM-BSE and reflected light images showing accessory phases. A. Silver in the core samples occurring with cpy-bn and calcite. The bn is rimmed by cpy. Calcite infills vuggy cavities in quartz. Silver-chalcopyrite and Ag-rich bornite are spatially associated with a grain of native silver. **B.** Molybdenite grains occurring as inclusions in quartz and k-spar. **C.** Accessory fl in association with mol, musc and k-spar occurring near massive cpy, with bn and cov rimming cpy. **D.** Musc-ep-ad alteration with minor fluorite and calcite. **E.** Massive sulfides post-dating musc, splitting the grains of musc along cleavage plains. Mineral abbreviations: ad = adularia; Ag = native silver; bn = bornite; cal = calcite; cc = chalcocite; cpy = chalcopyrite; cov = covellite; ep = epidote; fl = fluorite; ga = galena; id = idaite; kfs = k-feldspar; mol = molybdenite; musc = muscovite; qtz = quartz; sph = sphalerite; spn = spionkopite.

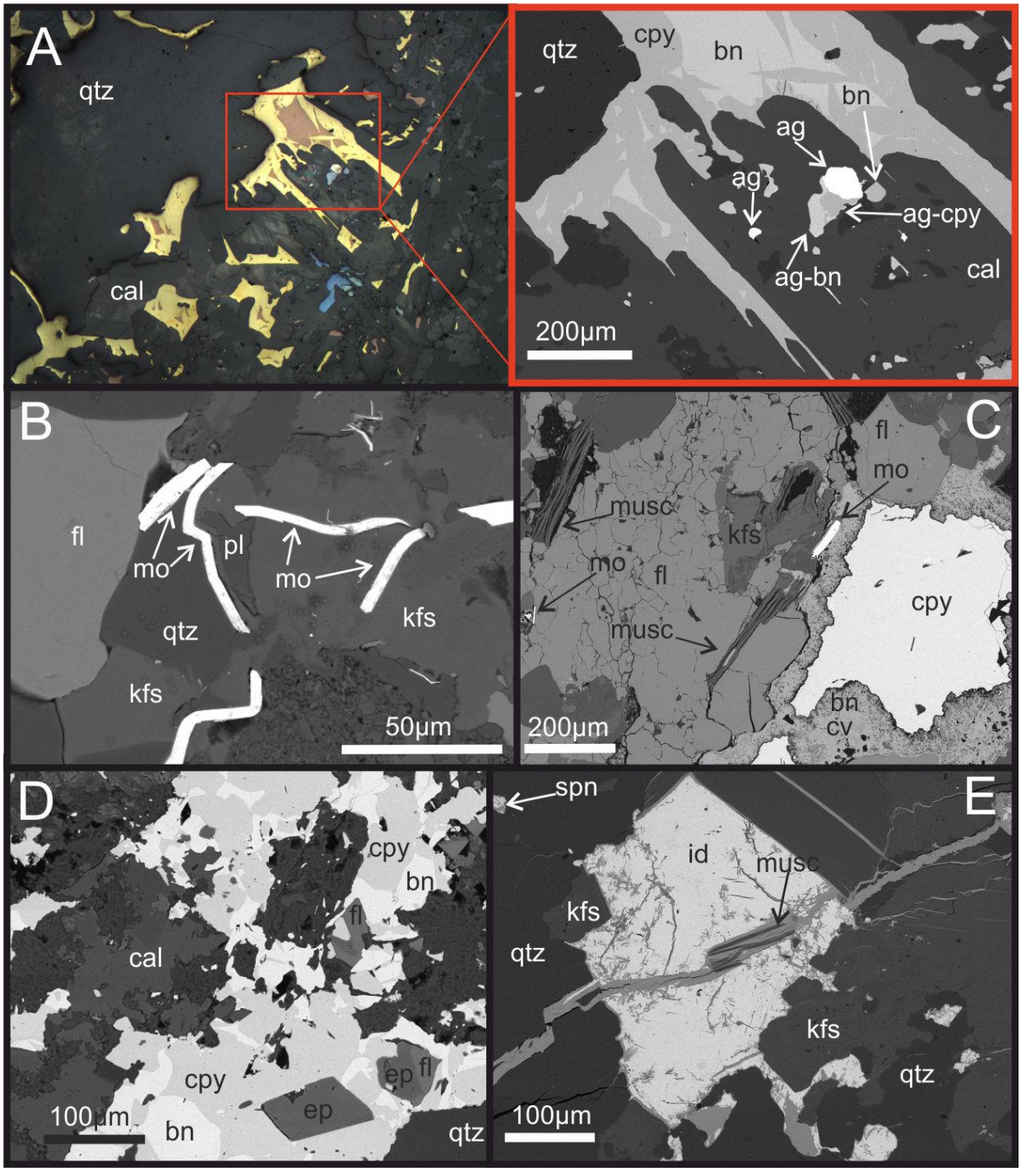
A
qtz
cal
qtz
cpy
bn
bn
ag
ag
ag-cpy
ag-bn
cal
200µm
B
fl
mo
pl
mo
qtz
kfs
kfs
50µm
C
fl
mo
musc
kfs
mo
fl
cpy
musc
bn
cv
200µm
D
cpy
bn
fl
cal
cpy
ep
fl
ep
100µm
bn
qtz
E
spn
id
musc
kfs
qtz
kfs
qtz
100µm

4.2.2 Minor and accessory phases

Grains of molybdenite can occur as inclusions in major sulfides along fractures in quartz (Figure 4.3F), along quartz-muscovite grain boundaries (Figure 4.3G, Figure 4.4B), and included in accessory phases like fluorite (Figure 4.4C). Many molybdenite grains are aligned, and oriented parallel, to the pre-existing fractures (Figure 4.3F). Figures 4.3G-H illustrates an example of a molybdenite grain embedded within the muscovite cleavage, oriented along the cleavage plains, indicating muscovite post-dates molybdenite. This was observed commonly.

Pyrite is a rare sulfide phase in the Salkeld Lake mineralization, present in both surface and core samples. However, it occurs only in the alkali granitoid samples, exhibiting mutual grain boundary texture with chalcopyrite. Another rare accessory sulfide phase is identified as Ag-bearing tetrahedrite $(Cu, Ag)_{10}(Fe, Zn)_2Sb_4S_{13}$ present in the surface brecciated samples only in association with galena. Both pyrite and tetrahedrite are considered trace phases only.

Fluorite is a more abundant accessory phase, occurring together with major sulfides (Figure 4.4C) and in the host rocks. It occurs together with molybdenite and epidote (Figure 4.4B, D), and appears texturally early in the mineralizing sequence. In the host rocks, apatite and titanite were noted, although these phases are not associated with the mineralization assemblages.

4.2.3 Wallrock mineralogy

The mineralogy of wallrock gangue is dominated by quartz, k-feldspar and biotite. Quartz shows undulose extinction and jigsaw textures in mineralized meta-arkose samples (Figure 4.5B, C). K-feldspar is prevalent and can be found in the majority of

samples and is coarse grained in alkali granitoid samples, compared to wall rock biotite. Unlike muscovite, biotite is a host rock phase found distal from the mineralized veins, and the grain size difference between the two micas is apparent; muscovites are much coarser-grained in contact with mineralized quartz vein material.

4.2.4 Alteration assemblages

Figure 4.5A, D, E show muscovite-epidote-adularia (composition of which was confirmed by Raman spectroscopy; Figure 4.6A) alteration associated with the mineralization. The minerals are spatially associated with the dominant sulfide assemblage, appearing proximal to the vein margins (Figure 4.5D). Notably, adularia, only occurs in the core samples, while the assemblage of epidote-muscovite is pervasive across all the samples. Epidote and adularia occur as rhomb-shaped crystals (Figure 4.5E) and, together with muscovite, are included in chalcopyrite (Figure 4.5E-F). Exceptionally large muscovite grains line the vein margins and sulfide-filled cavities in the veins and are generally spatially associated with sulfide-rich areas. Figure 4.3C, D and E illustrate the relationship between early muscovite and later sulfides – in many cases muscovite appears split along the cleavage planes by sulfides overprinting quartz veins (Figures 4.3C, 4.4E). These textural relationships suggest muscovite immediately predates sulfide minerals.

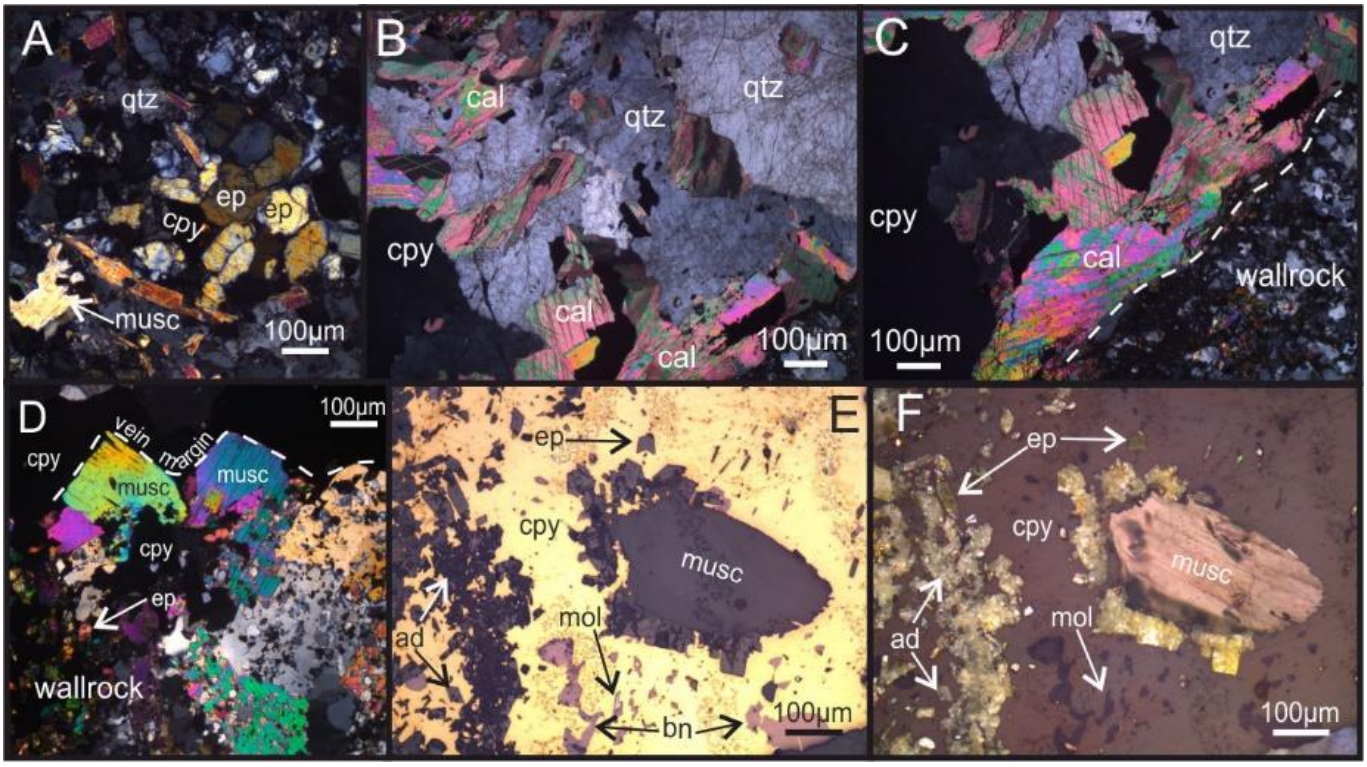

Figure 4.5: Transmitted (A-E) and reflected (F) light images showing alteration styles in the surface and DDH samples. A. Alteration assemblage in mineralized surface samples consisting of musc and ep, infilled by sulfides. **B-D.** Veining in the DDH samples, showing cpy-cal infilling vugs in qtz **(B-C)** and coarse muscovite lining vein margin **(D)**. Note the difference in grain size between qtz in the wallrock and qtz along the vein margins. **E.** Reflected light image showing early alteration minerals embedded in sulfides consisting of musc, ep and ad **F.** The same area as in **E** but in transmitted light. Mineral abbreviations: ad = adularia; bn = bornite; cal = calcite; cc = chalcocite; cpy = chalcopyrite; cov = covellite; ep = epidote; ga = galena; id = idaite; mol = molybdenite; musc = muscovite; qtz = quartz; sph = sphalerite.

Figure 4.6 (following page): Raman spectra for alkali feldspar in mineralized veins and fluid inclusion volatiles from the Salkeld Lake samples. A. Reference Raman spectra for adularia (top spectrum) and sanidine (middle spectrum) from Eastwood et al. (2015) showing the diagnostic band in the region from 138-140 cm^{-1} that is utilized to differentiate adularia from sanidine. The spectrum at the bottom is the K-spar from Salkeld Lake mineralized veins, showing the same adularia-related feature at 138 cm^{-1}. **B.** The top spectra is from a vapour bubble in a type II inclusion showing no detectable CO_2, low intensity CH_4 band and H_2O liquid band from the aqueous phase inside the inclusion. The lower two spectra are from the carbonic fluid bubble in a type I inclusion; the middle spectrum was collected at 40 ^oC while the carbonic phase was a single-phase liquid (homogenized and held at T on a hot stage prior to spectrum collection) whereas the bottom spectrum was taken from the carbonic liquid phase in the same inclusion but in an unhomogenized, three-phase state. Note the pronounced CO_2 peaks (fermi diad) that decrease in intensity and shift slightly to higher wavenumbers from the unhomogenized to homogenized spectrum. Type I inclusions contain only trace N_2 and no CH_4.

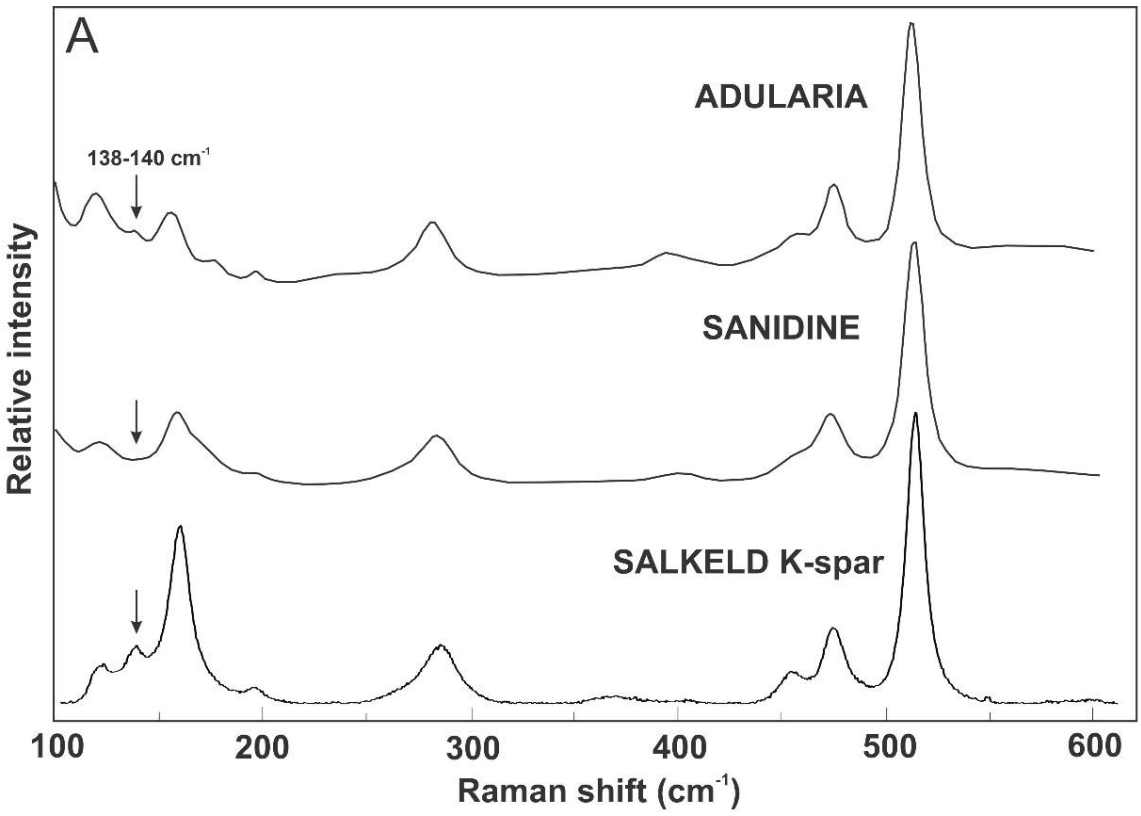
A
ADULARIA
138-140 cm-1
SANIDINE
SALKELD K-spar
Relative intensity
100
200
300
400
500
600
Raman shift (cm-1)

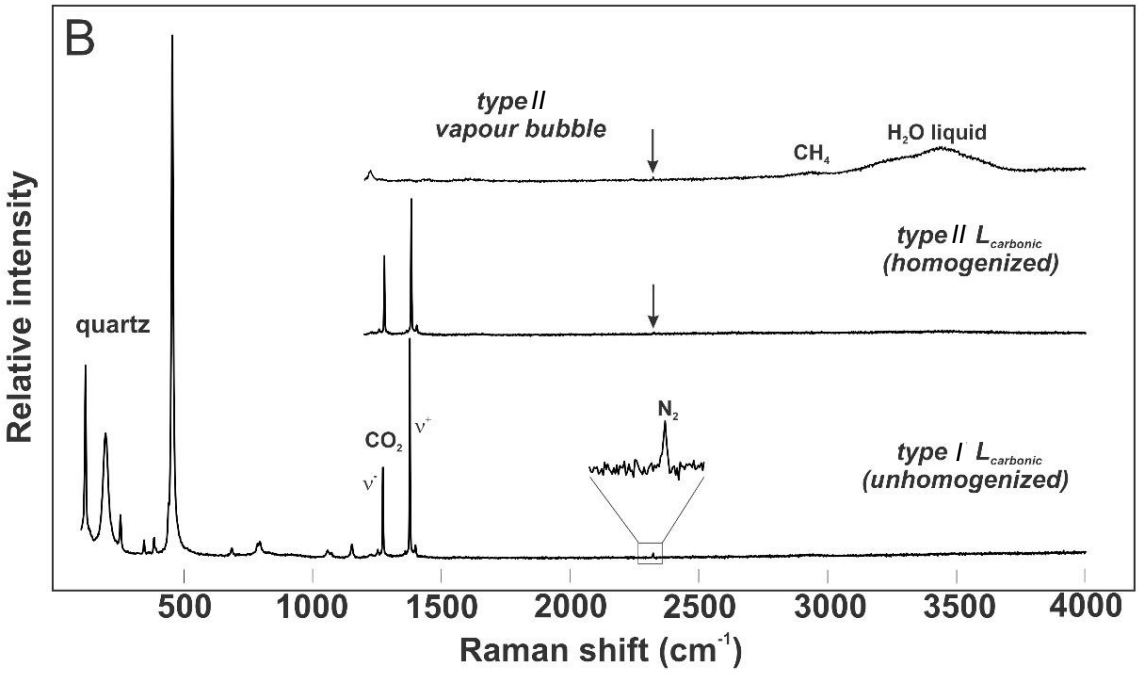
B
type II
vapour bubble
CH4
H2O liquid
type II Lcarbonic
(homogenized)
quartz
CO2
N2
type I Lcarbonic
(unhomogenized)
Relative intensity
500
1000
1500
2000
2500
3000
3500
4000
Raman shift (cm-1)

4.3 Whole rock and mineral chemistry

4.3.1 Bulk rock geochemistry

Whole rock analyses of mineralized samples are listed in Table 6. All the analyzed samples show elevated Cu (up to 12.5 wt%), Ag (~40-600 ppm), Pb (up to 3 wt%) and Zn (up to 20 wt%), but Au is consistently low (average 0.27 ppm). Of note, bulk rock data show that samples are enriched in Cd (up to 300 ppm) in Zn-rich sample, Ba (in some samples >1740 ppm) and Mo (up to 420 ppm) but very U-poor (0.22-0.32 ppm). Breccia and vein mineralization samples show much higher abundances of Pb, Zn, Cd, Mo and Ag, while disseminated mineralization has significantly higher concentrations of Ba, but lower concentrations of major ore metals.

4.3.2 SEM-EDS and EPMA analysis

Representative analysis of major and accessory minerals (i.e., chalcopyrite, bornite, idaite, sphalerite, galena, chalcocite, covellite) acquired from SEM-EDS and EPMA analysis are recorded in Table 3a, b and Table 4. EPMA analyses show the compositional range of major Cu-Fe-S is consistent from sample to sample with little variation, in both surface and core samples. Chemical make-up of chalcopyrite ranges insignificantly from 33.59-35.93 wt% Cu, 28.39-30.56 wt% Fe and 32.46-35.02 wt% S. Bornite analysis shows 60.90-65.01 wt% Cu, 9.19-11.83 wt% Fe and 25.09-26.28 wt% S. Chalcocite-djurleite-digenite solid solution falls within the range of 76.2-79.7 wt% Cu and 21.5-23.4 wt% S. Idaite is only present at the surface and has compositional range of 50.78-58.31 wt% Cu,11.51-15.57 wt% Fe and 30.99-33.59 wt% S. Results of sphalerite analysis reveals little compositional variation, ranging from 32.38 to 33.39 wt% S, 63.37 to 65.68

wt% Zn and additionally, 0.84 to 1.11 wt% Cd. Galena analysis showed little compositional variation, ranging from 14.13 to 14.53 wt% S, 84.36 to 87.4 wt% Pb.

Silver is enriched in chalcopyrite and bornite in the core samples; based on EPMA and SEM-EDS data, concentrations range up to 0.2-2.22 wt% Ag in chalcopyrite and up to 4.6 wt% Ag in bornite (Figure 4.4A). An unknown phase in the sample SLC-1b has Ag content up to 31.6 wt%. Concentrations of Ag in chalcopyrite and bornite in the surface samples are very low (<0.01 wt% Ag), with an exception of one sample (SAL-2a), in which the concentration of silver in bornite ranges from 6.4-8.1 wt% Ag in a single area in a thin section.

A ternary diagram shows the plotted EPMA and SEM-EDS data for Cu-Fe-S phases (Figure 4.7A) and the ideal wt% compositions (Figure 4.7B) for comparison. The plot shows that the phases lie in a compositional trend, showing chalcopyrite→idaite→bornite→chalcocite→djurleite→digenite→spionkopite→yarrowite →covellite, with the latter part of the sequence shifting towards more S-rich minerals, losing the Fe component. Analyzed sulfides correspond closely to the ideal end-member compositions. This is consistent with textural observations that show chalcopyrite, idaite and in rare cases bornite exhibiting mutual grain boundary, (thus coeval) whereas bornite, chalcocite and the rest of the sequence leading up to covellite shows rim and island-mainland replacement textures of earlier chalcopyrite and idaite, which is interpreted to signify decreasing Fe as the mineralization progresses, and then increasing S once the compositions reach the Cu-S join. Notably, the core samples texturally follow a reverse paragenetic path from covellite to chalcopyrite, excluding surface-only minerals like idaite, spionkopite and yarrowite.

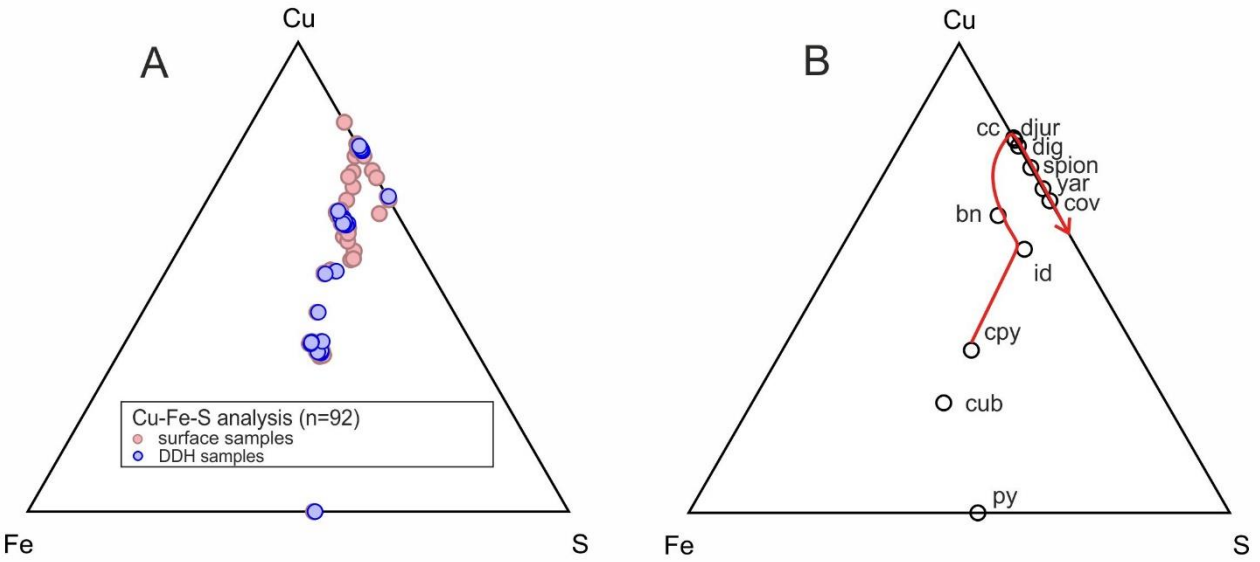

Figure 4.7: Ternary diagrams (Cu-Fe-S; wt%) showing the chemical composition of sulfides. A. Ternary diagram showing SEM-EDS and EMPA analyses of major Cu-Fe sulfides from Salkeld Lake, including both surface and DDH samples. **B.** Ternary diagram showing ideal compositions of major Cu-Fe sulfides and the inferred paragenetic sequence of the sulfides at Salkeld Lake (red arrows), tracing the compositional change from cpy to cov, reflecting increasing Cu : Fe ratios by decreasing Cu : S ratios along the Cu-S join. Mineral abbreviations: bn = bornite; cc = chalcocite; cpy = chalcopyrite; cov = covellite; cub = cubanite; dig = digenite; djur = djurleite; id = idaite; py = pyrite; spion = spionkopite; yar = yarrowite.

Of note, K-feldspar data shows elevated concentrations of Ba, ranging from 0.53-2.88 wt%, shown in Table 3b.

4.3.3 LA-ICP-MS analysis of sphalerite

Trace element composition of sphalerite acquired from the LA-ICP-MS analysis is provided in Table 8. Nickel, Ge, As, Te, Au and Bi values fell below detection limits and are not shown in the table. The data acquired reveals elevated values of Cd in sphalerite, ranging from ~11800 to ~14700 ppm, consistent with the EPMA and SEM-EDS analysis. Concentrations of Cd within small area (crystal-scale) appear to be uniform, although on a thin section scale, there is variability. Concentrations of the trace elements analyzed (in orders of magnitude ppm) are as follows: Mn (10^1), Fe (10^2), Co (10^1), Ga (10^{-1}), Ge (10^{-2}), In (10^{-2}), Se (10^1) and Ag (10^1).

Selected trace element concentrations for Ga, Ge, In, Fe, and Mn were utilized in sphalerite geothermometry calculations using the Frenzel et al. (2016) calibration to obtain additional temperature constraints on sphalerite precipitation. The calibration used is as follows:

$$PC1^* = \ln [(C_{Ga}^{0.22} * C_{Ge}^{0.22}) / (C_{Fe}^{0.37} * C_{Mn}^{0.20} * C_{In}^{0.11})], \quad (1)$$

where C_{Ga}, C_{Ge}, C_{In} and C_{Mn} are concentrations of Ga, Ge, In and Mn, respectively, in ppm, and C_{Fe} is Fe concentration in wt.%. The relationship is sufficiently strong to be used as a preliminary geothermometer Ga-Ge-In-Mn-Fe (GGIMFis). The empirical relationship between PC 1* and temperature, T, is:

$$T\ (^oC) = (54.4 \pm 7.3) * PC1^* + (208 \pm 10). \quad (2)$$

The results of sphalerite thermometry utilizing the LA-ICP-MS data yielded an average temperature of 169.11 ± 15 ^{o}C (range calculated on the basis of the lowest and highest calculated value from 22 sphalerite analyses).

4.4 Cathodoluminescence

Four generations of quartz were identified and differentiated on the basis of colour and intensity of CL luminescence (Figure 4.8). Figure 4.8C shows type I (first generation quartz), which luminesces blue and is the earliest identifiable generation. In some of the vein samples blue quartz grains are large and appear intact. In majority of the samples, however, type I quartz is brecciated and partly replaced and resorbed by type II quartz (second generation), which is black (non-luminescing). The two types are indistinguishable in plane- and cross-polarized light as evidenced in Figure 4.8A, B, C. Both type I and II quartz do not show any evidence of being coeval with the sulfides, which show open-space filling textures in quartz. Sulfides replace type II quartz (Figure 4.8A-C, E-F), and fill what may be vugs or dissolution cavities in type II quartz. Type III quartz, (third generation; Figure 4.8G), luminesces yellow-green, post-dates black type II quartz, and coincides to fractured areas near heavily mineralized domains. In a few samples the density of type III quartz is unambiguously highest surrounding sulfide patches (4.8D, E, G). Type IV quartz post-dates type III quartz and luminesces dim, pale blue, appearing along the boundaries of some sulfides and encasing yellow type III quartz and fragments of type II quartz (Figure 4.8I, K). Similar to type I and II, type III and IV quartz appear indistinguishable from one another unless CL imaging is done. Although all four quartz generations can be found in contact with sulfides, only type III and IV quartz envelop the

sulfides completely, and are deemed sulfide-coeval. Type III quartz distribution coincides with trails of vapour-rich fluid inclusions (Figure 4.8H).

Figure 4.8 (following page): Hot cathode cathodoluminescence (CL) of various quartz generations associated with mineralization at Salkeld Lake. The four generations of quartz were differentiated by the intensity and colour of luminescence. Quartz and sulfide grains are outlined throughout the frames to illustrate selected quartz generations and their spatial association with sulfides. **A.** Transmitted plane-polarized light image highlighting an area for CL analysis in a massive qtz veins. **B.** Transmitted cross-polarized image of the selected study area. **C.** CL image showing the distinct bright blue luminescence of the early **type I** (1st generation) quartz, that is being replaced by non-luminescing **type II** (2nd generation) appearing black. The two generations are indistinguishable in the plane- and cross-polarized light. Sulfides (cpy-bn) replace both type I and type II qtz. **D.** An enlarged image (transmitted light) depicting fluid inclusion poor areas associated with the type I and type II quartz. **E.** Transmitted, plane-polarized light image highlighting the area for CL analysis of the frame **G**. **F.** Transmitted cross-polarized image of the selected study area of the frame **G**. **G.** CL image showing the 3rd generation (**type III**) yellow-green luminescing quartz, enveloping the sulfide and highlighting fluid inclusion trails. The abundance of type III qtz is high in sulfide-rich areas suggesting a genetic link. Type III qtz overprints type II non-luminescing quartz. **H.** An enlarged image of the fluid inclusion-rich area associated with the type III yellow-luminescing quartz. **I.** CL image showing the 4th generation quartz (**type IV**) luminescing dim blue and overprinting by brecciation type III yellow-luminescing quartz. Note the difference in intensity of type IV qtz compared to type I (bright blue) quartz. **J.** Transmitted, plane-polarized light image highlighting the area for CL analysis of frame **I**. **K.** CL image showing the spatial association between the type I, II, III and IV quartz

generations. Type II is the most abundant in the samples and is replaced by fluid inclusion-rich type III, closely associated with sulfides and type IV quartz. **L.** Transmitted plane-polarized light image highlighting the area for CL analysis of frame **K**.

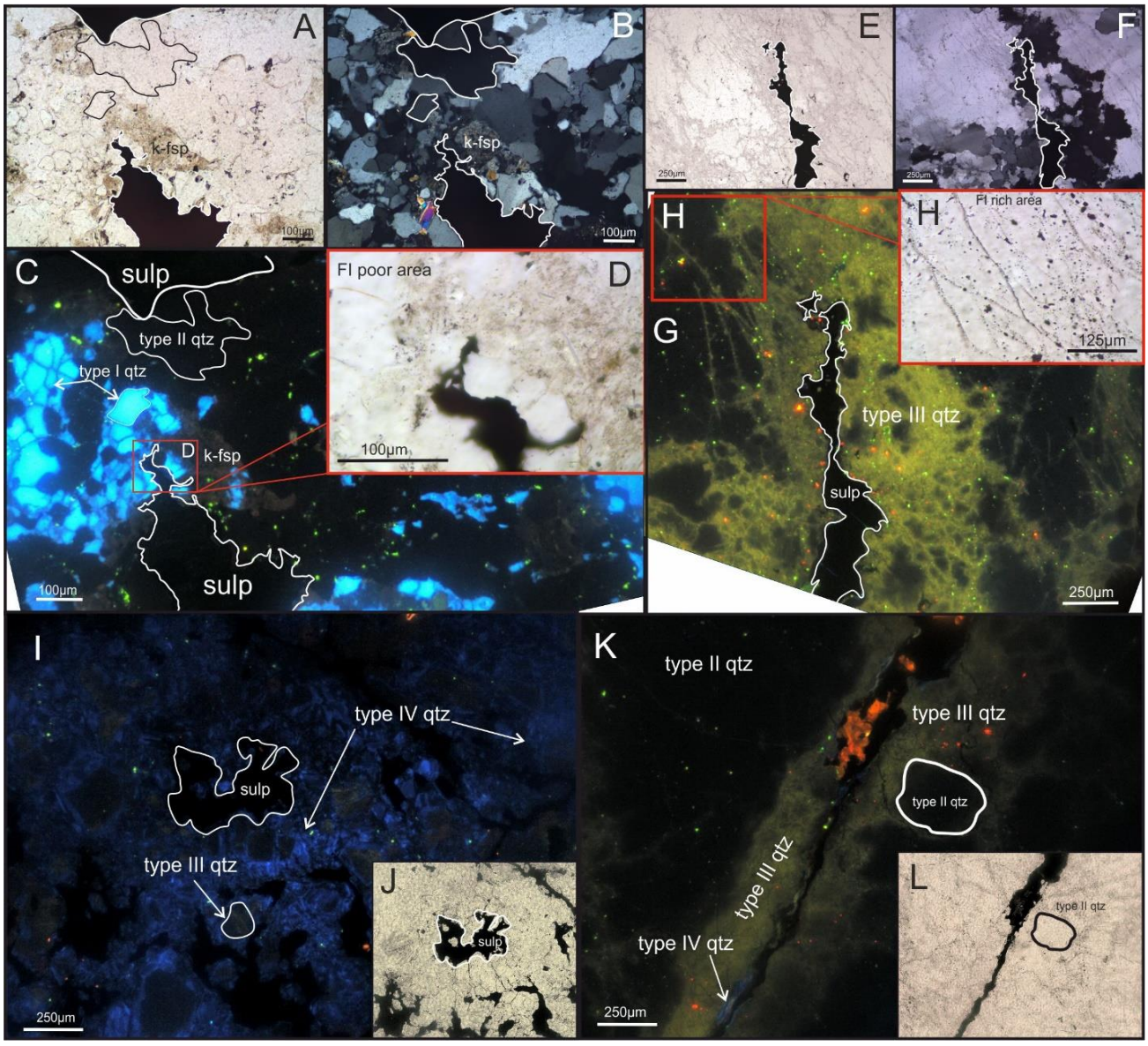
A
k-fsp
100µm
B
k-fsp
100µm
E
250µm
F
250µm
C
sulp
type II qtz
type I qtz
D
k-fsp
100µm
sulp
FI poor area
D
100µm
H
G
type III qtz
sulp
250µm
H
FI rich area
125µm
I
type IV qtz
sulp
type III qtz
250µm
J
sulp
K
type II qtz
type III qtz
type II qtz
type III qtz
type IV qtz
250µm
L
type II qtz

4.5 Fluid inclusion petrography

Fluid inclusions were grouped using the fluid inclusion assemblage ("FIA") method (Goldstein et al., 2003; Chi et al., 2008). An FIA represents a group of inclusions the were trapped *coevally* in secondary trails or planes (healed fractures) or in small clusters of indeterminate origin within quartz and calcite. Inclusions, classified as indeterminate, do not occur in secondary planes. For these, no unambiguous evidence for primary origin was found. They are interpreted as being broadly related to host quartz or calcite formation.

Three types of inclusions were identified in the Salkeld Lake samples, hosted in quartz, calcite and sphalerite, observed at room T (Figure 4.9):

- Type I (Figure 4.9A, F, I, J): early, two or three-phase ($L_{aq}+L_{carb}\pm V_{carb}$) carbonic-aqueous inclusions. The composition of the carbonic phase was confirmed by Raman spectroscopy (Figure 4.6B) to be near-pure CO_2 with minor N_2.
- Type IIa (Figure 4.9B, G, I, J): two-phase aqueous ($L_{aq}+V$) inclusions hosted in quartz and calcite; aqueous composition with trace CH_4 and trace N_2 confirmed by Raman spectroscopy.
- Type IIb (Figure 4.9C, D, E): two-phase aqueous ($L_{aq}+V$) inclusions hosted in calcite and sphalerite;
- Type III (Figure 4.9H): vapour-rich aqueous inclusions (V_{aq}); aqueous composition with trace CH_4 and trace N_2 confirmed by Raman spectroscopy.

Type I carbonic-aqueous inclusions are the least abundant type, hosted in quartz. They occur as FIA of 5-7 inclusions, and range in size from 10 to 30 μm (Figure 4.9F). They occur in trails that do not extend to grain boundaries (therefore, pseudosecondary)

or are of indeterminate origin where not in trails. Within a single FIA the phase ratios in single inclusions between the carbonic and aqueous phases are quite consistent, with the carbonic vapour phase taking up approximately 1-5 vol%, the liquid carbonic phase 30-40 vol% and the liquid aqueous phase 50-60 vol%. The inclusions do not contain any solid phases and in some of the cases, show some post-entrapment modification (varied phase proportions within FIA and evidence of “necking down”). Such inclusions were not measured by microthermometry and were not considered when describing phase proportions above, and in Table 5.

Type II aqueous inclusions are the most abundant type (Figure 4.9B), hosted in both type II quartz and calcite. They occur throughout type II quartz in secondary trails, commonly in FIA of 5-10 inclusions, and are smaller in size than type I inclusions (2-10 μm). Primary and indeterminate type II aqueous inclusions were identified in calcite. The phase ratios are consistent within individual FIA, but from FIA to FIA, they show considerable variability. In single FIA, regardless of host phase, the proportions of the vapour phase vary from 10-25 vol%, and the liquid phase 75-90 vol%. Secondary type II inclusions occur in sphalerite, and vary in size from 15 to 20 μm. The liquid phase in these sphalerite-hosted type II inclusions comprises 90-95% of the inclusion volume in the majority of inclusions (Figure 4.9E). No solid phases are present in type II inclusions.

The relative spatial relationships and timing of type I and II fluid inclusions in quartz is shown in Figure 4.9J-K. Type I inclusions are “overprinted” by trails of type II aqueous inclusions. The size and orientation of an overprinted type I inclusion in Figure 4.9J-K (inclusion at bottom of images) appears to be similar to other pristine type I inclusions. However, the type I inclusion that is overprinted is missing the carbonic phase entirely,

because it has been cracked opened and refilled by type II fluid, providing an unambiguous timing relationship. Trails of type II aqueous inclusions are usually much shorter than type I inclusions, and appear sub-perpendicular to the orientation direction of type I inclusions, further indicating, that type II post-date type I fluids.

Type III vapour-rich inclusions (Figure 4.9H, I) occur in trails, commonly spatially associated with sulphides. Their size varies greatly from <1 to 30 μm and they occur in greatest abundance along healed fractures; thus, they are of secondary origin. Inclusions appear empty (low density) with no aqueous liquid phase visible. Type III inclusions are most abundant near heavily mineralized zones, coincident with type III, yellow-luminescing quartz, occurring in healed fractures surrounding sulfides.

Figure 4.9 (following page): Representative transmitted light images of the types of fluid inclusions. A. The image shows an area containing type I fluid inclusions of indeterminate origin, hosted in qtz. **B.** The image shows an area containing type IIa, low salinity, secondary aqueous fluid inclusions, hosted in quartz. **C.** The image shows an area containing primary, low salinity type IIb inclusions in calcite. **D.** The image shows an area containing secondary high salinity type IIb inclusions in sphalerite**. E.** An enlarged image of a representative aqueous inclusion hosted in sphalerite. **F.** An enlarged image of a carbonic-aqueous inclusion, showing typical size and phase ratios. Carbonic-aqueous assemblages are small in numbers with 3-5 inclusions per assemblage but comparatively to type II and type III appear to be larger in size. **G.** A close-up image of the aqueous inclusion hosted in quartz showing typical size and phase ratios. Aqueous inclusions are the most abundant in the samples and occur in assemblages of 5-10 inclusions. **H.** A close-up image showing type III vapour-rich inclusions, the range in size and distributions varied from sample to sample. **I.** Many trails of type III secondary inclusions can be seen along the healed quartz fractures. **J-K.** Image and schematic showing the spatial distribution and cross-cutting relationships between type I and II fluids. Type IIa aqueous inclusions post-date type I carbonic-aqueous as evidenced by the former type I inclusion at the bottom of the image showing no carbonic phase, having been cracked open and refilled by type IIa fluid related to the cross-cutting type IIa FIA. Type IIb and type III fluids are pre- to syn-mineralization and post-date type IIa and type I fluids. The designation IIa vs. IIb is based on microthermometry (see section 4.6).

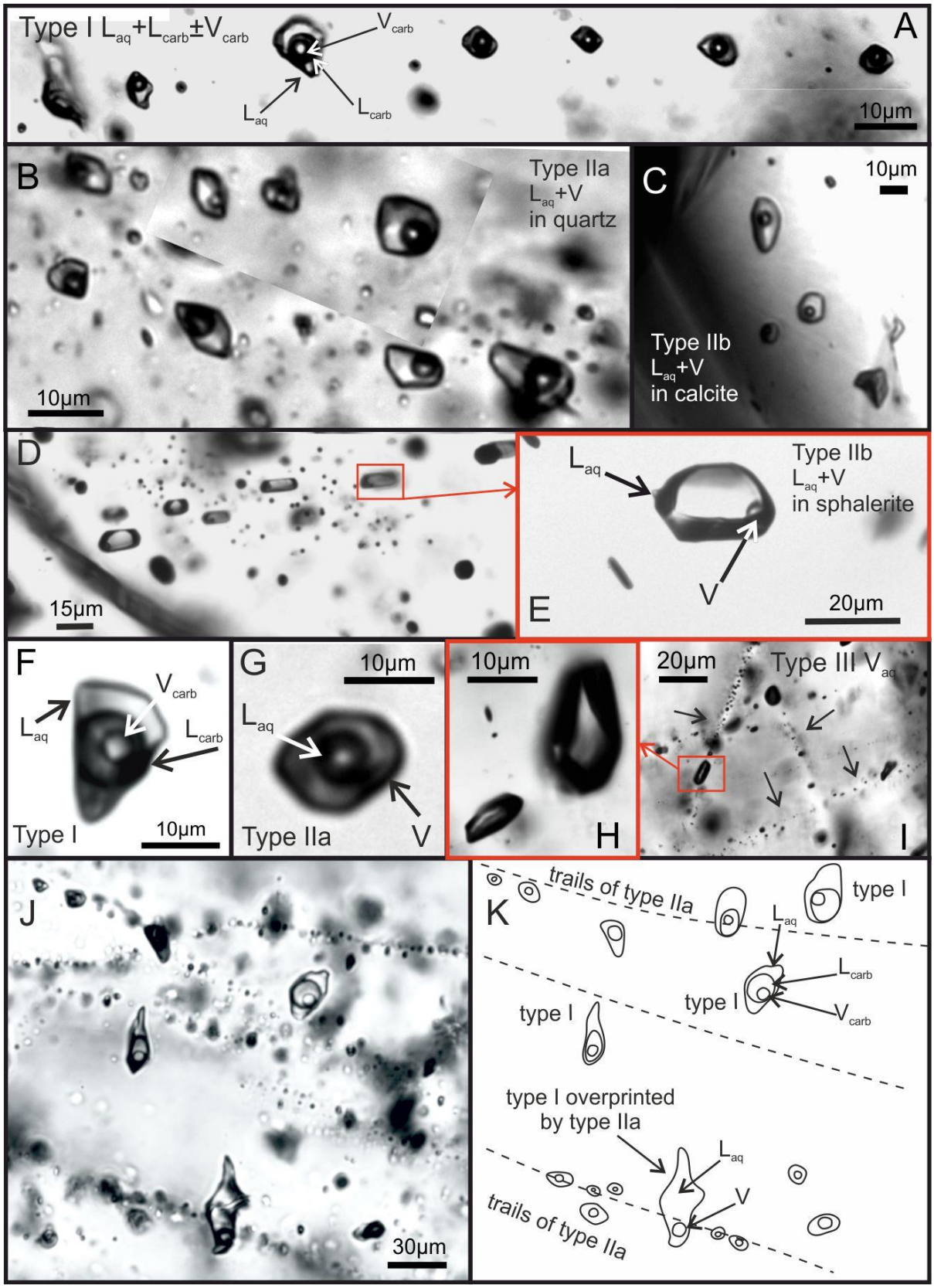
Type I $L_{aq}+L_{carb}\pm V_{carb}$
V_{carb}
L_{aq}
L_{carb}
A
10μm
B
Type IIa
$L_{aq}+V$
in quartz
10μm
C
10μm
Type IIb
$L_{aq}+V$
in calcite
D
15μm
L_{aq}
V
E
Type IIb
$L_{aq}+V$
in sphalerite
20μm
F
V_{carb}
L_{aq}
L_{carb}
Type I
10μm
G
10μm
L_{aq}
Type IIa
V
10μm
H
20μm
Type III V_{aq}
I
J
30μm
K
trails of type IIa
type I
L_{aq}
L_{carb}
type I
type I
V_{carb}
type I overprinted
by type IIa
L_{aq}
V
trails of type IIa

4.6 Microthermometry

Data acquired from microthermometry is summarized in Table 5. All measurements were recorded using a heating rate of 1 ^{o}C/min, and all the measurements were repeated once.

Type I carbonic-aqueous inclusions larger than 10 μm commonly decrepitated on heating due to pressure build-up (Schmidt and Bodnar, 2000) making measurements of total homogenization temperature (Th_{total}) challenging in many chips, and in some, making it impossible to obtain any measurements. Smaller inclusions (<10 μm) yielded some measurements of Th_{total} for type I inclusions, but the majority of inclusions did not yield this parameter.

A total of 107 inclusion measurement sets from 27 FIA were recorded for phase changes in type I fluid inclusions in type II quartz (Figure 4.10; Table 5). Of these, all inclusions yielded measurements of clathrate "melting" (dissociation; T_m^{clath}), carbonic phase melting (T_m^{carb}), and carbonic phase homogenization (Th_{carb}), but only 28 inclusions in 8 FIA yielded Th_{total}. Type I inclusions showed T_m^{carb} from -58.6 to -57.2^{o}C (mean = -56.9 ^{o}C), consistent with the dominant volatile species in the carbonic phase being CO_2. Many FIA show identical values for all contained inclusions, at the resolution of measurement conditions/stage precision. Type I inclusions showed T_m^{clath} from 3.7-7.5 ^{o}C, corresponding to low calculated salinities (3.3-9.0 wt% $NaCl_{eq}$). The values of T_m^{clath} do vary from FIA to FIA, but within single FIA, inclusions usually show identical melting values. Values of Th_{carb} (by bubble point transition) show little variation within FIA, ranging from 25.2 ^{o}C to the critical T across all FIA, with many values close to critical temperature (~31 ^{o}C). Measurements of minimum $T_{trapping}$ (Th_{total}; by total carbonic phase

bubble point transition) were between 285-375 ^{o}C. Total homogenization temperatures showed some variation within FIA (< ±10-15 ^{o}C). Identical values within-FIA for many clathrate and carbonic low-T phase changes, while surprising, are consistent with expected outcomes of measurements that utilize the FIA method (e.g., Fall and Bodnar, 2018).

A total of 117 inclusion measurement sets were recorded for phase changes in type II fluid inclusions (Figure 4.11; Table 5). A distinction was made between secondary type IIa inclusions hosted in type II quartz (n=94; 31 FIA), primary type IIa inclusions hosted in calcite (n=14; 2 FIA), and indeterminate or secondary origin type IIb inclusions hosted in calcite (n=5; 1 FIA) and sphalerite (n=11; 1 FIA). The designation “a” vs. “b” differentiates two subtypes of type II inclusions with contrasting salinity (recognized during microthermometry) and V:L ratios (for inclusions in sphalerite only, compared to type IIa inclusions in quartz).

Type IIa inclusions are hosted in quartz and calcite, and show variable final ice melting T (T_m^{ice}) from -3.5 to -0.1^{o}C, and -1.8 to -0.4 ^{o}C, respectively. These correspond to low salinities (0.2-5.7 wt% $NaCl_{eq.}$, and 0.7-3.1 wt% $NaCl_{eq.}$, respectively). These ranges extend to considerably lower values but with some overlap with bulk salinities for type I inclusions. Single FIA yield nearly identical (within 0.3 ^{o}C) T_m^{ice} values internally. Minimum $T_{trapping}$ (Th_{total}; by bubble point transition) ranges widely (inter-FIA) between 149 to 327 ^{o}C, and 106 and 251 ^{o}C, respectively for quartz and calcite-hosted inclusions. However intra-FIA ranges are relatively small (< ±15-20 ^{o}C). Such ranges are partly attributed to the measurements of inclusions that experienced necking down (undetected

during petrographic scrutiny) or were not part of the FIA (despite petrographic classification as such).

Compared to type IIa inclusions, type IIb inclusions hosted in calcite yielded a significantly high salinity (17.1 wt% $NaCl_{eq.}$ for all inclusions in the FIA) based on a T_m^{ice} of -13.2 ^oC, and significantly lower Th_{total} range (by bubble point transition) from 106.9 to 119.5 ^oC. Type IIb inclusions hosted in sphalerite showed the highest overall salinities 19.7 to 23.2 wt% $NaCl_{eq.}$ based on T_m^{ice} from -22.3 to -16.3 ^oC, and lowest overall values of Th_{total} from homogenization temperatures ranging from 58.9 to 66.1 ^oC.

Figure 4.12 summarizes the results of all microthermometry on a diagram showing Th_{total} vs. bulk salinity, with each fluid inclusion type/subtype shown. The diagram shows a continuous cooling and mixing trend, with low salinity fluid, followed by the influx of cooler, more saline fluid that will be discussed in detail below.

No microthermometric measurements could be obtained for type III inclusions (optically single phase aqueous, low-density at room T, vapour-rich, and containing trace CH_4 and N_2 based on Raman spectroscopy).

Figure 4.10 (following page): Microthermometric results for type I fluid (carbonic-aqueous) by FIA, showing (B) salinity, (A) total homogenization temperatures Th_{total}, and (C) homogenization temperatures of the carbonic phase Th_{carb}. The data show real variations in temperature and salinity, from FIA to FIA, but are relatively consistent within individual FIA with a few exceptions, attributed to post-entrapment modification or an error in assignment to a specific FIA petrographically. Variations in bulk salinity from FIA to FIA indicates mixing of fluids with variable salinity. Varying density of the carbonic phase and variations in Th_{total} (when observations combined) indicate fluctuations in confining pressure and or temperature during entrapment.

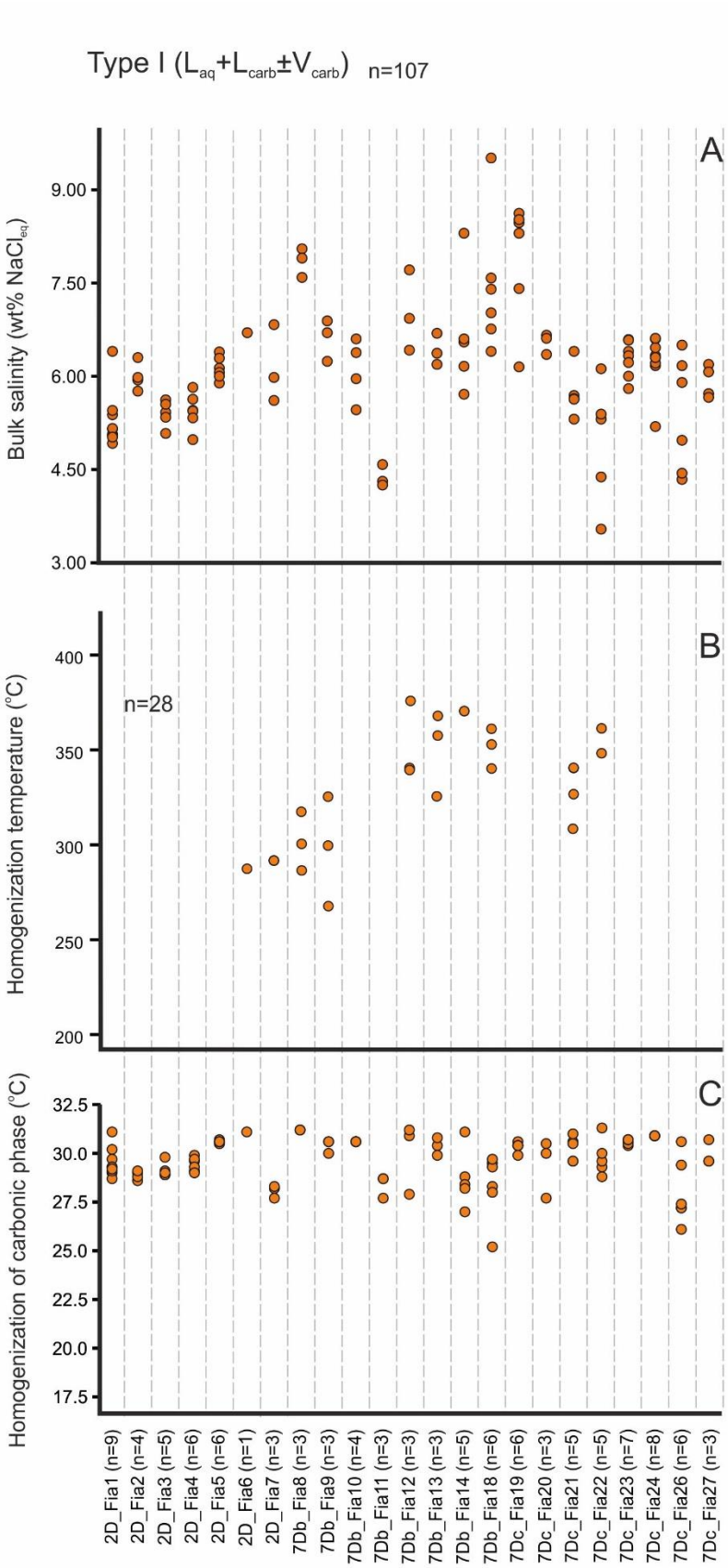
Type I (L_{aq}+L_{carb}±V_{carb}) n=107
A
Bulk salinity (wt% $NaCl_{eq}$)
9.00
7.50
6.00
4.50
3.00
B
Homogenization temperature (°C)
n=28
400
350
300
250
200
C
Homogenization of carbonic phase (°C)
32.5
30.0
27.5
25.0
22.5
20.0
17.5
2D_Fia1 (n=9)
2D_Fia2 (n=4)
2D_Fia3 (n=5)
2D_Fia4 (n=6)
2D_Fia5 (n=6)
2D_Fia6 (n=1)
2D_Fia7 (n=3)
7Db_Fia8 (n=3)
7Db_Fia9 (n=3)
7Db_Fia10 (n=4)
7Db_Fia11 (n=3)
7Db_Fia12 (n=3)
7Db_Fia13 (n=3)
7Db_Fia14 (n=5)
7Db_Fia18 (n=6)
7Dc_Fia19 (n=6)
7Dc_Fia20 (n=3)
7Dc_Fia21 (n=5)
7Dc_Fia22 (n=5)
7Dc_Fia23 (n=7)
7Dc_Fia24 (n=8)
7Dc_Fia26 (n=6)
7Dc_Fia27 (n=3)

Figure 4.11 (following page): Microthermometric results for type II fluid (aqueous) by FIA, showing (B) salinity and (A) total homogenization temperature Th. The diagram depicts real variations from FIA to FIA in temperature and salinity, as the values range from FIA to FIA, but stay consistent within individual FIA with a few exceptions attributed to post-entrapment modification or an error in assignment to specific FIA petrographically. Type IIb inclusions, hosted in calcite and sphalerite, show two distinct groups: *low salinity* calcite-hosted assemblages (1D_FIA1 and 1D_FIA2) and *high salinity* calcite- and sphalerite-hosted assemblages (1D_FIA4 and sph). Low salinity type IIa and type IIb fluids are pre- to syn-mineralization and provide the best estimates for conditions during or immediately prior to, and during, Cu-Ag-Zn-Pb precipitation, respectively.

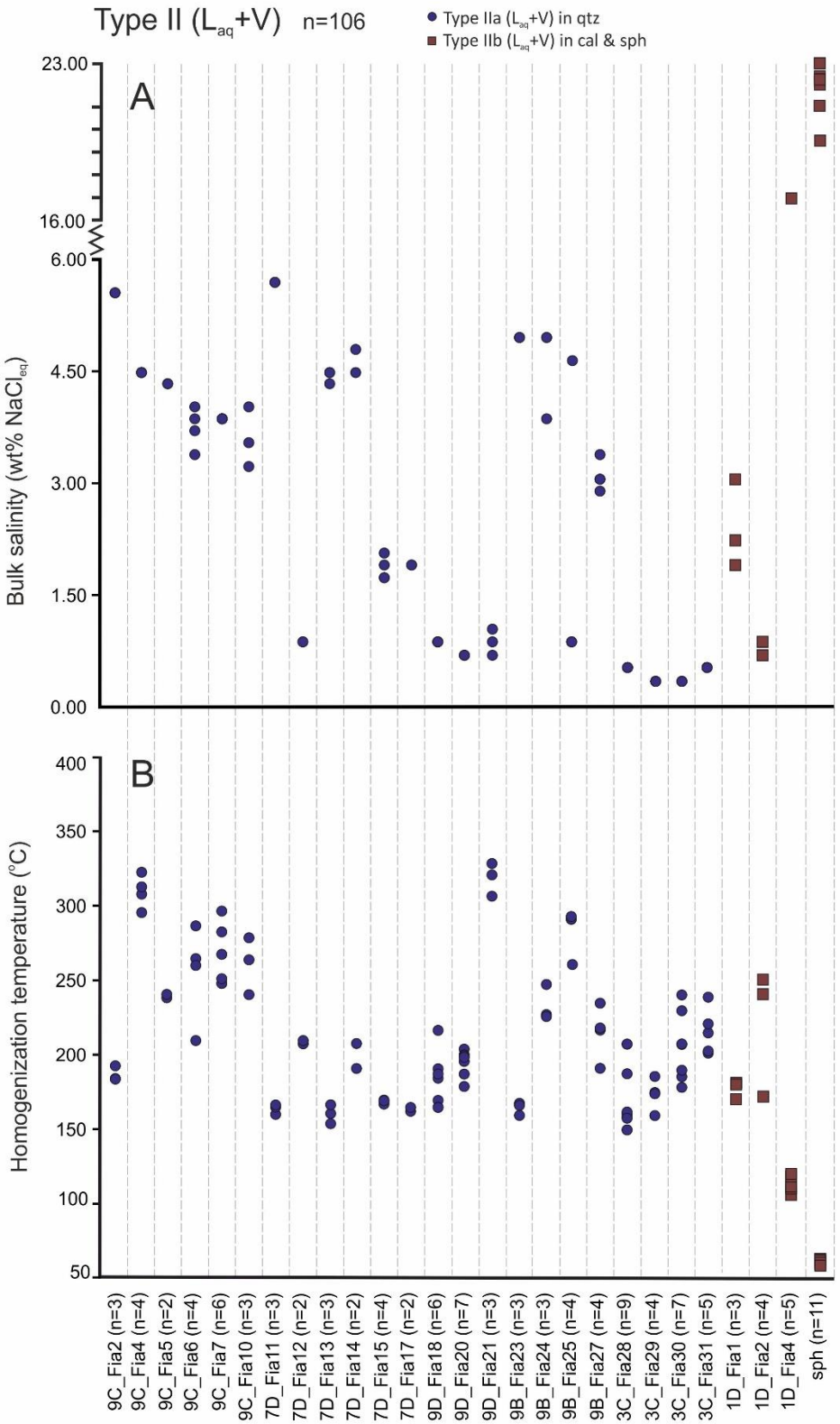
Type II (L_{aq}+V) n=106
Type IIa (L_{aq}+V) in qtz
Type IIb (L_{aq}+V) in cal & sph
A
B
Bulk salinity (wt% $NaCl_{eq}$)
Homogenization temperature (°C)
23.00
16.00
6.00
4.50
3.00
1.50
0.00
400
350
300
250
200
150
100
50
9C_Fia2 (n=3)
9C_Fia4 (n=4)
9C_Fia5 (n=2)
9C_Fia6 (n=4)
9C_Fia7 (n=6)
9C_Fia10 (n=3)
7D_Fia11 (n=3)
7D_Fia12 (n=2)
7D_Fia13 (n=3)
7D_Fia14 (n=2)
7D_Fia15 (n=4)
7D_Fia17 (n=2)
9D_Fia18 (n=6)
9D_Fia20 (n=7)
9D_Fia21 (n=3)
9B_Fia23 (n=3)
9B_Fia24 (n=3)
9B_Fia25 (n=4)
9B_Fia27 (n=4)
3C_Fia28 (n=9)
3C_Fia29 (n=4)
3C_Fia30 (n=7)
3C_Fia31 (n=5)
1D_Fia1 (n=3)
1D_Fia2 (n=4)
1D_Fia4 (n=5)
sph (n=11)

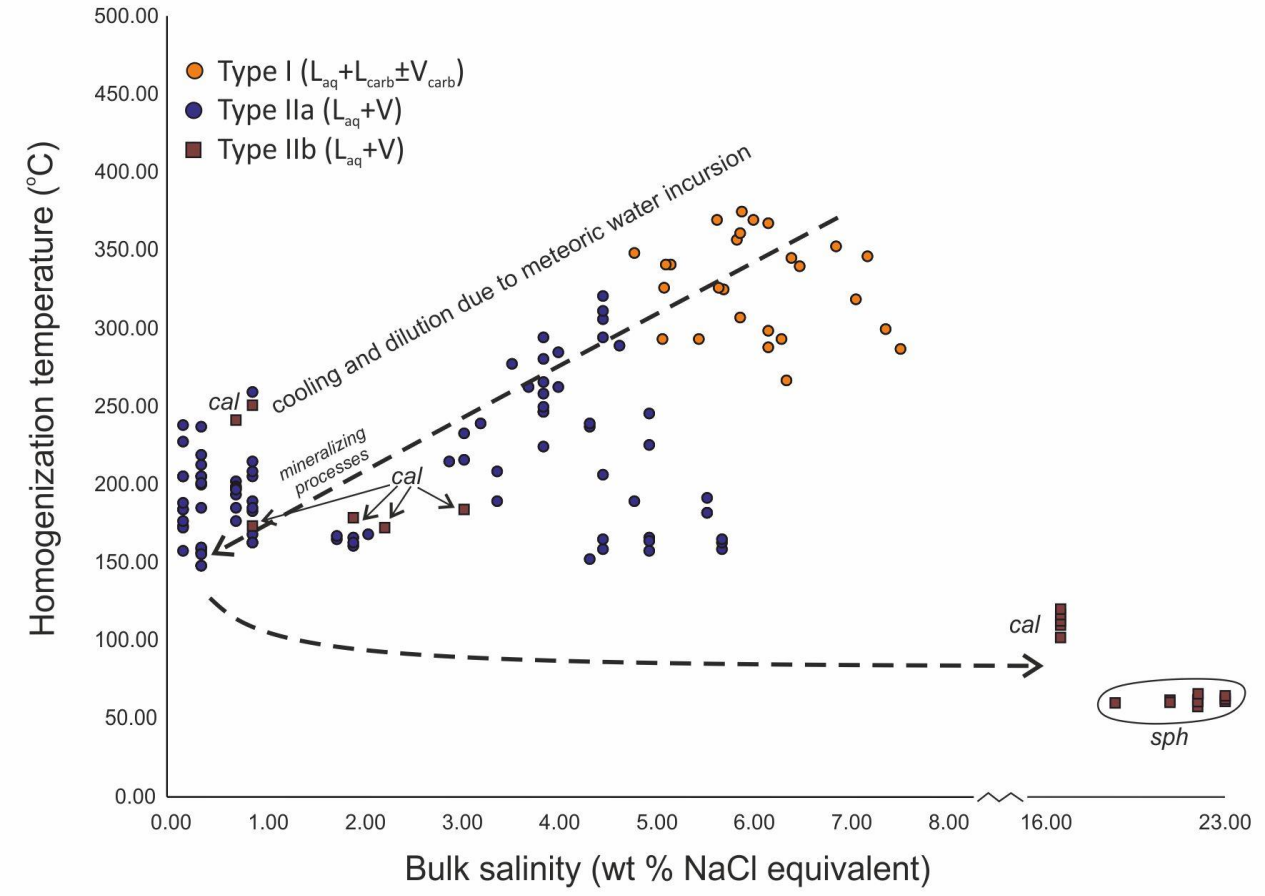

Figure 4.12: Fluid evolution portrayed on a minimum temperature (Th_{total}) vs. salinity (wt % NaCl eq.) diagram summarizing fluid inclusion microthermometry data, showcasing cooling and dilution of the evolution hydrothermal system. Mineralizing fluids are represented at the lower left of the diagram where low salinity type IIa and low salinity type IIb data are plotted. Low salinity type IIb fluid inclusions hosted in calcite are unambiguously syn-mineralization (coeval with sulfide) and type IIa inclusions occurring in healed fractures in quartz overlap in composition-T space with the calcite-hosted inclusions at low T and salinity, suggesting they are coeval. Data for type III inclusions are not available but these V-rich inclusions are interpreted to be broadly

synchronous to type IIa and IIb low salinity inclusions, formed during decompression of type IIa or IIb (low salinity) fluids resulting in flash boiling, and synchronous with mineralization (based on textures revealed from CL imaging). High salinity type IIb hosted in calcite and sphalerite represent an influx of a late highly saline low temperature fluid into the system, post mineralization (bottom right corner of the diagram).

4.7 Laser Ar-Ar and Re-Os age dating

The complete results of laser Ar-Ar age dating are presented in Table 7. All diagrams were made with the Isoplot R program (Vermeesch, 2018) and show a weighted mean age by sample (Figure 4.13). All uncertainties are quoted at the approximate 100(1-α) % confidence interval, confidence interval for t with overdispersion, calculated as z = y√MSWD (not reported for random effects models).

Weighted mean ages for muscovite in samples SAL-4F (n=21), SAL-4I (n=11) and SAL-4E (n=3) are 1827.6 ± 3 Ma (Figure 4.13A), 1835.1 ± 3 Ma (Figure 4.13B), 1830.4 ± 14 (Figure 4.13D), respectively. Sample SAL-4 is a mineralized (massive bornite and disseminated chalcopyrite) granitic gneiss sample. Grains chosen for analyses are coarse-grained vug-infilling muscovites, embedded in sulfides within a quartz vein.

Weighted mean ages for muscovite in samples SAL-8A (n=11), SAL-8B (n=12) are 1830.2 ± 4 Ma (Figure 4.13C) and 1836.0 ± 5 Ma (Figure 4.13E), respectively. These grains are from sample SAL-8, which is a quartz vein in a heavily mineralized meta-arkose. Grains of muscovite are coarse and occur embedded in sulfide (chalcopyrite), and vug-infilling mineralized veins. The overall weighted mean age of muscovite in association with Cu-Fe sulfides considering all grains analyzed is 1831 ± 2 Ma (n=58).

Compared to muscovite, wallrock biotite grains (n=22) from the samples SAL-4F, SAL-3B and SAL-4E yielded similar ages.

Weighted mean age of 4 biotite grains from the sample SAL-4F is 1838.4 ± 6 (Figure 4.13F) and weighted mean age of 2 biotite grains from SAL-4E is 1836.3 ± 6 Ma (Figure 4.13H). In sample SAL-4 wallrock biotite grains occur at the vein margins of a mineralized granitic gneiss.

Weighted mean age of 16 biotite grains from the sample SAL-3B is 1814.31 ± 3.1 Ma (Figure 4.13G). Sample SAL-3 is an alkali granite sample with disseminated chalcopyrite and pyrite, grains of biotite occur in the wall-rock, away from the mineralization.

A single Re-Os age for pure molybdenite separated from its textural settings, embedded in sulfides and muscovite along quartz-sulfide boundaries from sample SAL-HF-14. The calculated age is much older than muscovite and biotite ages. The age of this molybdenite, with uncertainty quoted at 2σ, including all known uncertainties (including α ~ 0.31% uncertainty in the decay constant of ^{187}Re), is 1884 ± 8 Ma (n=1).

Figure 4.13 (following page): Weighted mean ages from the laser Ar-Ar age dating of mineralized vein-related muscovite (A-E) and wall-rock biotite (F-H) grains, plotted using Isoplot R software.

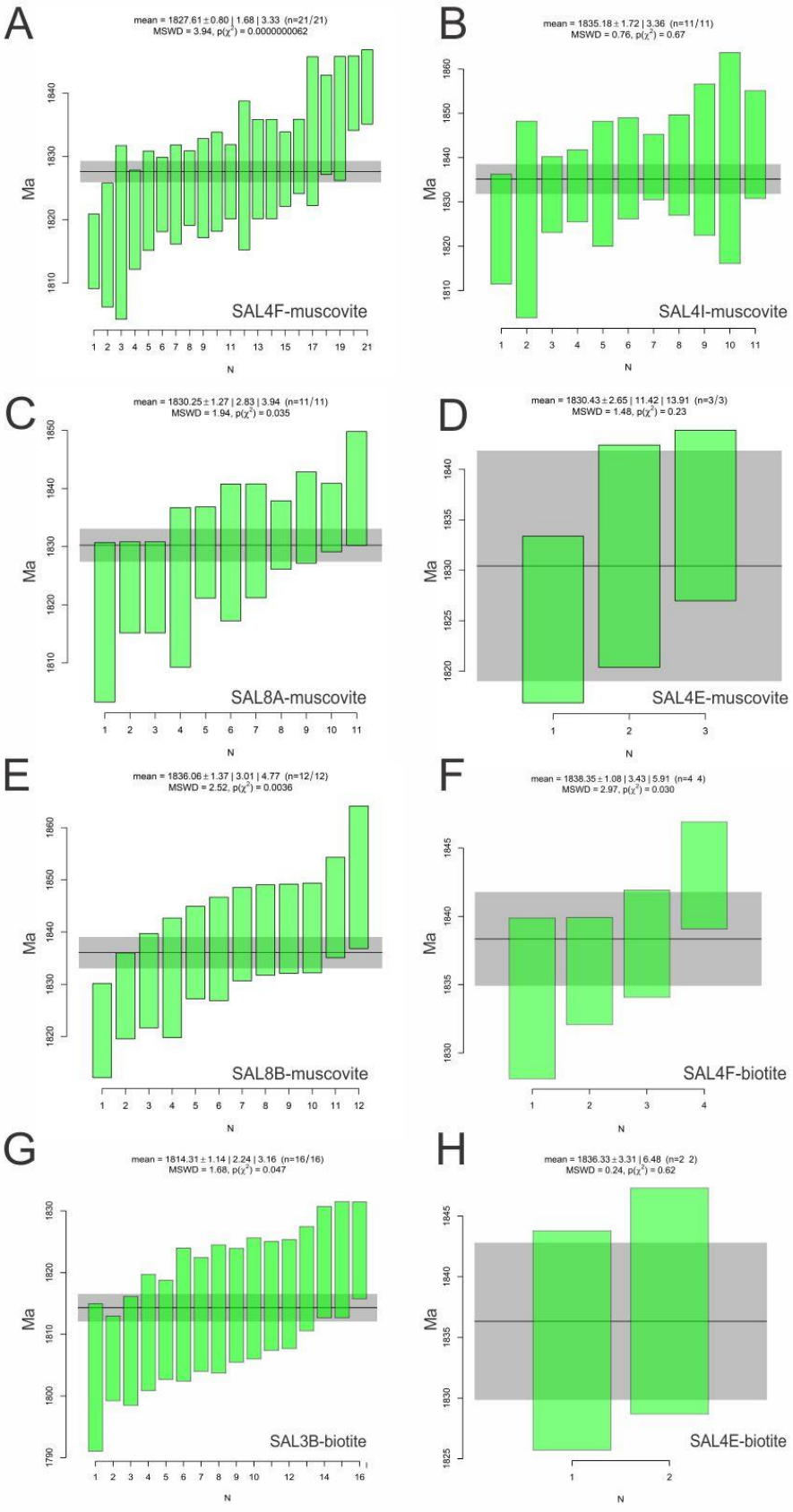
A
mean = 1827.61 ± 0.80 | 1.68 | 3.33 (n=21/21)
MSWD = 3.94, p(χ²) = 0.0000000062
SAL4F-muscovite
B
mean = 1835.18 ± 1.72 | 3.36 (n=11/11)
MSWD = 0.76, p(χ²) = 0.67
SAL4I-muscovite
C
mean = 1830.25 ± 1.27 | 2.83 | 3.94 (n=11/11)
MSWD = 1.94, p(χ²) = 0.035
SAL8A-muscovite
D
mean = 1830.43 ± 2.65 | 11.42 | 13.91 (n=3/3)
MSWD = 1.48, p(χ²) = 0.23
SAL4E-muscovite
E
mean = 1836.06 ± 1.37 | 3.01 | 4.77 (n=12/12)
MSWD = 2.52, p(χ²) = 0.0036
SAL8B-muscovite
F
mean = 1838.35 ± 1.08 | 3.43 | 5.91 (n=4 4)
MSWD = 2.97, p(χ²) = 0.030
SAL4F-biotite
G
mean = 1814.31 ± 1.14 | 2.24 | 3.16 (n=16/16)
MSWD = 1.68, p(χ²) = 0.047
SAL3B-biotite
H
mean = 1836.33 ± 3.31 | 6.48 (n=2 2)
MSWD = 0.24, p(χ²) = 0.62
SAL4E-biotite
Ma
N

4.8 SIMS S and O isotope analysis

The S isotope composition of chalcopyrite is summarized in Table 9, for sample SAL-5. The data range is $\delta^{34}S_{V\text{-}CDT}$ = -9.8 – -11.4 ‰ and yields a mean $\delta^{34}S_{V\text{-}CDT}$ (‰) value of -10.6 ‰, based on 22 analyses.

In-situ O spot isotope compositions were obtained for 52 spots within the 4 different quartz generations, with domains for analysis identified using CL. The data are summarized in Table 10. As the generations cannot be distinguished by optical microscopy, the spots were chosen using CL imaging to locate spots for analysis on transmitted and reflected light images, to ensure that single analyses could be tied to a specific quartz generation. Type I, 1st generation quartz yielded three analyses from one sample with $\delta^{18}O_{V\text{-}SMOW}$ values ranging from 11.2 to 12.1 ‰. Type II, 2nd generation, non-luminescing, “black” quartz not in contact with calcite (“distal” to calcite) has $\delta^{18}O_{VSMOW}$ values ranging from 7.8 to 13.3 ‰ (mean = 10.2 ‰, n=26). Type II quartz, in contact with calcite, (spots in quartz less than 80 µm from calcite-quartz contacts), yielded a mean value of 8.3 ‰ (n=20), and range from 6.8 ‰ to 10.6 ‰. Type III, 3rd generation, yellow-luminescing quartz has $\delta^{18}O_{V\text{-}SMOW}$ values ranging from 7.4 ‰ to 12.6 ‰ (mean = 10.1 ‰, n= 26). Type IV, 4th generation, dim-blue luminescing quartz showed mean value of 12.8 ‰ (n=16) and range from 10.3 to 15.3 ‰.

The O isotopic composition of calcite, filling vugs in quartz and texturally coeval with Cu-Fe sulfides, ranges $\delta^{18}O_{V\text{-}SMOW}$ = 4.7 ‰ – 9.8 ‰, with a mean value of 6.8 ‰ (n=23). The calcite analyses coincided to the same areas as for type II quartz, analyzed adjacent to calcite (i.e., quartz-calcite pairs).

Oxygen isotope fluid values were estimated, based on the microthermometric data, using the stable isotope fractionation calculator “AlphaDelta” (Beaudoin and Therrien; 2004) and are summarized in Table 10. For type II quartz distal and adjacent to calcite, and calcite values for these calculations were constrained by the fluid inclusion microthermometric T results. All calculated $\delta^{18}O_{V\text{-}SMOW}$ values for fluid are minimum values for relevant quartz generations because Th values are used to calculate the isotope values for the equilibrating fluids are minimums. For type II quartz, distal to calcite, the maximum and minimum Th_{total} of the type I carbonic-aqueous fluid was used, (375 and 267 ^{o}C, respectively). For syn-mineralization calcite and calcite adjacent quartz, the maximum and minimum Th_{total} of type IIb low-salinity, aqueous fluid were used (173 and 251 ^{o}C). For type II quartz distal to calcite, calculated $\delta^{18}O_{V\text{-}SMOW}$ values for the equilibrating fluid ranged from -0.4 to 8.5 ‰. Adjacent to calcite, calculated type II quartz $\delta^{18}O_{V\text{-}SMOW}$ fluid values ranged from -6.9 to 1.7 ‰.

For type III quartz, enveloping sulfide mineralization, the results of sphalerite thermometry (153 to184 ^{o}C) were used. This approach is justified by the association of sphalerite and type II quartz with the mineralizing event. Type III quartz-related $\delta^{18}O_{V\text{-}SMOW}$ fluid values were calculated to have ranged from -8.0 to 0.5 ‰. Finally, calcite-related $\delta^{18}O_{V\text{-}SMOW}$ fluid (also syn-mineralization) values ranged from -2.6 to -1.3 ‰. Calculated O isotope values for the mineralizing fluid are best estimated from the mineralization-related type III quartz and calcite calculations and ranged from -8 to 0‰. While calcite-based values are minimums, calculated fluid values for type III quartz, based on the sphalerite thermometry, are considered absolute compositions for the mineralizing fluid. A shift to lower $\delta^{18}O_{V\text{-}SMOW}$ values is noted in type II quartz transitioning from distal

to adjacent to calcite; This is consistent with re-equilibration of the type II quartz (that texturally predates mineralization) with the mineralizing fluid that entered cavities and vugs in type II quartz, now filled with calcite and sulfides. The values from quartz adjacent to calcite overlap with calculated values for type III quartz and calcite. The $\delta^{18}O_{V\text{-}SMOW}$ values of all of the quartz types, calcite and the calculated fluids are summarized in Figure 4.14. A significant decrease in $\delta^{18}O_{V\text{-}SMOW}$ values is seen as the system transitions from type I quartz to type II quartz (adjacent to calcite) to type III quartz and calcite, within the minerals and in calculated fluid compositions.

Figure 4.14 (following page): Oxygen isotopic composition of quartz and calcite, and estimated fluid O isotope compositions from mineralized veins. Box-whisker plot shows measured (SIMS) $\delta^{18}O_{V\text{-}SMOW}$ values for the four types of wall-rock and vein quartz, colour-coded according to their CL luminescence (type I = bright blue, wall-rock; type II = black, vein; type III = yellow, vein; type IV = dim blue, vein), calcite and corresponding calculated fluid $\delta^{18}O_{V\text{-}SMOW}$ values. Type II quartz $\delta^{18}O_{V\text{-}SMOW}$ values have been divided into two separate groups according to the spatial association with calcite (*a* = massive quartz, distal to calcite; *b* = vuggy quartz, immediately adjacent to (in contact with) calcite-sulfide-filled cavities). With the exception of type III quartz, all the fluid calculations were done using the various temperature constraints. Fractionation equations used were for quartz-H_2O equilibration from Sharp et al. (2016) and for calcite-H_2O equilibration from Horta et al. (2014). The following approaches were used: for type II quartz ("a,1"), distal to calcite-sulfide-filled vugs, two ranges in fluid values were calculated using the maximum and minimum Th_{total} for type I fluid inclusions combined with the range in measured $\delta^{18}O_{V\text{-}SMOW}$ from type II quartz. For type II quartz ("b, 2"), adjacent to calcite-sulfide filled vugs, two ranges are shown, but fluid inclusion Th_{total} values are from type IIb primary, low salinity aqueous inclusions hosted in calcite as these T are considered to be more appropriate minimum conditions for fluid-quartz isotope exchange close to these vugs. In both cases, the calculated fluid value ranges are minimums, as maximum and minimum Th_{total} values used in the calculation represent minimum trapping temperatures of the fluid. For type III quartz (3) which is genetically linked to sulfides the temperature constraints used for the calculations are considered to be absolute values, based on minimum and maximum temperature from sphalerite

thermometry, not fluid inclusion data. Again, two ranges in fluid values are calculated combining the range in measured $\delta^{18}O_{V\text{-}SMOW}$ from type II quartz and the sphalerite min and max T. For calcite (“4”) fluid values were calculated using the minimum and maximum Th_{total} from type IIb primary, low salinity aqueous inclusions, hosted in calcite. Like in the case of quartz calculations, these are also minimum values.

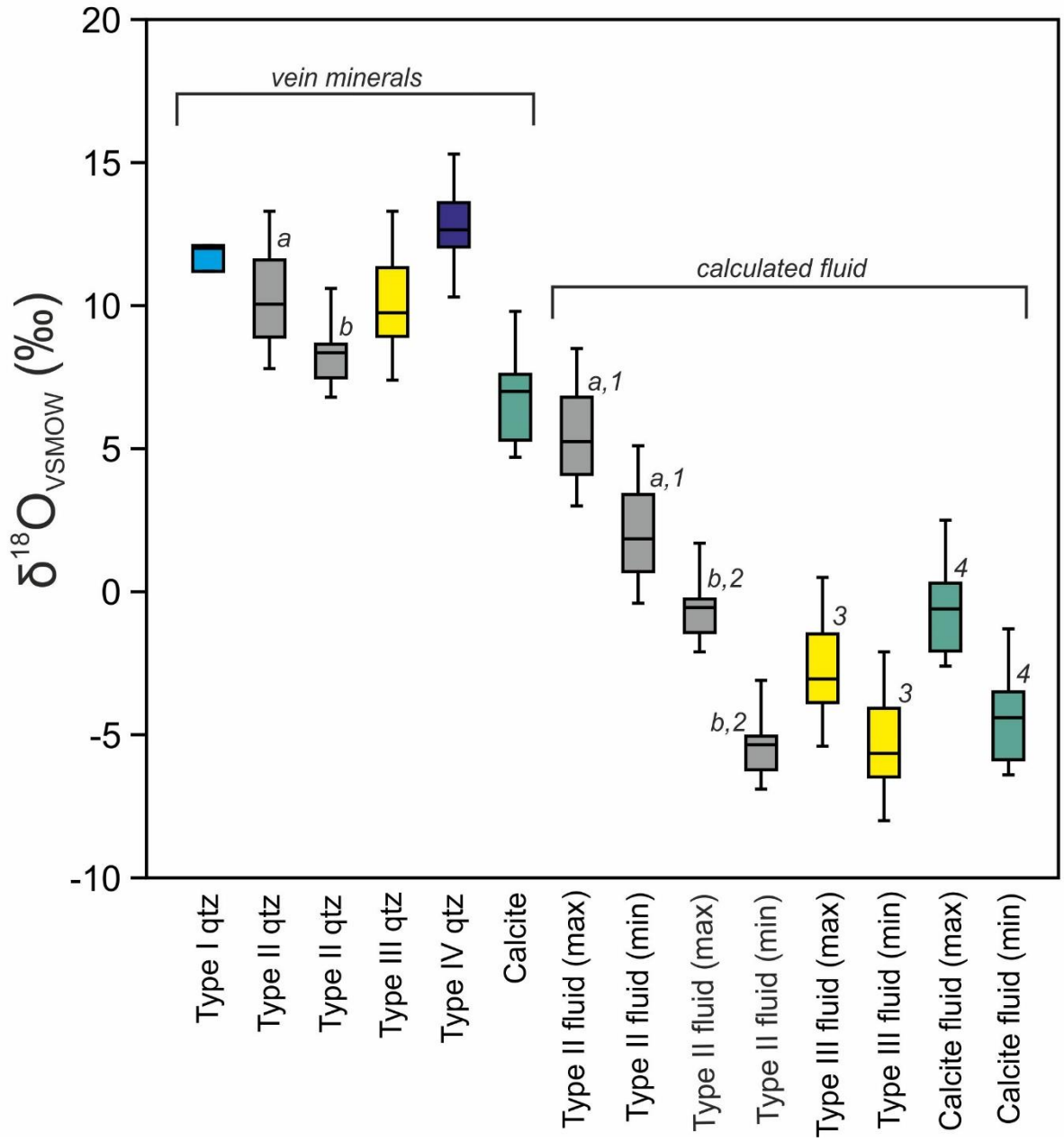
20
15
10
5
0
-5
-10
δ18OVSMOW (‰)
vein minerals
calculated fluid
a
b
a,1
a,1
b,2
b,2
3
3
4
4
Type I qtz
Type II qtz
Type II qtz
Type III qtz
Type IV qtz
Calcite
Type II fluid (max)
Type II fluid (min)
Type II fluid (max)
Type II fluid (min)
Type III fluid (max)
Type III fluid (min)
Calcite fluid (max)
Calcite fluid (min)

Chapter 5: Discussion

5.1 Field observations and cross-cutting relationships

Combining observations from the field, (e.g., cross-cutting relations, macroscopic textures), reveals the relative timing of the mineralization. It is evident from various sulfide textures (e.g., fracture fillings, vein vug fill, undeformed disseminations, breccia matrix infilling) that the mineralization post-dates all three host rock types and the ductile deformation that sheared quartz clasts in granitic gneiss (Figure 4.2F). Quartz clasts indicate a left-lateral sense of shear, but disseminated chalcopyrite shows no evidence of deformation, occurring within fractures. Mineralization post-dates the host rock foliation along the quartz-sulfide breccia contacts with the host rock (Figure 4.1A-B). Early quartz veins pre-date the mineralization and brittle deformation since chalcopyrite-bornite infills vugs within intact quartz veins (Figure 4.2B). There is evidence of a brittle deformation event(s) that created porosity and permeability for the metal-rich fluids to infiltrate and precipitate. This is seen in the heavily mineralized incohesive quartz-sulfide breccia free of any host-rock clasts. It is likely that this breccia was derived from as coherent quartz veins and mineralization may have been timed with the brecciation of the veins. Alternatively, sulfide mineralization may have post-dated both ductile and brittle and took advantage of earlier structures.

5.2 Paragenetic sequence

The construction of a paragenesis for the Salkeld Lake mineralization sequence is an integral part of the classification and model development. Understanding the difference between the mineral sequences in the surface and core samples, the relationship between alteration mineralogy and mineralization, as well as the timing of the fluids based

on petrographic observations allows constraints on relative timing and possible conditions of mineralization to be established. For example, precipitation and dissolution of sulfides is sensitive to, and can be controlled by, variables such as pH, oxygen fugacity (fO_2) and temperature (e.g., Reed and Palandri, 2006). The mineralization history, based on textural and petrographic observations, has been divided into four stages, and reflects the differences between the surface and drill core samples (Figure 5.1).

5.2.1 Pre-veining stage

The pre-veining stage encompasses wall rock minerals, including type I quartz, which remains preserved as brecciated, partly resorbed and dissolved crystals in some of the mineralized veins. Type I quartz is presumed to be coeval with other host rock minerals (metamorphic or magmatic biotite and k-feldspar) and is abundant in all host rock lithologies. The bright blue luminescence of type I quartz indicates its magmatic or metamorphic origin (Götze, 2001). Grains of molybdenite, occur as inclusions in Cu-Fe sulfides but also as relict grains in muscovite, and along type I and II quartz grain boundaries. Based on petrographic evidence alone, the timing of molybdenite is ambiguous and can be only inferred to be early relative to the sulfide precipitation. However, Re-Os age dating firmly sets this mineral in the pre-veining stage, linked to some earlier non-Cu mineralizing event at Salkeld Lake (see section 5.5).

5.2.2 Veining and mineralization stage

During the veining stage, the 2nd generation (type II) quartz replaces 1st generation (type 1) quartz (Figure 4.8C). This was a barren vein stage immediately preceding the mineralization. Muscovite, epidote and adularia grew during this veining, prior to sulfide

deposition. Fluorite is the earliest accessory mineral, coeval with epidote, muscovite and adularia in this stage.

As the system evolved, brecciation, fracturing, and dissolution of type I and II quartz occurred over the transition into the mineralization stage, which produced 3rd generation (type III) quartz (Figure 4.8G) and was followed by, or synchronous to, calcite. Type III quartz luminesces bright yellow, which occurs in low-temperature (~250 ^{o}C) hydrothermal systems, related to fast crystallization in environments with oxygen deficiency (Götze, 2015).

The base metal sulfides chalcopyrite, idaite, sphalerite and galena may have been coeval with sulfides or were the earliest sulfides in the mineralizing stage. Native silver occurred early as well, prior to these early sulfides as it is included or partly included in the sulfides and calcite. However, Ag mineralization was also clearly coeval with sulfides since Ag-enrichment is noted in chalcopyrite, bornite and chalcocite (SEM/EPMA). Post-mineralization deformation and metamorphism were minimal, therefore, mutual grain boundary textures indicate that these minerals, as well as tetrahedrite and calcite must have precipitated at approximately the same time. Bornite replaced chalcopyrite by rim, island-mainland and boxwork type replacement. Often secondary sulfides precipitated in the form of chalcocite-djurleite-digenite, followed by spionkopite, yarrowite and covellite. Yarrowite and covellite often create a net/“spider-web” texture replacing bornite, chalcopyrite and idaite, and also occupy fractures within these minerals. This mineral sequence is evident from sequential rim replacement textures that occur in the majority of samples, that follows a precipitation path from chalcopyrite to covellite (Figure 4.3A).

5.2.3 Surface oxidation stage

Late surface oxidation is most evident in hand samples and at the outcrop scale (Figure 4.1C). Tenorite, malachite and azurite staining is pervasive and only occurs in the surface samples. It is not related to the main mineralization stage, but rather surface oxidation after the rocks were exhumed.

Figure 5.1 (following page): A four-stage paragenesis of the Salkeld Lake mineralization including the surface and DDH mineral sequence. Stage 0 represented the earliest pre-veining stage, consisting of the host rock 1st generation qtz, bt and k-fsp, and possibly mol. Veining **stage I** introduced 2nd generation qtz and carbonic-aqueous type I fluid into the system, along with muscovite that is coarsening in grain size over time, as well as epidote and adularia. Brecciation occured as the system enters mineralizing **stage II** that involves precipitation of the 3rd generation qtz and the type IIa, IIb (low salinity) and type III fluids, followed by the late-stage high salinity type IIb. During this stage calcite is precipitated along with the primary (cpy-id-ga-sph) and secondary (bn-cc-dg-yar-cov) sulfide sequence from sph to cov. Late oxidation during **stage III** yields ten, mal and az. Question marks indicate that the textural evidence for the first appearance of a phase is suggestive but less certain. Mineral abbreviations: ad = adularia; az = azurite; bn = bornite; bt = biotite; cal = calcite; cc = chalcocite; cpy = chalcopyrite; cov = covellite; dg = digenite; ep = epidote; FI = fluid inclusion; fl = fluorite; ga = galena; high sal = high salinity; id = idaite; k-fsp = potassium-feldspar; low sal = low salinity; mal = malachite; mol = molybdenite; musc = muscovite; py = pyrite; qtz = quartz; silver = native silver; sph = sphalerite; spn = spionkopite; tetr = tetrahedrite; ten = tenorite; yar = yarrowite.

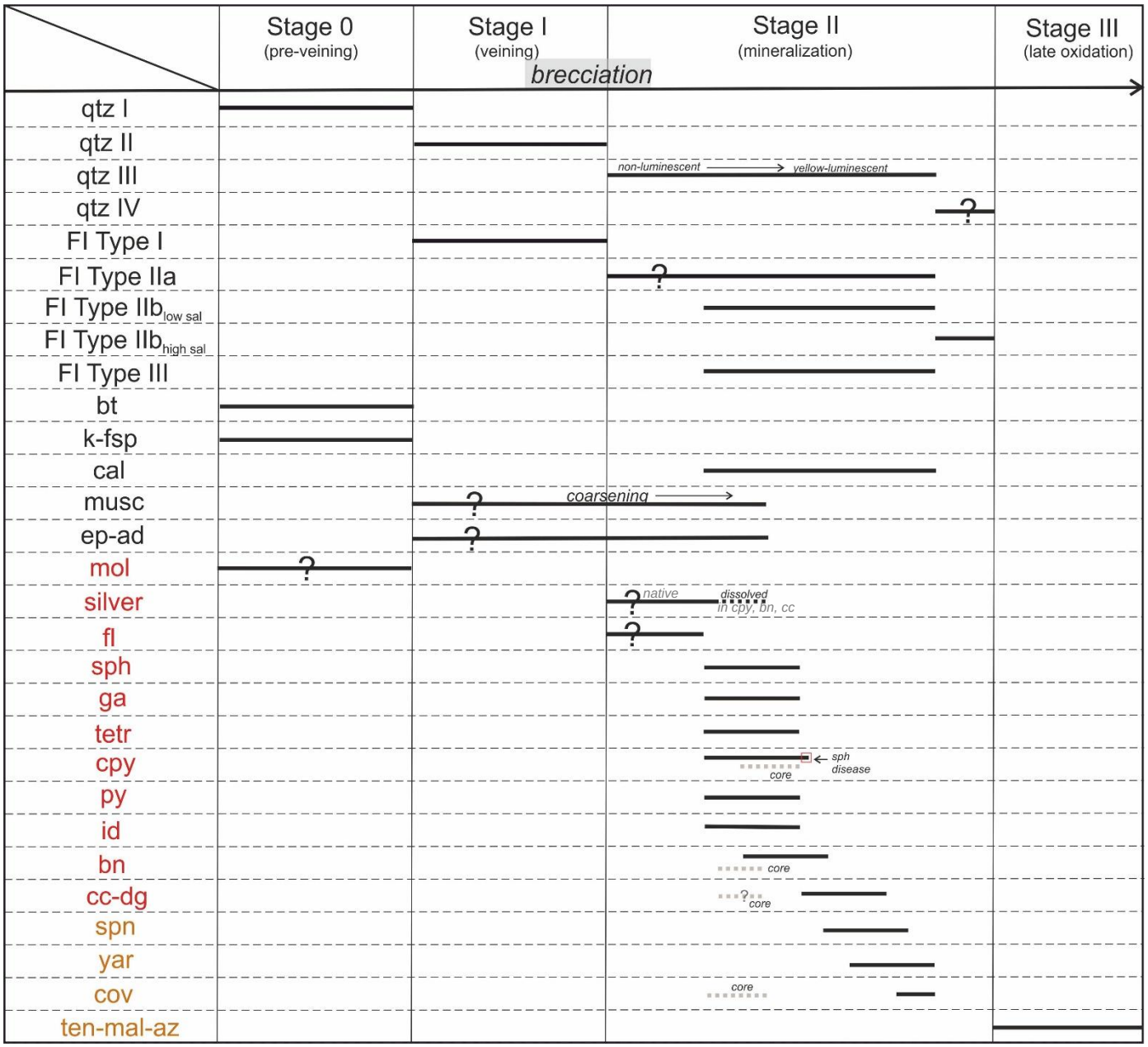
Stage 0
(pre-veining)
Stage I
(veining)
Stage II
(mineralization)
Stage III
(late oxidation)
brecciation
qtz I
qtz II
qtz III
non-luminescent
yellow-luminescent
qtz IV
FI Type I
FI Type IIa
FI Type IIb low sal
FI Type IIb high sal
FI Type III
bt
k-fsp
cal
musc
coarsening
ep-ad
mol
silver
native
dissolved
in cpy, bn, cc
fl
sph
ga
tetr
cpy
sph
disease
core
py
id
bn
core
cc-dg
core
spn
yar
cov
core
ten-mal-az

5.3 Sulfide chemistry

After examining the mineralogical evidence, there are significant paragenetic differences between the samples taken from the surface trenches and outcrops and the DDH core samples. Core samples from some mineralized stratigraphic units as at surface lack specific base metal minerals (sphalerite and galena), and although the textures are similar (e.g., rim replacement), the order of sulfide mineral precipitation is reversed (covellite and bornite were replaced by chalcopyrite, and chalcocite was replaced by bornite; Figure 4.3I-L). Idaite, spionkopite and yarrowite are exclusive to the surface samples. While these three minerals are common in shallow, low temperature sediment-hosted copper deposits (Hatert, 2005; Demir et al., 2013) (Figure 4.3B, 4.7), their absence in the core samples does not necessarily indicate that they are the products of only late surface oxidation of the Salkeld mineralization during surface weathering. The occurrence of early bornite-chalcocite-covellite replaced by chalcopyrite in core samples, a sequence opposite to that observed in surface samples, indicates that fO_2, pH and other parameters that influence sulfide mineralogy were clearly varying in the mineralizing system at significant depth (100s m), and likewise are not just surface alteration feature. Notably, covellite, (the most oxidized sulfide) occurs both in the surface and core (Figure 4.3A, L), indicating that its growth is not the result of late-stage oxidation, rather it is directly related to the primary metal precipitation event. Calcite, appearing in the paragenesis in the mineralization, is completely absent in the surface samples (Figure 4.5B-C). As well, adularia occurs only in the alteration assemblage in the core samples (Figure 4.5E-F).

Evidently, there must be two opposing parameters (e.g., pH, fO_2, etc.) occurring to drive distinct paragenetic sequences near surface and at depth (cpy→cov vs cov→cpy)

leading to an apparent zonation of the entire mineralized system. Favourable geochemical conditions relevant to the precipitation of both sequences are discussed in the next section.

Although there are insufficient drill hole coverage/data to confirm the existence and morphology of a distinct zonation in the deposit, mineral chemistry and paragenetic sequences have contrasting features that are distinct in the surface and core samples. Changes in pH and fO_2 would have had to occur within the system to drive the sulfide reactions but also trigger transient *reversals* in the major sulfide mineral sequence (cpy,id,ga,sph→bn→cc→cov) vs. (cov→cc→bn→cpy), and explain the presence or lack of calcite co-precipitation with the sulfides.

A pH increase, resulting from fluid neutralization (e.g., via mixing and dilution by meteoric water, or wall-rock reactions that consume $H^+_{(aq)}$) will lead to the precipitation of chalcopyrite, sphalerite and galena, according to the following reactions (Reed and Palandri, 2006):

$$Fe^{2+}_{(aq)} + Cu^{+}_{(aq)} + 1\tfrac{7}{8}HS^{-}_{(aq)} + \tfrac{1}{4}SO_4^{2-}{}_{(aq)} = CuFeS_{2(cpy)} + \tfrac{7}{8}H^{+}_{(aq)} + \tfrac{1}{2}H_2O \quad (3)$$

$$ZnCl^{+}_{(aq)} + HS^{-}_{(aq)} = ZnS_{(sph)} + H^{+}_{(aq)} \quad (4)$$

$$PbCl^{2-}_{4\,(aq)} + HS^{-}_{(aq)} = PbS_{(ga)} + H^{+}_{(aq)} \quad (5)$$

Reactions involving neutralization can also change the speciation of Cu-Fe sulfides, through reactions that may consume pyrite:

$$2CuS_{(cv)} + H_2O_{(aq)} = Cu_2S_{(cc)} + \tfrac{1}{4}SO_4^{2-}{}_{(aq)} + \tfrac{1}{2}H^{+}_{(aq)} + \tfrac{3}{4}H_2S_{(aq)} \quad (6)$$

$$Cu_2S_{(cc)} + FeS_{2(py)} + H_2O_{(aq)} = Cu_5FeS_{4(bn)} + \tfrac{1}{4}SO_4^{2-}{}_{(aq)} + \tfrac{1}{2}H^{+}_{(aq)} + \tfrac{3}{4}H_2S_{(aq)} \quad (7)$$

$$Cu_5FeS_{4(bn)} + 4FeS_{2(py)} + 2H_2O_{(aq)} = 5CuFeS_{2(cp)} + ½SO_4^{2-}{}_{(aq)} + H^+_{(aq)} + 1½H_2S_{(aq)} \quad (8)$$

The consumption of $H^+_{(aq)}$ (pH increase) in each reaction above drives them toward the right-hand side of the mass action expressions, yielding the incremental sequence cov→cc→bn→cpy. This could be a mechanism for Cu-Fe sulfide precipitation in the core samples. However, there is negligible pyrite observed in any of the samples and so it is surprising, if these reactions proceeded as predicted above, that there is not more residual pyrite preserved in the sulfide assemblages that contain the earliest forming minerals in the sequence. Likewise, if the system was to experience a drop in pH (from neutral to acidic) due to the introduction of a new pulse of acidic, metal-bearing fluid, the paragenesis observed in the surface samples (the reverse of what is observed at depth in DDH) could be achieved. However, the complete absence of pyrite in any of the surface samples, a necessary product of the reversal of reactions 6-8 above, suggests these reactions did not occur as they are written above.

Without pyrite involved, a neutralization reaction can precipitate the mineral sequence cpy→bn→cc→cov provided that Fe stays in solution as a hydroxide; this would have to be removed/flushed from the hydrothermal system, as there are no iron oxides or iron hydroxides in the Salkeld Lake mineral assemblages. An example reaction is (Reed and Palandri, 2006):

$$5CuFeS_{2(cpy)} + 14H_2O_{(aq)} =$$

$$Cu_5FeS_{4(bn)} + 4Fe(OH)_3^-{}_{(aq)} + 5½HS^-_{(aq)} + ½SO^{2-}_{4(aq)} + 10½H^+_{(aq)} \quad (9)$$

As stated earlier, these pH fluctuations could occur through simple dilution via mixing of a more acidic fluid with meteoric water, or can be facilitated by the consumption of $H^+_{(aq)}$

through mineral reactions such as formation of muscovite, as observed along the margins of veins and in close association with sulfides at Salkeld Lake:

$$2H^{+}_{(aq)} + 2NaAlSi_3O_{8(ab)} + KAlSi_3O_{8(kf)} = KalSi_3O_{10}(OH)_{2(musc)} + 2Na^{+}_{(aq)} + 6SiO_{2(qtz)}. \quad (10)$$

Again, influx of a more acidic fluid could reverse the reaction in equation (9).

An alternative (or complementary process) to those described above for the paragenetic sequences can be achieved if the system experiences an increase in solely oxygen fugacity (fO_2), and not accompanied by pyrite precipitation. For example,

$$5CuFeS_{2(cpy)} + 12O_2 = Cu_5FeS_{4(bn)} + 6SO_{4(aq)}^{2-}. \quad (11)$$

Similarly, the rest of the paragenetic sequence of the surface samples can be achieved by continually increasing fO_2, whereas a reduction in fO_2 would reverse the sequence as observed in the core samples (Reed & Palandri, 2006).

In summary, to precipitate both the mineral sequences on surface (cpy,id,ga,sph→bn→cc→cov) and observed at depth in the core samples (cov→cc→bn →cpy) the conditions (whether pH or fO_2) must change to cause the sequence reversal. Other indicators of change and/or differences in these conditions is the presence of minerals like idaite, that are common and stable at low temperature and shallow depth (Hatert, 2005), only at the surface, while calcite and adularia are present only in the core samples.

In the interpreted (shallow) center of the mineralized system, represented by the samples collected at the surface (in the absence of pyrite), an incursion of a neutralizing fluid and/or fluid with increased in fO_2 must have prevailed. In the interpreted deep (~80-

150 m) periphery of the system, represented by the core samples, following initial neutralization/oxidation, an influx of acidic and/or reducing fluid explains the observed reversal in mineral sequence less impacted by meteoric water incursion. This reversal is not evident in the surface samples.

Oxygen fugacity and/or pH fluctuations appear to be the most likely mechanism for the sulfide precipitation and variability in sulfide replacement reactions occurring throughout the system (cf. Wohlgemuth-Ueberwasser, 2012; Zhang, 2017).

5.4 Alteration mineralogy

Adularia, occurring in the DDH samples from Salkeld Lake, is common in low- to intermediate-sulfidation epithermal Au-Ag systems (Legault, 2006; Mikaeili et al. 2017; Tombe et al., 2018; Juliani et al., 2021). Epidote is an alteration mineral commonly found in moderately deep mesothermal and porphyry systems with neutral pH, includingshear-hosted mesothermal vein systems (Liu, 2003; Reviews in Mineralogy and Geochemistry, 2004, vol. 56-1). Muscovite characteristically occurs in the main phyllic stage alteration assemblages of high temperature, moderately low pH systems like porphyry deposits (Field, 2005; Wilson, 2006; Reed, 2013). In these systems, muscovite is often coarse-grained and ripened along the vein margins, not unlike muscovite at Salkeld Lake (cf. Runyon et al., 2017, 2019).

However, the specific assemblage of muscovite-epidote-adularia is not well documented in the literature. Individually those minerals can be part of alteration assemblages within a distinct deposit style, but to find these minerals together in equilibrium is unusual. Epidote and adularia can occur together in the inner propylitic zones of the porphyry deposits and mesothermal systems, while muscovite is more

indicative of phyllic alteration zones (Buchanan, 1981; Sillitoe, 1990; White et al., 1995; John et al., 1999; Bath et al., 2014; Corbett, 2018; Wilkinson et al., 2010, 2020).

Based on comparisons with the aforementioned studies the alteration assemblage at Salkeld can be classified as intermediate between phyllic and propylitic, and possibly formed at moderate to high temperatures, at near neutral pH, with characteristics similar to both mesothermal and porphyry systems.

5.5 Fluid evolution and pressure-temperature constraints

Summarizing cross-cutting and spatial relationships seen microscopically, Figure 5.2 shows a generalized representation of a sulfide mineralization within a vein, highlighting quartz generations and fluid inclusion types. The diagram shows the relationships and timing of the quartz generations (according to their CL colours) and fluid inclusion types associated with them, as well as their relationship to the sulfides (shown in red). Type I (1st generation quartz), luminescing bright blue is wall rock-related, and most likely of a high-grade metamorphic or magmatic origin (cf. based on CL colour; Götze, 2001). Type I quartz was replaced, (appearing brecciated/resorbed), by type II (2nd generation) non-luminescing, “black” quartz. Type II quartz hosts type I carbonic-aqueous inclusions, interpreted to be broadly coeval with the host quartz generation. Although the origin is indeterminate for some FIA, others are pseudosecondary and none are secondary. Importantly, those type I inclusions that are pseudosecondary were trapped before type II quartz precipitation concluded in the veins.

Figure 5.2 (following page): An idealized schematic representation of the vein-hosted mineralization at Salkeld Lake. Schematic shows the distribution of the fluid inclusions, their association with the quartz generations, identified using CL, sulfides and other relative phases (e.g., muscovite). Type I blue-luminescing qtz is the host-rock qtz being replaced by the type II non-luminescing qtz, hosting the indeterminate and pseudosecondary type I and secondary type IIa fluid inclusions. Primary, low salinity type IIb fluid inclusions are hosted in calcite. High salinity secondary type IIb inclusions are hosted calcite and sphalerite. Low salinity type IIb fluid is timed with the mineralization. Type III vapour-rich inclusions are associated with the yellow-luminescing, type III qtz (replacing type II), occurring near heavily mineralized zones on a sample scale. 3rd generation qtz can occur as non-luminescing and can rarely host type IIa inclusions. Type IV dim-blue qtz is the rarest type and is only seen replacing type III.

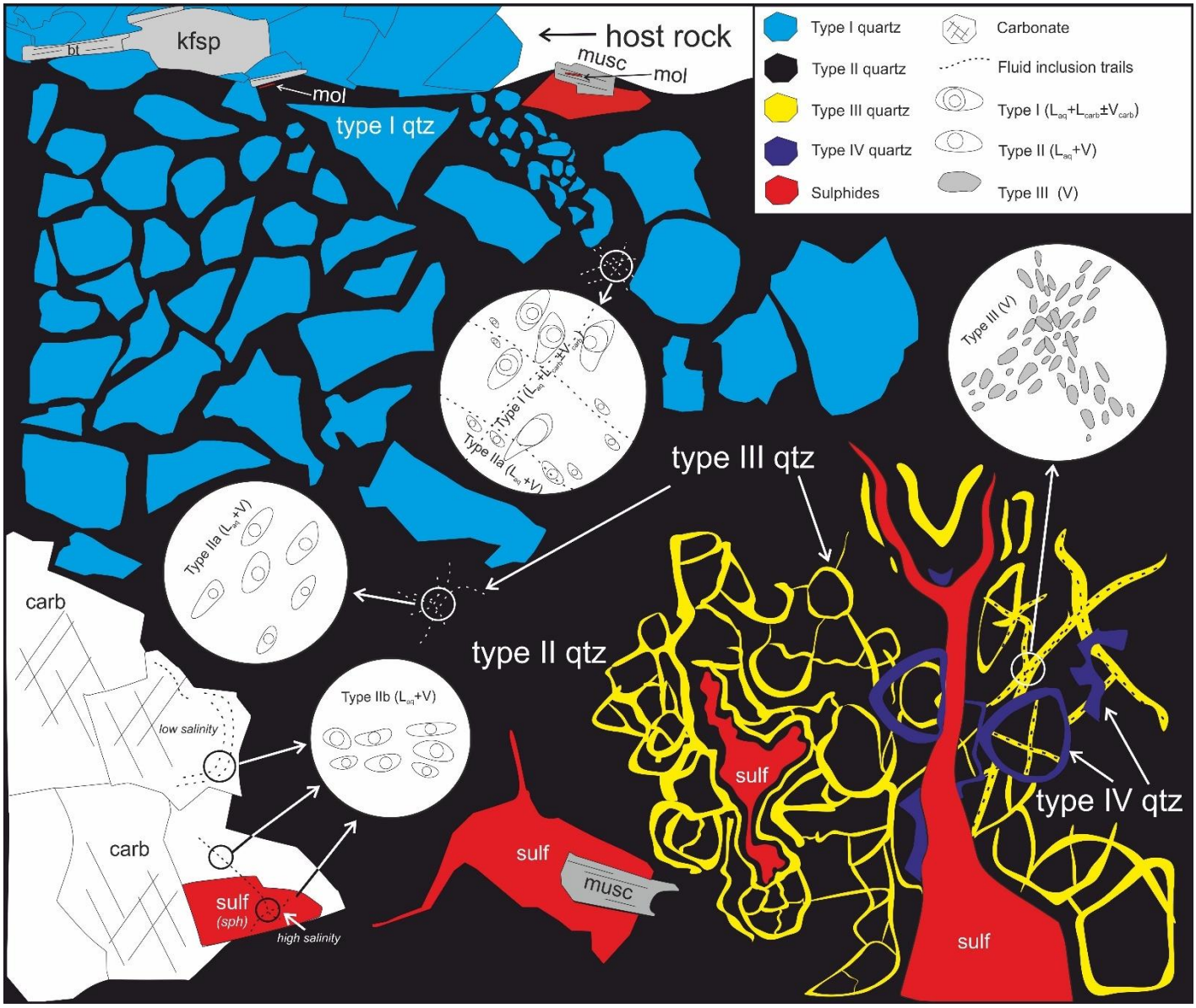
kfsp
bt
mol
type I qtz
host rock
musc
mol
Type I quartz
Type II quartz
Type III quartz
Type IV quartz
Sulphides
Carbonate
Fluid inclusion trails
Type I (Laq+Lcarb±Vcarb)
Type II (Laq+V)
Type III (V)
Type III (V)
type III qtz
Type IIa (Laq+V)
carb
type II qtz
Type IIb (Laq+V)
low salinity
carb
sulf
(sph)
high salinity
sulf
musc
sulf
type IV qtz
sulf

Type IIa, aqueous fluids hosted in type II quartz are low salinity, secondary, are broadly coeval with the syn-mineralization type III quartz, luminescing bright yellow (hydrothermal; Ioannou, 2004; Götze, 2015). Primary inclusions containing type IIb low salinity fluid hosted in calcite, although not having a direct association with a quartz generation must be closely related to type III quartz, and must postdate type II quartz, since the timing of calcite is syn-mineralization. Type III low density vapour-rich fluid inclusions are hosted in both type II and type III quartz, cross-cutting type II quartz, observed as trails in bright yellow luminescing areas, enveloping sulfides. Close association of the low-density vapour-rich fluid with the sulfides indicate that the rapid shallowing and decompression of the system must be related to metal precipitation. Such trails of low-density vapour-like fluid inclusions are typical of rapidly boiling hydrothermal systems ("flashing", cf. Bodnar et al., 2014; Moncada et al., 2017). The exact relationship and timing between type IIa and type III fluids is unclear. However, type IIb primary inclusions in calcite are considered to be related to type III, syn-sulfide mineralization. Decompression of type IIb fluid could produce type III fluid, and this P variation could have fluctuated. There must have been significant variations in pressure, attributed to closure and re-opening of the system to facilitate the decompression and evolution of type III fluid. Resealing of the system again would allow type IIb low salinity fluid (non-flashing) to be trapped in calcite, filling vugs in quartz. Ambiguity is introduced with the 4th generation quartz, luminescing dim blue. Its relationship to aqueous (type IIb high salinity) primary inclusions in calcite or type III fluid is unclear. Secondary inclusions in sphalerite, contain the latest fluids, post-dating mineralization. Microthermometry results for these fluids yielded the highest salinity and lowest temperatures of homogenization.

The quartz, calcite and sphalerite paragenetic sequence, fluid inclusion petrography, and microthermometric data allow for the stages of the fluid evolution in pressure-temperature space to be constrained graphically. To summarize, Figure 5.3 shows the fluid evolution path, from the earliest type I fluid to type III, utilizing the minimum P-T constraints provided by the isochores plotted in the NaCl-CO_2-H2O and NaCl-H_2O systems for type I and type II fluid, respectively. Additionally, Figure 5.3 shows an independent temperature constraint for mineralization based on sphalerite thermometry. High temperature carbonic-aqueous fluid (type I) is diluted through the incursion of meteoric water, decreasing in salinity and temperature to type IIa. The system experiences periods of rapid shallowing, decompression, trapping the mineralization-related type IIb low salinity in calcite and low-density "flashing-type" vapour-rich type III inclusions (trapped on the liquid-vapour curve in the diagram). Finally, a late-stage influx of highly saline low temperature type IIb fluid occurs, trapped in calcite and sphalerite (secondary).

To constrain the P-T conditions of entrapment for some fluid generations, consider first type I inclusions trapped in the single-phase field of the NaCl-CO_2-H_2O system (Schmidt & Bodnar, 2001) shown in Figure 5.3. The minimum trapping conditions of the type I carbonic-aqueous fluid must be no lower than ~300 ^oC and ~1.5 kbar prior to mineralization (lower end of red isochores in Figure 5.3). Type IIa inclusions are trapped in a broad isochore field due to the lack of available P-T constraints to pinpoint the exact P-T conditions. However, it is evident that the trajectories of type I and type IIa isochores overlap enough to suggest there is an evolutionary continuity between the two fluids. Similarly, type IIb low salinity fluids hosted in calcite overlap with the type IIa isochore

field. Combined with microthermometric results, this indicates possibility of a common origin/timing for both fluids. Additional constraints on temperature are available from sphalerite thermometry, the T range of which overlaps with the lower end of the isochore range for type IIb fluid, further supporting the notion of a system that experiences continuous dilution, cooling, rapid shallowing and decompression. A minimum decrease of ~150 ^{o}C and ~1.5 kbar was necessary to evolve from type I carbonic-aqueous to type III low density vapour-rich inclusions, trapped on the liquid-vapour curve (green curve in Figure 5.3). The estimated conditions for the mineralization stage range from 153 to 184 ^{o}C and <700-750 bar, based on the overlapping fields of sphalerite thermometry and isochores of the syn-mineralization type IIb low salinity fluid (yellow field in Figure 5.3). The final increase in salinity and additional cooling was associated with an incursion of a late-stage fluid, post-dating the main stage of the mineralization.

Figure 5.3 (following page): Pressure-temperature plot showing isochore ranges for each fluid type at Salkeld Lake, and related conditions of hydrothermal evolution and mineralization. Type I carbonic-aqueous fluid was trapped in the single-phase field of the diagram along the red isochores (boundaries separating two- and one-phase fields at different bulk salinity and fluid CO_2 contents from Schmidt & Bodnar, 2000). The lowest P-T points on the red isochores correspond to the conditions at homogenization for type I inclusions and represent minimum entrapment conditions. Type IIa aqueous inclusions hosted in quartz were trapped in the broad grey field, showing a significant range in the pressure-temperature conditions. Representative type IIb (low salinity) isochores are plotted within the broader type IIa range, and show overlap suggesting that type IIa and IIb inclusions trapped the same fluid at lower T conditions within this field. An independent temperature constraint (153-184 ^{o}C) was calculated from sphalerite thermometry (pale brown field; Frenzel et al., 2016) and overlaps type IIa (low salinity) and type IIb isochore ranges at the lowest P and T conditions. Type III vapour-rich inclusions, trapped a fluid that underwent flash boiling and synchronous to mineralization, were trapped on the liquid-vapour curve, in green (assuming the parental fluid was type IIa). Mineralizing conditions are approximated by the yellow outlined area, < 1 kbar, and between ~150-185 ^{o}C. The black arrow traces the evolution of the fluid and the system from minimum conditions of carbonic-aqueous fluid through to the conditions of mineralization associated with meteoric water incursion (cooling, dilution, redox change) and decompression. Post-mineralization, high salinity type IIb fluids were trapped at lower T.

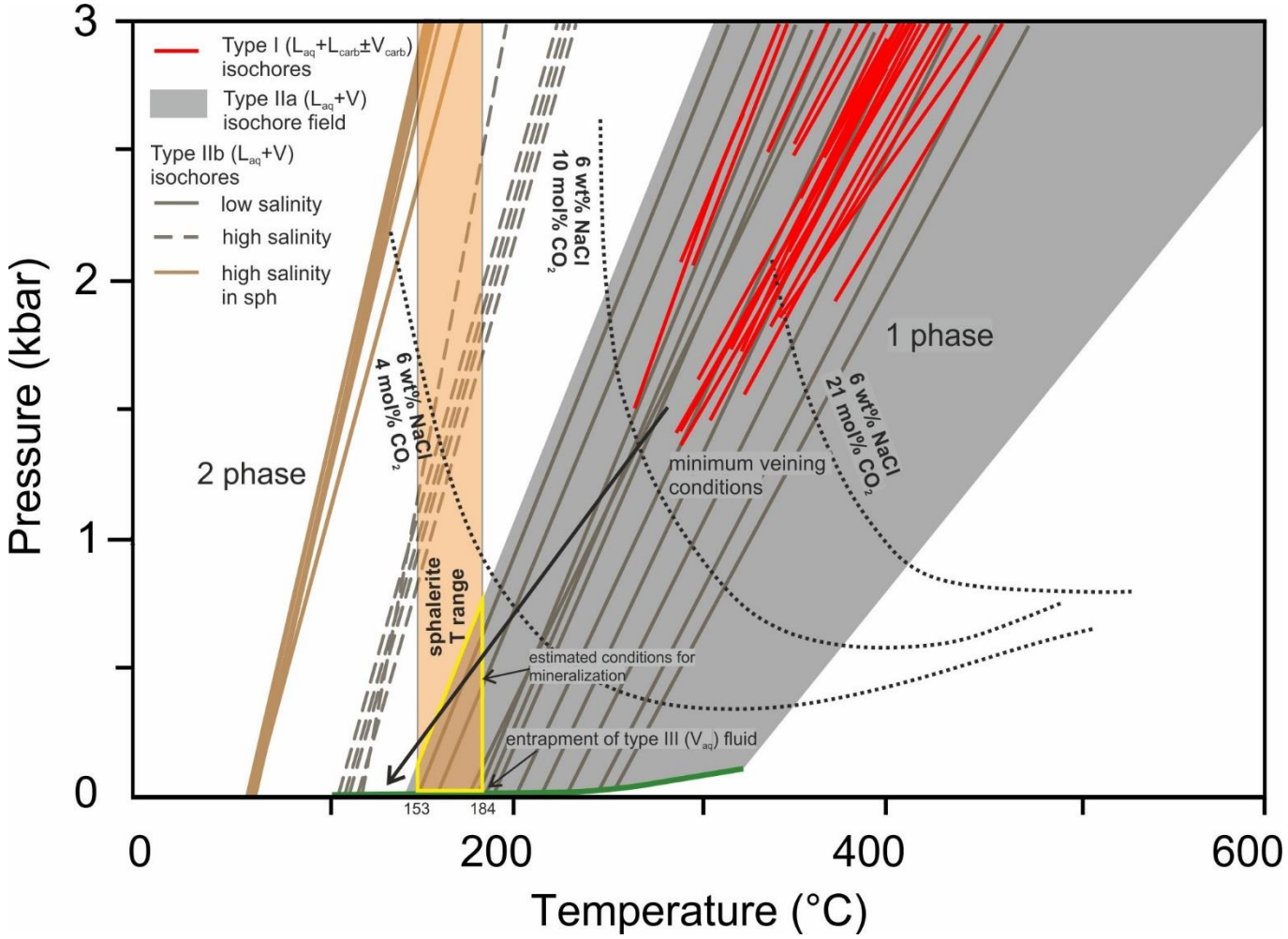
Type I (L_{aq}+L_{carb}±V_{carb}) isochores
Type IIa (L_{aq}+V) isochore field
Type IIb (L_{aq}+V) isochores
low salinity
high salinity
high salinity in sph
6 wt% NaCl 10 mol% CO_2
6 wt% NaCl 4 mol% CO_2
6 wt% NaCl 21 mol% CO_2
2 phase
1 phase
minimum veining conditions
sphalerite T range
estimated conditions for mineralization
entrapment of type III (V_{aq}) fluid
153
184
Pressure (kbar)
Temperature (°C)
0
1
2
3
0
200
400
600

5.4 Fluid and metal origin

The evolution of the hydrothermal system from the earliest type I (carbonic-aqueous) fluid to the type IIa low salinity (aqueous) to type III ("flashing") fluids was associated with a cooling, decompression and dilution trend consistent with an incursion of meteoric water, since type IIa salinities approach 0 wt% $NaCl_{eq}$. Calculated salinities for type IIa inclusions rule out the possibility of sea-water involvement; Precambrian seawater salinities range from 5.4-7 wt% $NaCl_{eq}$. (Knauth, 2004). A probable mechanism that would allow for the system to decompress and introduce meteoric water is faulting, brecciation and possible reactivation of earlier structures (cf. Neumayr et al., 2007; Miklethwaite, 2010), simultaneously creating favourable paths for fluid transport and mineralization precipitation.

Oxygen isotope data illustrates the transition from type I carbonic-aqueous fluid to the type III low-density vapour-rich and provides supporting constraints on the low T origin of the fluid end-member (meteoric water). Figure 4.14 shows measured values (SIMS) of $\delta^{18}O_{V\text{-}SMOW}$ isotope of the two mineralization-related quartz generations (type II, non-luminescing and type III, yellow-luminescing), pre- to syn-mineralization calcite and calcite-adjacent quartz as well as the associated calculated fluid values. Type II quartz $\delta^{18}O_{V\text{-}SMOW}$ values have been separated into two groups according to the spatial association with calcite. With the exception of type III quartz, all the fluid calculations were done using the various temperature constraints. Fractionation equations used were for quartz-H_2O equilibration from Sharp et al. (2016) and for calcite-H_2O equilibration from Horita et al. (2014). The following approaches were used: for type II quartz, distal to calcite-sulfide-filled vugs, two ranges in fluid values were calculated using the maximum

and minimum T_h for type I fluid inclusions combined with the range in measured $\delta^{18}O_{V\text{-}SMOW}$ from type II quartz. For type II quartz, adjacent to calcite-sulfide filled vugs, two ranges are shown, but fluid inclusion T_h values are from type IIb primary, low salinity aqueous inclusions hosted in calcite as these T are considered to be more appropriate minimum conditions for fluid-quartz isotope exchange close to these vugs. In both cases, the calculated fluid value ranges are minimums, as maximum and minimum T_h values used in the calculation represent minimum trapping temperatures of the fluid. For type III quartz, which is genetically linked to sulfides the temperature constraints used for the calculations are considered to be absolute values, based on minimum and maximum temperature from sphalerite thermometry, not fluid inclusion data. Again, two ranges in fluid values are calculated combining the range in measured $\delta^{18}O_{V\text{-}SMOW}$ from type II quartz and the sphalerite min and max T. For calcite fluid values were calculated using the minimum and maximum T_h from type IIb primary, low salinity aqueous inclusions, hosted in calcite. As in the case of quartz calculations, these are also minimum values. This is supported by the apparent overlap of the three estimated ranges, that are the best constraints on the fluid composition at the time of the mineralization, specifically the type III quartz spatially associated with the mineralization, syn-mineralization calcite, and calcite-adjacent quartz. A systematic decrease in a $\delta^{18}O_{V\text{-}SMOW}$ of the fluid is required to transition from the carbonic aqueous fluid to the low density one. Minimum values for a mineralizing fluid range from -8 to 0 ‰, indicating interaction with meteoric water, adding an ^{18}O-depleted fluid (Fekete, 2016). It is evident, that the system is experiencing a systematic and significant decrease in $\delta^{18}O_{V\text{-}SMOW}$ values by the time of the mineralization.

While the proportions of the mixed end-members not are not constrained, values of $\delta^{18}O_{V\text{-}SMOW}$ (< 0) can only be attributed to meteoric water.

With respect to the other end-member fluid in this mixing scenario, low salinity carbonic-aqueous fluids are documented as mineralizing fluids in orogenic gold systems (e.g., Roedder, 1982; McCuaig & Kerrich, 1998; Ridley & Diamond, 2000; Bodnar et al., 2014; Groves and Goldfarb, 2015; Rauchenstein-Martinek et al., 2014, 2016;Fusswinkel et al., 2017), as well as deep porphyry deposits (Rusk et al., 2008; Reed at al., 2020), intrusion-related gold systems (Lang and Baker, 2001; Marsh et al., 2003; Mair et al., 2006), and pegmatites (Thomas and Spooner, 1992). Additionally, such fluids are commonly associated with regional metamorphism (greenschist to amphibolite grade or higher). The latter is important, considering that the Nonacho Basin sediments were metamorphosed to greenschist facies (Aspler, 1985). Alternatively, the former may also be considered magmatic sources for carbonic-aqueous fluids and some ore metals could be the proximal mafic calc-alkalic Sparrow Dykes and/or felsic Thekulthili stock (Bostock & Breeman, 1992, 1994).

With respect to S source (e.g., Cu, Ag), stable S isotope data for chalcopyrite from Salkeld Lake is compared to other copper deposits globally in Figure 5.4. This diagram shows the ranges for $\delta^{34}S_{V\text{-}CDT}$ in chalcopyrite for different deposit types including the hydrothermal Cu veins of the Messina deposit (Sawkins & Rye, 1978), a nearby MVT deposit, (Pine Point, NWT, Canada; Sasaki & Krouse, 1969); two stratiform copper deposits: Redstone stratiform copper deposit, NWT, Canada (Milton, 2015), and the Kupferschiefer copper deposit, Germany (Wagner, 2010). Notably, the very negative values of $\delta^{34}S_{V\text{-}CDT}$ for Salkeld Lake are close to that for chalcopyrite from the

Kupferschiefer sediment-hosted copper deposit, attributed to the leaching of sulfides from sediments, with those sulfides formed by bacterial reduction of marine sulfate, (sedimentary-diagenetic source; Asael, 2009; Wagner, 2009). Taking this into consideration, the dissolution of older sedimentary sulfides by the mineralizing fluids during fluid rock interaction in the Nonacho Basin may explain the data from Salkeld Lake. Recent SIMS analyses of diagenetic pyrite from marine metasandstone-mudstone at the Tronka Chua-Chief Nataway transition yielded $\delta^{34}S_{V\text{-}CDT}$ values between -12.3 and 2.0 ‰ (J. Hanley, communication, December 2021). These data indicate that ^{34}S depleted sedimentary S sources occur within the host formations for the Salkeld Lake occurrence.

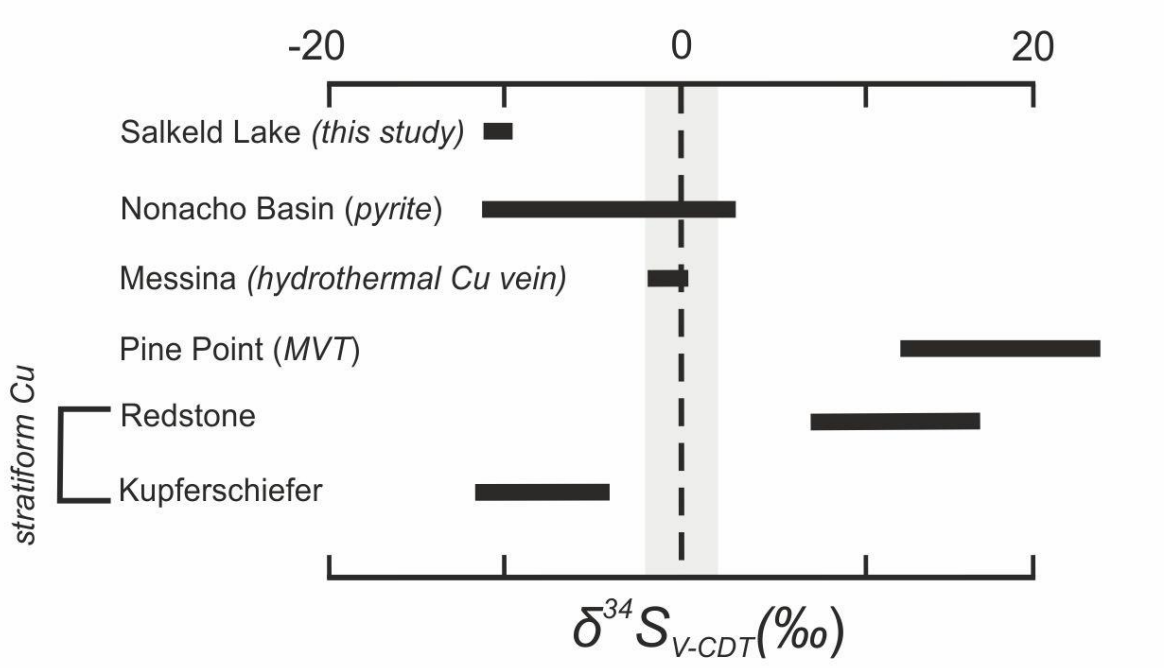

Figure 5.4: Sulfur isotope diagram ($\delta^{34}S_{V\text{-}CDT}$), showcasing compositional ranges for chalcopyrite from various copper-lead-zinc sulfide deposit styles, plotted with the isotope data from Salkeld Lake chalcopyrite. Deposits for comparison from top down: the Messina hydrothermal copper deposit, South Africa (Sawkins & Rye, 1978), Pine Point MVT, NWT, Canada (Sasaki & Krouse, 1969), Redstone stratiform copper, NWT, Canada (Milton, 2015), Kupferschiefer copper deposit, Germany (Wagner, 2010), and pyrite from Tronka Chua and Chief Nataway Formations, Nonacho Basin (J. Hanley, communication, December 2021). Mantle $\delta^{34}S_{V\text{-}CDT}$ values from Chaussidon et al., 1989.

5.5 Geochronology

The results of the Re-Os age dating of molybdenite and Ar-Ar dating of muscovites and biotite introduces a major uncertainty with respect to the timing of the Salkeld Lake mineralization. Molybdenite, often appearing as inclusions in sulfides and muscovite, is dated at 1884 ± 8 Ma, considerably older than the pre- to syn-mineralization muscovite, dated at 1831 ± 2 Ma (weighted mean, n=58). The muscovite ages overlap with the calc-alkalic magmatism in the Nonacho Basin (Figure 5.5), specifically Jerome Lake (Sparrow) calc-alkalic mafic dykes (1827 ± 4 Ma; Bostock and Breeman, 1992, 1994). The age of one muscovite sample (SAL-4E) overlaps with the age of Thekulthili granite dated at 1813 ± 4 Ma (Bostock and Breeman, 1992, 1994). However, this is due to a large error range, thus making Thekulthili granite an unlikely heat source for hydrothermal activity. The mean ages for muscovite are consistent from sample to sample, except for the aforementioned sample, and do not show significant variation with grain size (Figure 4.13), suggesting growth of the large grains (all > 100 μm) below the closure temperatures (~350-425 ^{o}C; Harrison et al., 2009; Oriolo et al., 2016). The T of the veining stage I event at the onset of the mineralization must be at or below the closure temperature, consistent with the microthermometric results for the early carbonic-aqueous fluid (Figure 4.10). Wallrock biotite (weighted mean 1826 ± 5 Ma) gives younger ages than muscovites, although not significantly; this can be attributed to the lower closure temperature of biotite (310 ± 40 ^{o}C; Harrison et al., 1985, 2009), and resetting by the type I quartz veining event

Both mineralizing events [Mo and Cu-Ag-(Pb-Zn)] overlap with major orogenic events occurring in the Western Rae (ca. 2.0-1.8 Ga), timed with the Trans-Hudson Orogeny (Godet et al., 2020). Figure 22 shows the absolute ages of the Thelon-Taltson

(2.0-1.9 Ga; Card et al., 2014), Wopmay (1.95-1.84 Ga; Davis et al., 2015; 2018) and Snowbird Orogen (1.94-1.86 Ga; Flowers et al., 2006) orogenies. As well, age windows for distal alkalic and calc-alkalic magmatism occurring in the Churchill and Slave Provinces are also shown in Figure 5.5; these include the Butte Island intrusives at ~1895 Ma, the Blatchford Lake intrusives at ~1892 Ma and the Compton calc-alkalic suite at 1872 Ma, located around the East arm of the east Slave Lake (Bowring et al., 1984; Mumford & Cousens, 2014), Martin Group basalts (~1818 Ma, Morelli, 2009; D'Souza, 2012) and the Christopher Island formation (~1830 Ma, Cousens et al., 2001). Those magmatic events in the Slave Province/ East arm clearly overlap with the Re-Os ages (~1884 Ma) of vein molybdenite at Salkeld. Distal alkaline magmatic events (Christopher Island, Martin Group basalts) may have been broadly regional heat sources relevant to the Cu mineralization. However, the most relevant proximal magmatic event is the emplacement of the Sparrow (Jerome Lake) mafic dykes (1827 ± 4 Ma), with their age overlapping with that of muscovite ages (~1831 ± 2 Ma). Those dykes may be a surface expression of what could be a much larger intrusive body under the study area, yet unidentified. The nature of the earlier molybdenite mineralizing event is unknown

It could be that the muscovite K-Ar clock was reset by the Sparrow Dykes (~1827 Ma) or Thekulthili stock (~1814 Ma), and that the age of the Cu-Ag-(Pb-Zn) mineralization is the same as that of molybdenite at ~1884 ± 8 Ma (the textural relationship between muscovite and molybdenite is discussed in section 5.2). However, it likely that the muscovites from an earlier event have not been re-set. The presence of intact carbonic-aqueous inclusions, which during microthermometric heating in the lab setting decrepitated above ~300 ^{o}C (i.e., below muscovite closure temperature), is key to this

argument. The Salkeld system cooled and decompressed to near surface conditions during mineraliztion, transitioning from type II quartz through to type III. Any reheating to a T sufficient enough to reset the muscovite K-Ar clock would have caused carbonic-aqueous inclusions to widely decrepitate, and they would not be preserved today. Likewise, any later reheating post-mineralization would have the same impact. Therefore, it is highly unlikely that the muscovite ages were reset by either the Sparrow Dykes (~1827 Ma) or Thekulthili stock (~1814 Ma) emplacements; their thermal influence was not enough to increase the T above the muscovite closure.

Having considered the geochronology results, it can be speculated that the overlap in ages between the intrusive rocks in the Nonacho Basin and the muscovite at Salkeld Lake implicates the calc-alkaline mafic Sparrow dykes as a possible heat source driving hydrothermal activity and possibly a source for some ore metals (e.g., Cu, Ag). The extent and size of the Sparrow dyke-related event cannot be assessed due to the lack of data on the magmatic history of the basin. Nonetheless, it can be assumed with a certain degree of confidence, that the heat source has to be quite significant in size to allow for such long cooling windows, as to allow resetting of wall rock biotite as late as 1814 ± 3 Ma.

Figure 5.5 (following page): Geochronological constraints on Cu-Ag-(Pb-Zn) mineralization at Salkeld Lake based on laser Ar-Ar age dating of vein muscovite and wall-rock biotite, and Re-Os age dating of vein molybdenite, shown on an absolute timescale compared to potentially relevant distal and proximal basinal, magmatic and tectonic events. The age data for Salkeld Lake mineralization are summarized in Table 7. Muscovite and biotite data are shown here as bars corresponding to weighted mean values including uncertainty for each sample (3 biotite and 5 muscovite samples; multiple grains measured per sample). Weighted mean ages for the three biotite samples are listed. The weighted mean age for each muscovite sample are not listed, but the weighted mean age for all muscovite grains combined is listed in the box. Figure shows distal and proximal magmatic events: 1 = Nuna volcanism (Hartnady et al., 2019); 2 = Thekulthili stock (Bostock, 1994); 3 = Martin Group basalts (Morelli, 2009; D'Souza, 2012); 4 = Jerome Lake (Sparrow) dyke (Bostock & Breeman, 1992); 5 = Christopher Island formation (Cousens et al., 2001); 6 = Compton calc-alkalic suite (Bowring et al., 1984; Mumford & Cousens, 2014); 7 = Blatchford Lake intrusives (Mumford & Cousens, 2014) 8 = Butte Island intrusives (Bowring et al., 1984; Mumford & Cousens, 2014). The major orogenic and basinal events included are the Trans-Hudson Orogen (Godet et al., 2020); Snowbird Orogen (Flowers et al., 2006); Wopmay Orogen (Davis et al., 2015; 2018); Thelon-Taltson Orogen (Card et al., 2014) and the available constraints for the Nonacho Basin (Neil, 2021).

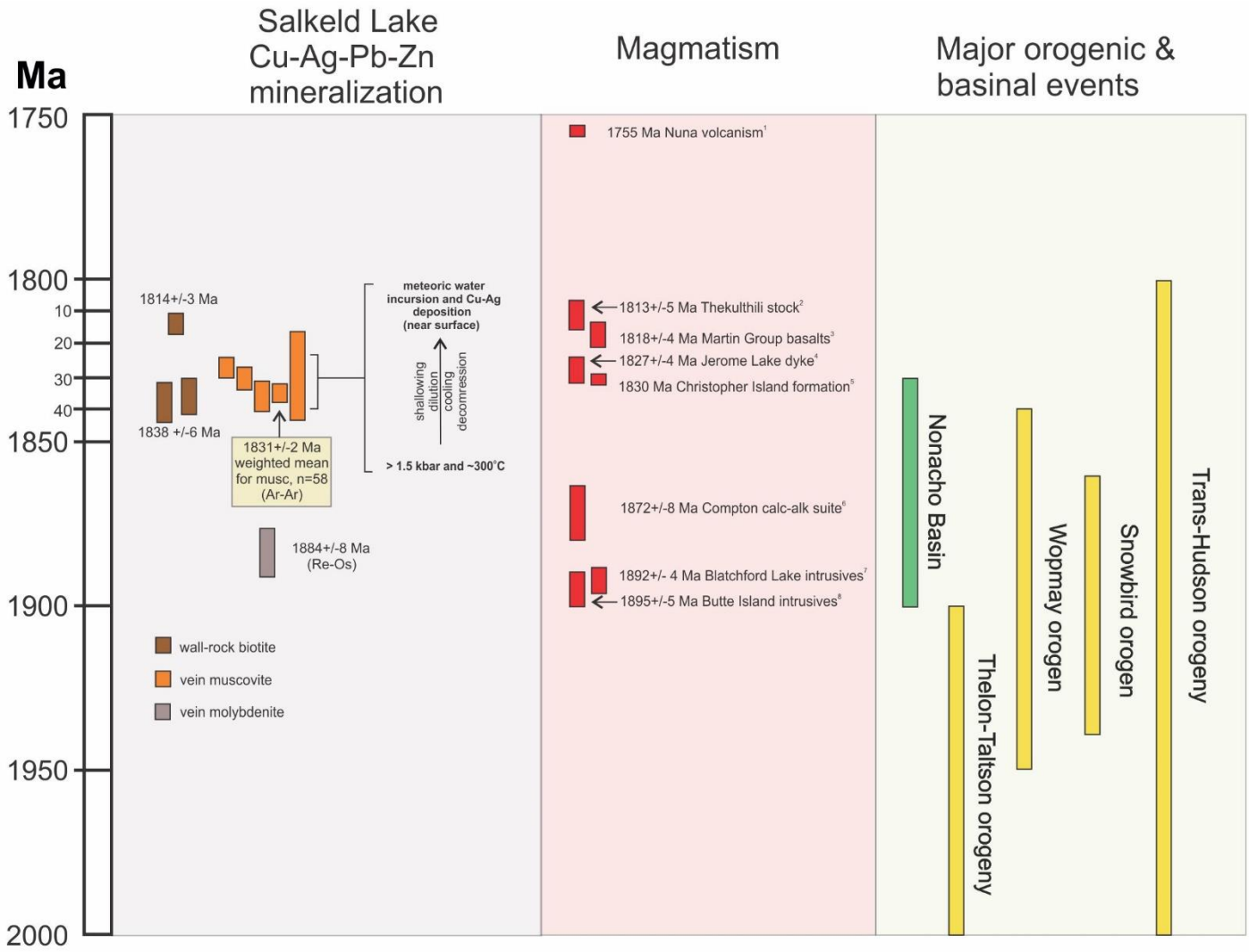
Ma
Salkeld Lake Cu-Ag-Pb-Zn mineralization
Magmatism
Major orogenic & basinal events
1750
1800
10
20
30
40
1850
1900
1950
2000
1814+/-3 Ma
1838 +/-6 Ma
1831+/-2 Ma weighted mean for musc, n=58 (Ar-Ar)
1884+/-8 Ma (Re-Os)
meteoric water incursion and Cu-Ag deposition (near surface)
shallowing
dilution
cooling
decompression
> 1.5 kbar and ~300°C
wall-rock biotite
vein muscovite
vein molybdenite
1755 Ma Nuna volcanism[1]
1813+/-5 Ma Thekulthili stock[2]
1818+/-4 Ma Martin Group basalts[3]
1827+/-4 Ma Jerome Lake dyke[4]
1830 Ma Christopher Island formation[5]
1872+/-8 Ma Compton calc-alk suite[6]
1892+/- 4 Ma Blatchford Lake intrusives[7]
1895+/-5 Ma Butte Island intrusives[8]
Nonacho Basin
Thelon-Taltson orogeny
Wopmay orogen
Snowbird orogen
Trans-Hudson orogeny

5.6 Classification and deposit comparison

Copper and other economically important metals (Ag, Pb, Zn) occur together within a variety of classified mineral deposit styles. Most of the planets giant copper deposits are porphyry deposits, (e.g. Chuquicamata, Escondida and El Salvador in Chile, Toquepala in Peru, and Malanjkhand, India, Stein et al., 2004; Romero et al., 2011; Zentilli, 2017) and sediment-hosted copper deposits, (e.g. Central African Copperbelt in Zambia and the Democratic Republic of Congo: Cailteux et al., 2005; Muchez et al., 2015; Crundwell et al., 2020; Kupferschiefer district in Poland and Germany: Mikulski et al., 2019; Oszczepalski et al., 2019). Additionally, Cu is mined in particular from VMS, SEDEX, volcanic red-bed, IOCG and other polymetallic deposit types. The strategic value of Cu is a critical incentive to study and classify unknown Cu deposits in Canada and globally, to refine genetic models for various deposit-styles to aid in exploration efforts.

The Salkeld Lake Cu-Ag-(Pb-Zn) mineralization shows mineralogical, geochemical, fluid and isotope characteristics that are both similar and dissimilar to many different Cu deposit styles, such as sediment-hosted copper and intrusion-related varieties.

The mineralogy, characterized by the presence of two distinct paragenetic sequences and dominated by chalcopyrite, bornite, chalcocite, sphalerite and galena, is consistent with sediment-hosted copper style mineralization (Kupferschiefer-type, sedimentary red-bed and volcanic red-bed type deposits). The presence of the minerals like idaite and yarrowite, common in low-temperature, shallow sediment-hosted deposits also mineralogically resembles sediment-hosted Stavelot Massif in Belgium (Hatert, 2005). The presence of molybdenite may be consistent with the porphyry-style, intrusion-related deposits, such as the giant Cu–Mo–Au Bingham Canyon deposit (e.g., Grondahl

& Zajacz, 2017). However, the results of Ar-Ar and Re-Os age dating shows that molybdenite is earlier than the main stage Cu-Fe-sulfide mineralization by ~50 Ma.

The alteration assemblage consisting of muscovite-epidote-adularia is unusual, but broadly consistent with phyllic (muscovite) and propylitic (epidote, adularia) alteration assemblages formed at relatively high pH values and moderate T, those that often occur in the outer zones of Cu-Au-Mo porphyry-epithermal systems and mesothermal Au deposits (Corbett, 2014).

The bulk geochemical characteristics of the mineralization using bulk-rock data for the selected elements (Ag, As, Au, Cd, Cu, In, Mo, Ni, Pb, Zn, U Ba, Ga, Se, Sn, Te, Bi, Co) for comparison (Figure 5.6) shows the data for Great Slave polymetallic system (Burke, 2018), Redstone stratiform copper (Milton, 2015), NICO IOCG (Golder Associates Ltd, 2011), Sunrise VMS (Sanche, 2001) and uranium deposits within the Nonacho Basin, specifically Kult-82, Dussault and Island showings (Landry, 2021) plotted over the Salkeld Lake data. It is evident that Salkeld Lake bears the closest geochemical resemblance to the Redstone copper deposit: note considerably low values of Au, In, Te, Bi and slightly elevated Cd, Ba and Mo. The major difference between Salkeld Lake and the Redstone Copperbelt is the elevated content of Pb and Zn at Salkeld. Nonetheless, it can be surmised that geochemically Salkeld Lake deposit carries metal associations of sediment-hosted style mineralization.

The sulfur isotope data shown in Figure 5.4, shows values of $\delta^{34}S_{V\text{-}CDT}$ from a variety of Cu deposits. Salkeld Lake shows low values (mean $\delta^{34}S_{V\text{-}CDT}$ = -15 ‰), not unlike sediment-hosted Kupferschiefer deposit both attributed to the bacterial reduction of sulfates, derived from the sedimentary-diagenetic or marine sources. Diagenetic pyrite

from marine sandstone-mudstone from the Nonacho metasedimentary units (Tronka Chua and Chief Nataway Formations) yielded between $\delta^{34}S_{V\text{-}CDT}$ -12.3 and 2.0 ‰, indicating that ^{34}S depleted sedimentary S sources occur within the host formations for Salkeld.

However, despite some similarities in host rock, setting, mineralogy and S isotope systematics, Salkeld Lake mineralization is vein and breccia hosted, and therefore uncharacteristic of SSC deposits, in which mineralization is stratiform/stratabound.

The Messina hydrothermal vein- and breccia pipe-hosted copper deposit in South Africa shares many similar genetic features with Salkeld Lake, despite having higher $\delta^{34}S_{V\text{-}CDT}$ sulfide values (~ -3-0 ‰). In the Messina deposits, Cu sulfides occur mainly in breccia pipes and veins, hosted by granulite-facies metasedimentary rocks. The mineralogy is dominated by chalcopyrite, bornite and chalcocite and, similar to Salkeld Lake, does not have abundant pyrite. Fluid inclusion studies in quartz and calcite in the Messina deposit indicate that Cu deposition occurred at ~160 ^{o}C, with a decrease in temperature and salinity, from ~25 to 2 wt% $NaCl_{eq}$. with time (Sawkins, 1977). This is reminiscent of Salkeld Lake, as the T for mineralization is constrained between 150 and 180 ^{o}C and the system had similar cooling and dilution history (Figures 4.12, 5.3). However, early-stage fluid salinity at Messina was significantly higher. The fluids responsible for the mineralization at Messina were constrained to be a mixture of magmatic-hydrothermal fluids related to peralkalic magmatism and low temperature meteoric water. The hydrothermal system at Messina evolved to produce mineral zonation through gradual cooling and reaction with the host rocks with fluids, entering the

system through wide-scale open structures in brecciated metasediments (Jacobsen & McCarthy, 1976; Sawkins & Rye, 1977, 1978).

A similar comparison can be made with the Mesoproterozoic Cu deposit at Mamainse Point, Ontario, Canada (Richards & Spooner, 1989), hosted in mafic metavolcanic rocks, with sulfides occurring in fault-related quartz veins. The paragenetic sequence of pyrite→ chalcopyrite→bornite→chalcocite→hematite, followed by late-stage deposition of calcite and associated with propylitic alteration at Mamainse Point indicates an increase in fO_2 and pH, similar to the interpretation of the sulfide paragenesis and related fluid evolution at Salkeld Lake (except for the lack of pyrite). Fluid inclusion data from Mamainse Point is consistent with mixing between hot, saline fluid of magmatic origin and cooler meteoric water (Richards & Spooner, 1989). The combined effects of cooling, dilution, neutralization, and oxidation are thought to have produced a significant drop in Cu solubility. Stable isotope data also supports a model involving meteoric water interacting with magmatic fluid at Mamainse Point (Keays et al., 2015; Perello et al., 2020), similar to Salkeld Lake.

Despite similarities to both SSC and some other vein and breccia-hosted magmatic-hydrothermal Cu deposits (i.e., Messina, Mamainse Point), the presence of Pb and Zn complicates the classification of the Salkeld Lake mineralization style. These metals are not commonly associated with magmatic fluids, but rather with basinal brines, akin to those in MVT systems (Kesler et al., 1995, 2007). Texturally, Pb and Zn are coeval with major Cu-Fe sulfides at Salkeld Lake and are major elements in some samples, but notably are only present in the surface samples. These metals may have been remobilized from the sediments of the Nonacho Group (similar to the source of sulfur,

supported by S isotopes). The system did experience an influx of late, basinal brine-like (Richard et al., 2010), high salinity fluid, recorded as secondary type IIb inclusions in sphalerite, but this firmly places this fluid timing as post-sphalerite mineralization, so unrelated to Pb-Zn. On the other hand, some intrusion-related base metal deposits (e.g., San Rafael, Peru; Harlaux et al., 2021; Bingham, Utah, Tomlinson et al., 2021) have high grade polymetallic Pb-Zn-Cu-Ag-Au veins associated with them.

Overall, the Salkeld Lake Cu-Ag-(Pb-Zn) mineralization exhibits some traits of both a sediment-hosted copper deposit but its distinct vein and breccia-hosted nature, stable isotope and fluid inclusion systematics, and sulfide mineralogy suggest a distinct magmatic, possibly intrusion-related affinity with meteoric water involvement. The deposit could be referred to as a “hybrid-type” mineralization style, with a high temperature, magmatic-hydrothermal component, not unlike that at the Messina copper deposit in South Africa (Sawkins & Rye, 1978) or a similar deposit at Mamainse Point, Ontario (Richards & Spooner, 1989).

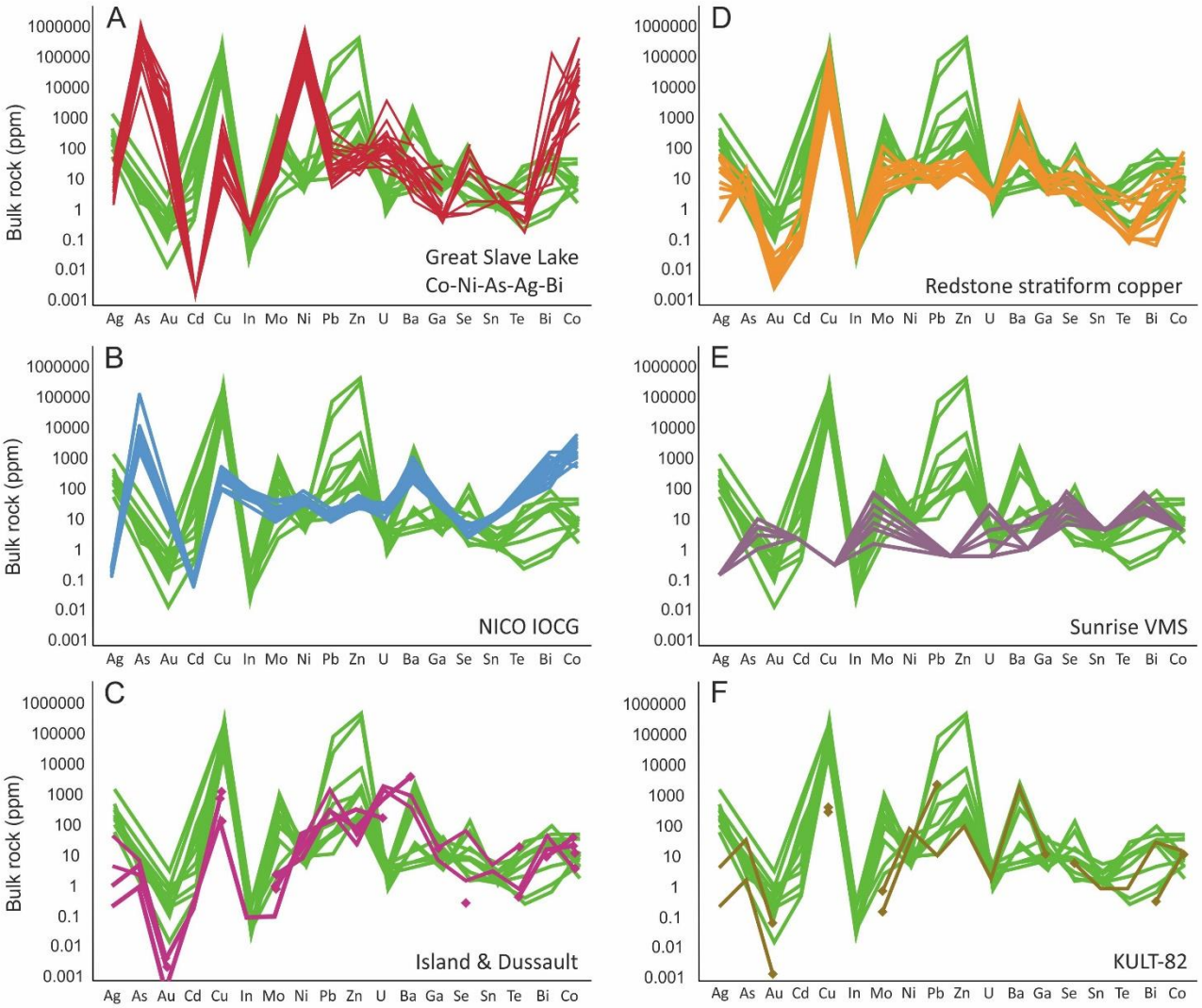

Figure 5.6: Non-normalized spider-plots showing the concentration (ppm) of selected elements. Salkeld Lake bulk-rock data is plotted against and compared to the data from: **A.** East Arm polymetallic veins, NWT (Burke, 2018). **B.** NICO IOCG system, NWT (Golder Associates Ltd, 2011). **C.** Data from the assays of the uranium showings around Nonacho Basin Island and Dussault (Landry, pers. comm, 2021) **D.** Redstone Copperbelt, NWT, (Milton, 2015). **E.** Sunrise Lake VMS system, NWT (Sanche, 2001). **F.** Data from the assays of the uranium showings around Nonacho Basin – Kult-82 (Landry,

pers. comm, 2021). Salkeld Lake is characterized by high concentrations of copper, lead and zinc, as well as barium, and low concentrations of gold, uranium and indium. Note the geochemical signature of Salkeld Lake closely resembling that of the Redstone Copperbelt stratiform copper deposit.

Chapter 6: Conclusions and future work

6.1 Key conclusions

At Salkeld Lake, Nonacho Basin, NWT, vein-hosted Cu-Ag-(Pb-Zn) mineralization post-dates three main host rock lithologies. Host granitic gneisses, meta-sediments and alkali red granitoids are overprinted by disseminations, fracture vug infills in quartz veins, and quartz-sulfide breccias within the *stockwork* and *shear-hosted* zones. Sulfide mineralization is dominated by Ag-rich chalcopyrite, Ag-rich bornite, chalcocite Cd-rich sphalerite and galena. The system shows mineralogical zonation, with two distinct paragenetic sequences in the surface (original mineralizing centre) and core (original periphery) samples (cpy→bn→cc→cv vs cv→cc→bn→cpy). A distinct alteration mineralogy is observed consisting of muscovite-epidote at surface and muscovite-epidote-adularia, identified as calc-phyllic or calc-propylitic, and syn-sulfide calcite in core. These differences are partly attributed to fluctuating pH but must have also been influenced by fluctuating oxygen fugacity (fO_2). Carbonic-aqueous type I fluids, associated with the veining stage, represent the onset of vein formation hosting the mineralization, and had a minimum T and P of trapping of ~300 ^{o}C and ~1.5 kbar, trapped in the single-phase field of the NaCl-CO_2-H_2O system. The system experienced dilution and cooling through the incursion of meteoric water to produce type IIa, low salinity fluids. Shallowing and decompression at the time of sulfide deposition, led to entrapment of coeval type III vapour-rich inclusions, containing low-density aqueous vapour formed by boiling. The minimum T and P constraints for the mineralization are ~150-180 ^{o}C and <750 bar, based on the several overlapping constraints, including sphalerite thermometry and microthermometric results for the syn-mineralization type IIb low-salinity fluid. The

system must have experienced a later influx of highly saline colder fluid (post-sulfide) to yield type IIb high salinity fluids found as secondary trails of fluid inclusions in calcite and sphalerite. The origin of this later fluid is unknown but may be basinal/seawater/evaporite-related. The O isotope data show gradual depletion of $\delta^{18}O_{V\text{-}SMOW}$ with time towards meteoric water composition. The mineralization is dated at ~1831 ± 2 Ma, timed with proximal igneous activity in the Nonacho Basin, specifically, the Sparrow dyke swarm dated at 1827 ± 4 Ma at Jerome Lake. The Sparrow dykes are only surface manifestations of what could be a much larger igneous heat source that drove the hydrothermal fluid circulation, and possibly acted as a metal source for Cu-Ag, whereas Pb-Zn and S are likely metasediment-derived via fluid and host rock interaction.

Molybdenite mineralization, pre-dating (1884 ± 8 Ma) the main Cu-Ag-(Pb-Zn) sulfide mineralization may be an early intrusion-related mineralization related to the distal magmatic processes occurring in the Western Churchill Province (ca. Trans-Hudson Orogeny), specifically, the Snowbird Orogeny at 1.94-1.86 Ga. There are no other data available to provide further constraints on this early molybdenite mineralization.

Considering the mineralogical, geochemical, fluid and stable isotope evidence, the Salkeld Lake Cu-Ag-(Pb-Zn) deposit is classified as a “hybrid” deposit with characteristics of both a sediment-hosted copper deposit, and magmatic-hydrothermal heat vein breccia pipe-type Cu deposits. It formed at ~1831 Ma, overprinting an earlier molybdenite mineralization at ~1884 Ma.

6.2 Implications for mineral exploration and future work

Additional work is encouraged to improve the classification, and understanding of formation conditions, of this possibly unique “hybrid-type” deposit, with characteristics

mixed between intrusion-related and volcanosediment-hosted stratiform Cu. The size and zonation of the deposit should be assessed, specifically to further spatially constrain the center and periphery of the mineralized system. Constraints on fluid provenance, metal and heat sources, the chemical processes affecting ore deposition (i.e., reducing agents) for the development of the overall paragenetic model can be improved upon. Further petrographic and fluid inclusion studies can help identify the source for the late-stage influx of highly saline, cooler fluids. Metal contents and trace elements in fluid inclusions should be determined by LA-ICP-MS to confirm a possible magmatic input and reveal the chemical nature of the fluid. To better constrain fluid and metal origin, further investigation into the magmatic history of the Nonacho Basin is required to gain a better understanding of the possible heat (and metal) sources. Geochemical analysis of young intrusive suites in the basin, as well as age dating for those units are needed. Additionally, the relationship to Nonacho Basin U mineralization, evidently not present at Salkeld, is ambiguous. It remains unclear whether Cu and U mineralization are temporally related and share common heat and/or fluid sources.

References

Alexandre, P. (2012). Modeling of the fluid flow involved in the formation of Athabasca basin unconformity-type uranium deposits. Geological Association of Canada. In *Mineralogical Association of Canada Annual Conference Abstracts, 35*.

Alexandre, P., Jiricka, D. (2009). Critical geochemical and mineralogical factors for the formation of unconformity-related uranium deposits: comparison between barren and mineralized systems in the Athabasca Basin, Canada. *Economic Geology, 104*. 413-435.

Alexandre, P., Kyser, K., Polito, P., Thomas, D. (2005). Alteration mineralogy and stable isotope geochemistry of Paleoproterozoic basement-hosted unconformity-type uranium deposits in the Athabasca Basin, Canada. *Economic Geology, 100*, 1547-1563.

Allen, P. A., & Armitage, J. J. (2012). Cratonic Basins. In *Tectonics of Sedimentary Basins* (pp. 602-620). https://doi.org/10.1002/9781444347166.ch30

Allen, P. A., Eriksson, P. G., Alkmim, F. F., Betts, P. G., Catuneanu, O., Mazumder, R., Meng, Q., & Young, G. M. (2015). Chapter 2 Classification of basins, with special reference to Proterozoic examples. *Geological Society, London, Memoirs*, *43*(1), 5-28. https://doi.org/10.1144/m43.2

Asael, D., Matthews, A., Oszczepalski, S., Bar-Matthews, M., Halicz, L. (2009). Fluid speciation controls of low temperature copper isotope fractionation applied to the Kupferschiefer and Timna ore deposits. *Chemical Geology*, *262*(3-4), 147-158. https://doi.org/10.1016/j.chemgeo.2009.01.015

Ashton, K. E., Hartlaub, R. P., Heaman, L. M., Morelli, R. M., Card, C. D., Bethune, K., & Hunter, R. C. (2009). Post-Taltson sedimentary and intrusive history of the southern Rae Province along the northern margin of the Athabasca Basin, Western Canadian Shield. *Precambrian Research*, *175*(1-4), 16-34. https://doi.org/10.1016/j.precamres.2009.09.004

Aspler B. L., 1985. Geology of Nonacho Basin (Early Proterozoic) NWT. Ph.D. thesis, Carleton University, Ontario.

Bakker, R. J. (2003). Package FLUIDS 1. Computer programs for analysis of fluid inclusion data and for modelling bulk fluid properties. *Chemical Geology, 194*, 3-23.

Bakker, R. J., Brown, P. E. (2003). Computer modelling in fluid inclusion research. In: Fluid Inclusions, Analysis and Interpretation (eds. Samson I, Anderson A, Marshall D), *Short Course v. 32, Mineralogical Association of Canada*, 175-212.

Bakker, R. J., Diamond, L. W. (1999). Determination of the composition and molar volume of H2O-CO2 fluid inclusions by microthermometry. *Geochimica et Cosmochimica Acta 64-10*, 1753–1764.

Bath, A. B., Cooke, D. R., Friedman, R. M., Faure, K., Kamenetsky, V. S., Tosdal, R. M., Berry, R. F. (2014). Mineralization, U-Pb geochronology, and stable isotope geochemistry of the lower main zone of the Lorraine Deposit, north-central British Columbia; a replacement-style alkalic Cu-Au porphyry. *Economic geology and the bulletin of the Society of Economic Geologists, 109(4)*, 979-1004.

Beaudoin, G., Therrien, P. (2004). The Web Stable Isotope Fractionation Calculator. In *Handbook of Stable Isotope Analytical Techniques*, 1045-1047. https://doi.org/10.1016/b978-044451114-0/50051-x

Bell, R. T. (1996). Sandstone uranium. In *Geology of Canadian Mineral Deposit Types, 8,* 212-219.

Berman, R. G., Pehrsson, S., Davis, W. J., Ryan, J. J., Qui, H., & Ashton, K. E. (2013). The Arrowsmith orogeny: Geochronological and thermobarometric constraints on its extent and tectonic setting in the Rae craton, with implications for pre-Nuna supercontinent reconstruction. *Precambrian Research*, *232*, 44-69. https://doi.org/10.1016/j.precamres.2012.10.015

Berman, R. G., Davis, W. J., Pehrsson, S. (2007). Collisional Snowbird tectonic zone resurrected: Growth of Laurentia during the 1.9 Ga accretionary phase of the Hudsonian orogeny. *Geology, 35,* 911-914.

Bodnar, R. J., Moncada, D., Baker, D. (2017). Mineralogical, petrographic and fluid inclusion evidence for the link between boiling and epithermal Ag-Au mineralization in the La Luz area, Guanajuato Mining District, México. *Ore Geology Reviews 89(35)*, 143-170.

Bodnar, R. J., Lecumberri-Sanchez P., Moncada D. and Steele-MacInnis M. (2014). Fluid inclusions in hydrothermal ore deposits. In Reference Module in Earth Systems and Environmental Sciences Treatise on Geochemistry (Second Edition), pp. 119–142.

Bodnar, R. J., Lecumberri-Sanchez, L., Moncada, D., Steele-MacInnis, M. (2014). 13.5–Fluid inclusions in hydrothermal ore deposits. *Treatise on geochemistry.* 2nd edn. Elsevier, Oxford 119, 142-267.

Bostock, H. H., van Breeman, O. (1994). Ages of detrital and metamorphic zircons and monazites from a pre-Taltson magmatic zone basin at the western margin of Rae Province. *Canadian Journal of Earth Sciences, 31*, 1353-1364.

Bostock, H. H., van Breeman, O. (1992). The timing of emplacement, and distribution of the Sparrow diabase dyke swarm, District of Mackenzie, Northwest Territories. Radiogenic Age and Isotopic Studies: Report 6. *Geological Survey of Canada, 92-2*, 49-55, https://doi.org/10.4095/134164 (Open Access).

Bowring, S. A., Schmus, W. R., Van Hoffman, P. F. (1984). U-Pb zircon ages from Athapuscow aulacogen, East Arm of Great Slave Lake, N.W.T., Canada. *Canadian journal of earth sciences, 21(11)*, 1315-1324.

Brown, A. C. (1997). World-class sediment-hosted stratiform copper deposits: Characteristics, genetic concepts and metallotects. *Australian Journal of Earth Sciences, 44(3)*, 317-328. DOI: 10.1080/08120099708728315

Buchanan, L. J., (1981). Precious metal deposits associated with volcanic environments in the southwest. *Arizona Geological Society Digest. 14*, 237-262.

Burgess, P. M. (2019). Phanerozoic Evolution of the Sedimentary Cover of the North American Craton. In *The Sedimentary Basins of the United States and Canada*, 39-75. https://doi.org/10.1016/b978-0-444-63895-3.00002-4

Cabral, A. R., Beaudoin, G. (2007). Volcanic red-bed copper mineralisation related to submarine basalt alteration, Mont Alexandre, Quebec Appalachians, Canada. *Mineralium Deposita, 42(8)*, 901-912. https://doi.org/10.1007/s00126-007-0141-7

Cailteux, J. L. H., Kampunzu, A. B., Lerouge, C., Kaputo, A. K., & Milesi, J. P. (2005). Genesis of sediment-hosted stratiform copper–cobalt deposits, central African Copperbelt. *Journal of African Earth Sciences*, *42*(1-5), 134-158. https://doi.org/10.1016/j.jafrearsci.2005.08.001

Card, C. D., Bethune, K. M, Davis, W. J., Rayner, N., Ashton, K. E. (2014). The case for a distinct Taltson orogeny: Evidence from northwest Saskatchewan, Canada. *Precambrian research, 255,* 245-265.

Chaussidon, M., Albarede, F., Sheppard, S. M. F. (1989). Sulphur isotope variations in the mantle from ion microprobe analyses of micro-sulphide inclusions. *Earth and Planetary Science Letters*, *92-2*, 144-156. https://doi.org/10.1016/0012-821X(89)90042-3.

Cheng, Y., Shaoyi, W., Tianfu, Z., Xueming, T., Cong, A., Ruoshi, J., Hongliang, L. (2020). Regional sandstone-type uranium mineralization rooted in Oligo- Miocene tectonic inversion in the Songliao Basin, NE China. *Gondwana Research, 88,* 88-105. https://doi.org/10.1016/j.gr.2020.08.002

Chi, G., Lu, H. (2008). Validation and representation of fluid inclusion microthermometric data using the fluid inclusion assemblage (FIA) concept. *Acta Petrologica Sinica 24-9*,1945-1953.

Christopher A. (1993). Report on the 1993 exploration program on the Salkeld Lake property, Teck Exploration Ltd, North Bay, Ontario.

Cloutier, J., Olivo, G., Alexandre, P. (2008). The Millenium uranium deposit, Athabasca Basin, Saskatchawan, Canada: insights into an atypical basement-hosted uranium deposit. Conference: Geological Association of Canada - Mineralogical Association of Canada Joint Meeting.

Corbett, G. (2018). Fluid mixing as a mechanism for bonanza grade epithermal gold formation*. Australian Institute of Geoscientists Bulletin 48*, 83-92.

Cousens, B. L., Aspler, L. B., Chiarenzelli, J. R., Donaldson, J. A., Sandeman, H. A., Peterson, T. D., LeCheminant, A. N. (2001). Enriched Archean lithospheric mantle beneath western Churchill Province tapped during Paleoproterozoic orogenesis. *Geology, 29(9),* 827-830.

Crowe, D. E., Vaughan, R. G. (1996). Characterization and use of isotopically homogeneous standards for in situ laser microprobe analysis of $^{34}S/^{32}S$ ratios. *The American mineralogist, 81(1-2),* 187-193.

Crundwell, F. K., du Preez, N. B., & Knights, B. D. H. (2020). Production of cobalt from copper-cobalt ores on the African Copperbelt – An overview. *Minerals Engineering*, *156*. https://doi.org/10.1016/j.mineng.2020.106450

Cuney, M. L. (2005). World-class unconformity-related uranium deposits: Key factors for their genesis. *Mineral Deposit Research: Meeting the Global Challenge,* 245-248. DOI:10.1007/3-540-27946-6_64.

Daly, M. C., Fuck, R. A., Julià, J., Macdonald, D. I. M., Watts, A. B. (2018). Cratonic basin formation: a case study of the Parnaíba Basin of Brazil. *Geological Society, London, Special Publications*, *472*(1), 1-15. https://doi.org/10.1144/sp472.20

Dazé, A., Lee, J.K.W., Villeneuve, M. (2003). An intercalibration study of the Fish Canyon sanidine and biotite 40Ar/39Ar standards and some comments on the age of the Fish Canyon Tuff. *Chem. Geol. 199*, 111-127.

Davis, W. J., St-Onge, M. R. (2018). Wopmay orogen revisited: Phase equilibria modeling, detrital zircon geochronology, and U-Pb monazite dating of a regional Buchan-type metamorphic sequence. *GSA Bulletin, 130(3/4),* 678–704 https:// doi .org /10 .1130 /B31809 .1;

Davis, W. J., Ootes, L., Newton, L., Jackson, V., Stern, R. A. (2015). Characterization of the Paleoproterozoic Hottah terrane, Wopmay Orogen using multi-isotopic (U-Pb, Hf and O) detrital zircon analyses: An evaluation of linkages to northwest Laurentian Paleoproterozoic domains. *Precambrian Research*, *269*, 296-310. https://doi.org/10.1016/j.precamres.2015.08.012

Deb, M., & Pal, T. (2015). Chapter 21 Mineral potential of Proterozoic intracratonic basins in India. *Geological Society, London, Memoirs*, *43*(1), 309-325. https://doi.org/10.1144/m43.21

Demir, Y., Uysal, I., & Sadıklar, M. B. (2013). Mineral chemical investigation on sulfide mineralization of the Istala deposit, Gümüşhane, NE-Turkey. *Ore Geology Reviews*, *53*, 306-317. https://doi.org/10.1016/j.oregeorev.2013.01.014

Deyell, C. L. (2005). Sulfur isotope zonation at the Mt Polley alkalic porphyry Cu-Au deposit, British Columbia, Canada. *Mineral Deposit Research: Meeting the Global Challenge*, 373-376.

Driesner T., and Heinrich C.A. (2007): The System H_2O-NaCl. I. Correlation Formulae for Phase Relations in Temperature-Pressure-Composition Space from 0 to 1000°C, 0 to 5000 bar, and 0 to 1 X_{NaCl}. *Geochimica et Cosmochimica Acta, 71*, 4880-4901.

Driesner T. (2007). The System H_2O-NaCl. II. Correlations for molar volume, enthalpy, and isobaric heat capacity from 0 to 1000 degrees C, 1 to 5000 bar, and 0 to 1 X_{NaCl}. *Geochimica et Cosmochimica Acta, 71(20)*, 4902-4919.

Eastwood, A., Oze, C., Fraser, S. J., Cole, J., Gravley, D., Chambefort, I., & Gordon, K. C. (2015). Application of Raman spectroscopy to distinguish adularia and sanidine in drill cuttings from the Ngatamariki Geothermal Field, New Zealand. *New Zealand Journal of Geology and Geophysics*, *58(1),* 66-77. https://doi.org/10.1080/00288306.2014.991744

Fayek, M., Utsunomiya, S., Ewing, R., Riciputi, L., Jensen, K. (2003). Oxygen isotopic composition of nano-scale uraninite at the Oklo-Okélobondo natural fission reactors, Gabon. *American Mineralogist, 88*. 10.2138/am-2003-1021.

Fekete, S., Weis, P., Driesner, T., Bouvier, A., Baumgartner, L., Heinrich, C. (2016). Contrasting hydrological processes of meteoric water incursion during magmatic-hydrothermal ore deposition: an oxygen isotope study by ion microprobe. *Earth and planetary science letters, 451*, 263-271.

Field, C. W., Zhang, L., Dilles, J. H., Rye, R. O., Reed, M. H. (2005). Sulfur and oxygen isotopic record in sulfate and sulfide minerals of early, deep, pre-Main Stage porphyry Cu–Mo and late Main Stage base-metal mineral deposits, Butte district, Montana. *Chemical Geology*, *215*(1-4), 61-93. https://doi.org/10.1016/j.chemgeo.2004.06.049

Frenzel, M., Hirsch, T., Gutzmer, J. (2016). Gallium, germanium, indium, and other trace and minor elements in sphalerite as a function of deposit type — A meta-analysis. *Ore Geology Reviews*, *76*, 52-78. https://doi.org/10.1016/j.oregeorev.2015.12.017

Flowers, R. M., Bowring, S. A., Williams, M. L. (2006). Timescales and significance of high-pressure, high-temperature metamorphism and mafic dike anatexis, Snowbird tectonic zone, Canada. *Contributions to Mineralogy and Petrology*, *151*(5), 558-581. https://doi.org/10.1007/s00410-006-0066-7

Gadd, M., Layton-Matthews, D., Peter, J., Paradis, S. (2016). The world-class Howard's Pass SEDEX Zn-Pb district, Selwyn Basin, Yukon. Part I: trace element compositions of pyrite record input of hydrothermal, diagenetic, and metamorphic fluids to mineralization. *Mineralium Deposita, 51,* 319-342. 10.1007/s00126-015-0611-2.

Gandhi, S. S ; van Breemen, O. (2005). SHRIMP U-Pb geochronology of detrital zircons from the Treasure Lake Group; new evidence for Paleoproterozoic collisional tectonics in the southern Hottah Terrane, northwestern Canadian Shield. *Canadian Journal of Earth Sciences*, *42(5),* 833-845.

Götze, J., Pan, Y., Stevens-Kalceff, M., Kempe, U., & Müller, A. (2015). Origin and significance of the yellow cathodoluminescence (CL) of quartz. *American Mineralogist*, *100*(7), 1469-1482. https://doi.org/10.2138/am-2015-5072

Götze, J., Schertl, H., Neuser, R. D., Kempe, U., Hanchar, J. M. (2013). Optical microscope-cathodoluminescence (OM–CL) imaging as a powerful tool to reveal internal textures of minerals. *Miner. Petrol., 107*, 373–392. doi: 10.1007/s00710-012-0256-0.

Götze, J., Schertl, H.-P., Neuser, R. D., Kempe, U., & Hanchar, J. M. (2012). Optical microscope-cathodoluminescence (OM–CL) imaging as a powerful tool to reveal internal textures of minerals. *Mineralogy and Petrology*, *107*(3), 373-392. https://doi.org/10.1007/s00710-012-0256-0

Goad, R. E., Webb, D. R. (1989). Report on the prospecting, geological mapping and sampling and data evaluation program on the Salkeld Lake claims, Mackenzie (South) district, Northwest Territories, Fortune Minerals Limited.

Godet, A., Guilmette, C., Labrousse, L., Smit, M. A., Cutts, J. A., Davis, D. W., & Vanier, M. A. (2021). Lu–Hf garnet dating and the timing of collisions: Palaeoproterozoic accretionary tectonics revealed in the Southeastern Churchill Province, Trans-Hudson Orogen, Canada. *Journal of Metamorphic Geology*, *39*(8), 977-1007. https://doi.org/10.1111/jmg.12599

Goldstein, R.H. (2003). Petrographic analysis of fluid inclusions. In: Samson, I., Anderson, A. and Marshall, D. (eds), Fluid inclusions – analysis and interpretation. *Mineralogical Association of Canada, Short Course Series 32*, 9-53.

Grondahl, C., & Zajacz, Z. (2017). Magmatic controls on the genesis of porphyry Cu–Mo–Au deposits: The Bingham Canyon example. *Earth and Planetary Science Letters*, *480*, 53-65. https://doi.org/10.1016/j.epsl.2017.09.036

Haest, M., Muchez, P., Dewaele, S., Boyce, A. J., von Quadt, A., & Schneider, J. (2009). Petrographic, fluid inclusion and isotopic study of the Dikulushi Cu–Ag deposit, Katanga (D.R.C.): implications for exploration. *Mineralium Deposita*, *44*(5), 505-522. https://doi.org/10.1007/s00126-009-0230-x

Hatert, F. (2003). Occurrence of sulphides on the bornite-idaite join from Vielsalm, Stavelot Massif, Belgium. *Eur. J. Mineral. 15*, 1063–1068.

Hatert, F. (2005). Transformation sequences of copper sulphides at Vielsam, Stavelot Massif, Belgium. *The Canadian Mineralogist 43*, 623-635.

Harrison, T. M., Célérier, J., Aikman, A. B., Hermann, J., Heizler, M. T. (2009). Diffusion of ^{40}Ar in muscovite. *Geochimica et Cosmochimica Acta*, *73*(4), 1039-1051. https://doi.org/10.1016/j.gca.2008.09.038

Harrison, T. M., Duncan, I., McDougall, I. (1985). Diffusion of ^{40}Ar in biotite: Temperature, pressure and compositional effects. *Geochimica et Cosmochimica Acta, 49(11)*, 2461-2468. https://doi.org/10.1016/0016-7037(85)90246-7

Harlaux, M., Kouzmanov, K., Gialli, S., Clark, A. H., Laurent, O., Corthay, G., Prado Flores, E., Dini, A., Chauvet, A., Ulianov, A., Chiaradia, M., Menzies, A., Villón D. G., Kalinaj, M., Fontboté, L. (2021). The upper Oligocene San Rafael intrusive complex (Eastern Cordillera, southeast Peru), host of the largest-known high-grade tin deposit. *Lithos, 400-401*, 106409.

Hitzman, M., Selley, D., Bull, S. (2010). Formation of Sedimentary Rock-Hosted Stratiform Copper Deposits through Earth History. *Economic Geology, 105,* 627-639. 10.2113/gsecongeo.105.3.627.

Hoeve J., Sibbald, T. I. (1978). On the genesis of Rabbit Lake and other unconformity-type uranium deposits in northern Saskatchewan, Canada. *Economic Geology, 73(8),* 1450-1473. https://doi.org/10.2113/gsecongeo.73.8.1450

Hoggard, M. J., Czarnota, K., Richards, F. D., Huston, D. L., Jaques, A. L., & Ghelichkhan, S. (2020). Global distribution of sediment-hosted metals controlled by craton edge

stability. *Nature Geoscience*, *13*(7), 504-510. https://doi.org/10.1038/s41561-020-0593-2

Holliger, P., Cathelineau, M. (1988). In situ U-Pb age determination by secondary ion mass spectrometry. *Chemical geology,70 (1),* 173-173.

Horita, J. (2014). Oxygen and carbon isotope fractionation in the system dolomite-water-CO2 to elevated temperatures. *Geochimica et Cosmochimica Acta 129,* 111-124.

Hunt J.A., Baker T., Gillen D., Thorkelson D.J. (2005). Wernecke breccia, Canada: A large-scale Proterozoic IOCG system related to basin evolution. In: Mao J., Bierlein F.P. (eds) Mineral Deposit Research: Meeting the Global Challenge. Springer, Berlin, Heidelberg. https://doi.org/10.1007/3-540-27946-6_33

Hunt J.A., (2004). The geology and genesis of iron oxide-copper-gold mineralisation associated with Wernecke Breccia, Yukon, Canada. PhD Thesis, James Cook University, Australia: 120.

Hutchinson, C. S. (1983). *Economic deposits and their tectonic setting.* The MacMillan Press LTD. DOI 10.1007/978-1-349-17039-5.

International Atomic Energy Agency (IAEA). (2018). Unconformity-related uranium deposits. *Tecdoc Series-1857.*

Ielpi, A., Martel, E., Fischer, B., Pehrsson, S. J., Tullio, M., & Neil, B. J. C. (2021). A reappraisal of the Nonacho Basin (Northwest Territories, Canada): Record of post-orogenic collapse and marine flooding in the Palaeoproterozoic of the Rae Craton. *Precambrian Research*, *358*. https://doi.org/10.1016/j.precamres.2021.106140

Ioannou, S. E., Götze, J., Weiershäuser, L., Zubowski, S. M., & Spooner, E. T. C. (2004). Cathodoluminescence characteristics of Archean volcanogenic massive sulfide

related quartz: Noranda, Ben Nevis and Matagami districts, Abitibi Subprovince, Canada. *Geochemistry, Geophysics, Geosystems*, *5*(2), n/a-n/a. https://doi.org/10.1029/2003gc000613

Jacobsen, J. B. E., McCarthy, T. S. (1976). The copper-bearing breccia pipes of the Messina district South Africa. *Mineral. Deposita, 11,* 33-45.

Jacobsen, J. B. E., McCarthy, T. S. (1976). An unusual hydrothermal copper deposit at Messina, South Africa. *Economic Geology, 71,* 117-130.

Johnson, C. A., Piatak, N. M., Miller, M. M. (2017). Barite (Barium), chap. D, Critical mineral resources of the United States—Economic and environmental geology and prospects for future supply: U.S. Geological Survey Professional Paper 1802, p. D1–D18, https://doi.org/10.3133/ pp1802D.

John, D. A., Garside, L. J., Wallace, A. R. (1999). Magmatic and tectonic setting of late Ceonozic epithermal gold-silver deposits in northern Nevada, with an emphasis on the Pah Rah and Virginia ranges and the northern Nevada rift. *Geological Society of Nevada, Special Publication no. 29*, 65-158.

Jefferson, C.W., Thomas, D.J., Gandhi, S., Ramaekers, P., Delaney, G.D., Brisbin, D., Cutts, C.J., Portella, P., & Olson, R.A. (2007). Unconformity-associated uranium deposits of the Athabasca Basin, Saskatchewan and Alberta. In *Bulletin of the Geological Survey of Canada 588,* 23-67. DOI:10.4095/223744

Juliani, C., Rodrigues de Assis, R., Virgínia Soares Monteiro, L., Marcello Dias Fernandes, C., Eduardo Zimmermann da Silva Martins, J., & Ricardo Costa e Costa, J. (2021). Gold in Paleoproterozoic (2.1 to 1.77 Ga) Continental Magmatic Arcs at the Tapajós and Juruena Mineral Provinces (Amazonian Craton, Brazil): A

New Frontier for the Exploration of Epithermal–Porphyry and Related Deposits. *Minerals*, *11*(7). https://doi.org/10.3390/min11070714

Keays, R. R., Lightfoot, P. C. (2015). Geochemical stratigraphy of the Keweenawan Midcontinent Rift volcanic rocks with regional implications for the genesis of associated Ni, Cu, Co, and platinum group element sulfide mineralization. *Economic geology and the bulletin of the Society of Economic Geologists, 110(5),* 1235-1267

Kellett, D. A., Pehrsson, S., Skipton, D. R., Regis, D., Camacho, A., Schneider, D. A., & Berman, R. (2020). Thermochronological history of the Northern Canadian Shield. *Precambrian Research*, *342*. https://doi.org/10.1016/j.precamres.2020.105703

Khosravi, M., Rajabzadeh, M. A., Mernagh, T. P., Qin, K., Bagheri, H., & Su, S. (2020). Origin of the ore-forming fluids of the Zefreh porphyry Cu–Mo prospect, central Iran: Constraints from fluid inclusions and sulfur isotopes. *Ore Geology Reviews*, *127*. https://doi.org/10.1016/j.oregeorev.2020.103876

Kirkham, R.V. (1996). Volcanic redbed copper; In *Geology of Canadian Mineral Deposit Types*, *Geological Survey of Canada, Geology of Canada, 8*, 241-252.

Kirkham, R.V, Carriere, J.J., Laramee, R.M., Garson, D.F., (1994). Global distribution of sediment-hosted stratiform copper deposits and occurrences. *Geological Survey of Canada Open File 2915b*, 256.

Kindle, E. D. (1972). Classification and description of copper Deposits, Coppermine River area, District of Mackenzie. *Geological Survey of Canada, Bulletin 214.* https://doi.org/10.4095/102298

Knauth, L. P. (2005). Temperature and salinity history of the Precambrian ocean: implications for the course of microbial evolution. *Palaeogeography, Palaeoclimatology, Palaeoecology*, *219*(1-2), 53-69. https://doi.org/10.1016/j.palaeo.2004.10.014

Kotzer, T., Kyser, T. K. (1990). Fluid history of the Athabasca Basin and its relation to uranium deposits. In *Summary of Investigations*, Saskatchewan Geological Survey, Saskatchewan Energy and Mines, Miscellaneous Report 90-4.

Kuiper, K.F., Deino, A., Hilgen, F.J., Krijgsman, W., Renne, R., Wijbrans, J.R. (2008). Synchronizing Rock Clocks of Earth History. *Science, 320,* 500-504.

Kyser, K. (2014). Uranium Ore Deposits, In Turekian, H. D., Holland, H. D., (eds.), Treatise on Geochemistry (2nd ed.): Oxford, Elsevier, v. 7, p. 489–513.

Kyser, T. K. (2007). Fluids, basin analysis, and mineral deposits. *Geofluids*, *7*(2), 238-257. https://doi.org/10.1111/j.1468-8123.2007.00178.x

Lang, J.R. and Baker, T. (2001). Intrusion-related gold systems: the present level of understanding. *Mineralium Deposita 36,* 477–489.

Leach, D. L., Taylor, R. D., Fey, D. L., Diehl, S. F., Saltus, R. W. (2010). A deposit model for Mississippi Valley-Type lead-zinc ores, chap. A, *of Mineral deposit models for resource assessment: U.S. Geological Survey Scientific Investigations Report 2010–5070–A*, 52.

Legault, M., Daigneault, R. (2006). Synvolcanic gold mineralization within a deformation zone: the Chevrier deposit, Chibougamau, Abitibi Subprovince, Canada. *Mineralium Deposita*, *41*(3), 203-228. https://doi.org/10.1007/s00126-006-0051-0

Le Roux, J. P. (1982). Geological principles of exploration for sandstone-hosted uranium deposits. *Nuclear development corporation of South Africa, 70,* 1-23.

Liu Z., Peng, S., Qin, M., Lui, h., Huang, S., He, Z., Guo, Q., Xu, Q., Song, J. (2017). Multistage enrichment of the Sawafuqi uranium deposit: new insights into sandstone-hosted uranium deposits in the intramontane basins of Tian Shan, China. *Acta Geologica Sinica, 91(6),* 2138-2152.

Liu, H., Liu, J., Sun, S., Zhai, M. (2003). Shear-hosted Mesothermal Vein System in the Jiapigou Goldfield, Northeast China: Implication for Subsequent Exploration. *Resource geology, 53(1),* 1-10.

Lopes, R. W., Mexias, A. S., Philipp, R. P., Bongiolo, E. M., Renac, C., Bicca, M. M., & Fontana, E. (2018). Au Cu Ag mineralization controlled by brittle structures in Lavras do Sul Mining District and Seival Mine deposits, Camaquã Basin, southern Brazil. *Journal of South American Earth Sciences*, *88*, 197-215. https://doi.org/10.1016/j.jsames.2018.08.017

Magnall, J. M., Gleeson, S. A., Stern, R. A., Newton, R. J., Poulton, S. W., & Paradis, S. (2016). Open system sulphate reduction in a diagenetic environment – Isotopic analysis of barite (δ34S and δ18O) and pyrite (δ34S) from the Tom and Jason Late Devonian Zn–Pb–Ba deposits, Selwyn Basin, Canada. *Geochimica et Cosmochimica Acta*, *180*, 146-163. https://doi.org/10.1016/j.gca.2016.02.015

Mahon, K. I., Harrison, M. T, McKeegan, K. D. (1997). The thermal and cementation histories of a sandstone petroleumreservoir, Elk Hills, California. Part 2: in situ oxygen and carbon isotopic results. *Chemical Geology, 152*, 257–271.

Markey, R., Stein, H. J., Hannah, J. L., Selby, D., Creaser, R. A.)2007). Standardizing Re-Os geochronology: A new molybdenite Reference Material (Henderson, USA) and the stoichiometry of Os salts. *Chemical Geology, 244*, 74-87.

Maynard, J. B., Okita, P. M. (1991). Bedded barite deposits in the United States, Canada, Germany, and China: Two major types based on tectonic setting. *Economic Geology, 86,* 364-376.

McCuaig, T.C. and Kerrich, R. (1998). P-T-t-deformation-fluid characteristics of lode gold deposits: evidence from alteration systematics. *Ore Geology Reviews 12*, 381–453.

McKenzie, D. (1978). Some remarks on the development of sedimentary basins. *Earh and Planetary Science Letters, 40,* 25-32. https://doi.org/10.1016/0012-821X(78)90071-7

Middleton, M. F. (1989). A model for the formation of intracratonic sag basins. *Geophysics, 99,* 665-676.

Mikaeili, K., Hosseinzadeh, M., Moayyed, M., & Maghfouri, S. (2018). The Shah-Ali-Beiglou Zn-Pb-Cu (-Ag) Deposit, Iran: An Example of Intermediate Sulfidation Epithermal Type Mineralization. *Minerals*, *8*(4). https://doi.org/10.3390/min8040148

Mikulski, S. Z., Oszczepalski, S., Sadłowska, K., Chmielewski, A., & Małek, R. (2020). Trace Element Distributions in the Zn-Pb (Mississippi Valley-Type) and Cu-Ag (Kupferschiefer) Sediment-Hosted Deposits in Poland. *Minerals*, *10*(1). https://doi.org/10.3390/min10010075

Micklethwaite, S. (2010). Fault-induced damage controlling the formation of Carlin-type ore deposits. Conference: Great Basin Evolution and Metallogeny.

Micko, J. (2005). The geology and genesis of the central zone alkalic copper-gold porphyry deposit, Galore Creek district, Northwestern British Columbia, Canada. PhD Thesis. The University of British Columbia.

Milton, J. E. (2015). Sedimentary rock hosted copper mineralization in the Neoproterozoic Redstone Copperbelt, Mackenzie Mountains, Northwest Territories, Canada. PhD Thesis. The University of British Columbia.

Min, K., Mundil, R., Renne, P.R., Ludwig, K.R. (2000). A test for systematic errors in 40Ar/39Ar geochronology through comparison with U/Pb analysis of a 1.1-Ga rhyolite. *Geochim. Cosmochim. Acta, 64*, 73-98.

Moroskat, M., Gleeson, S. A., Sharp, R. J., Simonetti, A., & Gallagher, C. J. (2014). The geology of the carbonate-hosted Blende Ag–Pb–Zn deposit, Wernecke Mountains, Yukon, Canada. *Mineralium Deposita*, *50*(1), 83-104. https://doi.org/10.1007/s00126-014-0525-4

Muchez, P., André-Mayer, A.-S., El Desouky, H. A., & Reisberg, L. (2015). Diagenetic origin of the stratiform Cu–Co deposit at Kamoto in the Central African Copperbelt. *Mineralium Deposita*, *50*(4), 437-447. https://doi.org/10.1007/s00126-015-0582-3

Mumford, T. R., Cousens, B. L., Hanley, J. (2014). Constraints on the relationships between Paleoproterozoic intrusions and dyke swarms, east arm of Great Slave Lake, N.W.T., Canada. *Canadian journal of earth sciences, 51(5),* 419-438.

Neil, B., Gibson, H., Pehrsson, S., Martel, E., Thiessen, E., Crowley, J., (2021). Provenance, stratigraphic and precise depositional age constraints for an outlier

of the 1.9 to 1.8 Ga Nonacho Group, Rae craton, Northwest Territories, Canada *Precambrian research, 352.* https://doi.org/10.1016/j.precamres.2020.105999

Neumayr, P., Walshe, J., Hagemann, S., Petersen, K., Roache, A., Frikken, P., Horn, L., Halley, S. (2007). Oxidized and reduced mineral assemblages in greenstone belt rocks of the St. Ives gold camp, Western Australia: vectors to high-grade ore bodies in Archaean gold deposits? *Mineralium Deposita*, *43*(3), 363-371. https://doi.org/10.1007/s00126-007-0170-2

Ng, R., Alexandre, P., Kyser, K. (2013). Mineralogical and geochemical evolution of the unconformity-related McArthur River Zone 4 orebody in the Athabasca Basin, Canada: implications of a silicified zone. *Economic Geology, 108(7)*, 1657–1689.

Ohomoto, H., (1986). Stable isotope geochemistry of ore deposits. In *Stable Isotopes in High Temperature Geological Processes, Reviews in Mineralogy 16*, 491-560.

Oriolo, S., Oyhantçabal, P., Wemmer, K., Basei, M. A. S., Benowitz, J., Pfänder, J., Hannich, F., Siegesmund, S. (2016). Timing of deformation in the Sarandí del Yí Shear Zone, Uruguay: Implications for the amalgamation of western Gondwana during the Neoproterozoic Brasiliano-Pan-African Orogeny. *Tectonics*, *35*(3), 754-771. https://doi.org/10.1002/2015tc004052

Oszczepalski, S., & Blundell, D. (2005). 7–4: Kupferschiefer Copper Deposits of SW Poland. *Ore Geology Reviews*, *27*(1-4). https://doi.org/10.1016/j.oregeorev.2005.07.009

Oszczepalski, S., Speczik, S., Zieliński, K., & Chmielewski, A. (2019). The Kupferschiefer Deposits and Prospects in SW Poland: Past, Present and Future. *Minerals*, *9*(10). https://doi.org/10.3390/min9100592

Paradis, S., Hannigan, P., Dewing, K. (2007). Mississippi Valley-type lead-zinc deposits (MVT). *MVT Synthesis.*

Pass, H. E., Cooke, D. R., Davidson, G., Maas, R., Dipple, G. M., Rees, C., Ferreira, L., Taylor, C., Deyell, C. (2014). Isotope geochemistry of the northeast zone, Mount Polley alkalic Cu-Au-Ag porphyry deposit, British Columbia; a case for carbonate assimilation. *Economic geology and the bulletin of the Society of Economic Geologists, 109(4),* 859-890.

Paton, C., Hellstrom, J., Paul, B., Woodhead, J., Hergt, J. (2011). Iolite: Freeware for the Visualisation and Processing of Mass Spectrometric Data. J. Anal. At. Spectrom. VL - IS -. online. 10.1039/C1JA10172B.

Pehrsson, S.J., Campbell, J.E., Martel, E., McCurdy, M.W., Agosta-Gongora, P., Theissen, E., Jamieson D., Lauzon, G., Buller G., Falck H., Dyke, A.S. (2015). Report of 2015 activities for the geologic and metallogenic framework of the South Rae Craton, Southeast Northwest Territories: GEM 2 South Rae Quaternary and Bedrock Project. Geological Survey of Canada, open file 7958.

Perelló, J., Sillitoe, R. H., & Creaser, R. A. (2020). Mesoproterozoic porphyry copper mineralization at Mamainse Point, Ontario, Canada in the context of Midcontinent rift metallogeny. *Ore Geology Reviews*, *127*. https://doi.org/10.1016/j.oregeorev.2020.103831

Peterson T. D., Van Breeman, O., Sandeman, H., Cousens, B. (2002). Proterozoic (1.85-1.75 Ga) igneous suites of the Western Churchill Province: granitoid and ultrapotassic magmatism in a reworked Archean hinterland. *Precambrian Research, 119,* 73-100.

Peterson T. D., Van Breeman, O. (1999). Review and progress report of Proterozoic granitoid rocks of the western Churchill Province, Northwest Territories (Nunavut). In *Current Research, 1999-C;* Geological Survey of Canada.

Rainbird, R. H., Davis, W. J., Pehrsson, S. J., Wodicka, N., Rayner, N., & Skulski, T. (2010). Early Paleoproterozoic supracrustal assemblages of the Rae domain, Nunavut, Canada: Intracratonic basin development during supercontinent break-up and assembly. *Precambrian Research*, *181*(1-4), 167-186. https://doi.org/10.1016/j.precamres.2010.06.005

Rauchenstein-Martinek, K., Wagner, T., Wälle, M., and Heinrich, C.A. (2014). Gold concentrations in metamorphic fluids: A LA-ICPMS study of fluid inclusions from the Alpine orogenic belt. *Chemical Geology 385,* 70-83.

Rauchenstein-Martinek, K., Wagner, T., Wälle, M., Heinrich, C.A., and Arlt, T. (2016). Chemical evolution of metamorphic fluids in the Central Alps, Switzerland: insight from LA-ICPMS analysis of fluid inclusions. *Geofluids 16,* 877-908.

Rusk, B.G., Reed, M.H., Dilles, J.H., Klemm, L.M. and Heinrich, C.A. (2004a). Compositions of magmatic hydrothermal fluids determined by LA-ICP-MS of fluid inclusions from the porphyry copper–molybdenum deposit at Butte, MT. *Chemical Geology 210(1–4),* 173–199.

Reed, M. H. (2006). Sulfide Mineral Precipitation from Hydrothermal Fluids. *Reviews in Mineralogy and Geochemistry*, *61*(1), 609-631. https://doi.org/10.2138/rmg.2006.61.11

Reed M., Rusk, B., Palandri, J. (2013). The Butte magmatic-hydrothermal system: one fluid yields all alteration and veins. *Economic Geology 108,* 1379-1396**.**

Regis, D., Pehrsson, S., Martel, E., Thiessen, E., Peterson, T., & Kellett, D. (2021). Post-1.9 Ga evolution of the south Rae craton (Northwest Territories, Canada): A Paleoproterozoic orogenic collapse system. *Precambrian Research*, *355*. https://doi.org/10.1016/j.precamres.2021.106105

Renne, P.R., Cassata, W.S., Morgan, L.E., 2009. The isotopic composition of atmospheric argon and 40Ar/39Ar geochronology: time for a change? *Quatern. Geochronol. 4*, 288-298.

Renne, P.R., Norman, E.B., 2001. Determination of the half-life of 40Ar by mass spectrometry. *Phys. Rev*. C 63 (047302), 3.

Renne P.R., Swisher C.C., Deino A.L., Karner D.B., Owens T.L. and DePaolo D.J., 1998. Intercalibration of standards, absolute ages and uncertainties in 40Ar/39Ar dating. *Chem. Geol*. 145, 117-152.

Richard, A., Pettke, T., Cathelineau, M., Boiron, M., Mercadier, J., Cuney, M., Derome, D. (2010). Brine-rock interaction in the Athabasca basement (McArthur River U deposit, Canada): Consequences for fluid chemistry and uranium uptake. *Terra Nova, 22*, 303 - 308. 10.1111/j.1365-3121.2010.00947.x.

Richards, J. P., Spooner, E. T. (1989). Evidence for Cu-(Ag) mineralization by magmatic-meteoric fluid mixing in Keweenawan fissure veins, Mamainse Point, Ontario. *Economic geology and the bulletin of the Society of Economic Geologists,* 84*(2)*, 360-385.

Riciputi, L. R., Greenwood, J. P. (1998). Analysis of sulfur and carbon isotope ratios in mixed matrices by secondary ion mass spectrometry: implications for mass bias corrections. *International journal of mass spectrometry, 178(1-2),* 65-71.

Ridley J.B. and Diamond L.W. (2000). Fluid chemistry of orogenic lode gold deposits and implications for genetic models. *Society of Economic Geology Reviews 13*, 141–162.

Robinson, G. R. (1989). Tectonic development of base-metal and barite-vein deposits associated with the early Mesozoic basins of eastern North America. *Basement Tectonics 8,* 711-725.

Roddick, J.C. (1983). High precision intercalibration of ^{40}Ar-^{39}Ar standards. *Geochim. Cosmochim. Acta 47*, 887-898.

Roedder, E. (1984). Fluid inclusions. Reviews in Mineralogy 12, 6

Romero, B., Kojima, S., Wong, C., Barra, F., Véliz, W., & Ruiz, J. (2011). Molybdenite Mineralization and Re-Os Geochronology of the Escondida and Escondida Norte Porphyry Deposits, Northern Chile. *Resource Geology*, *61*(1), 91-100. https://doi.org/10.1111/j.1751-3928.2010.00150.x

Ross, J., 2019. NMGRL/pychron. v18.2: doi: 10.5281/zenodo.3237834

Runyon, S. E., Seedorff, E., Barton, M. D., Steele-MacInnis, M., Lecumberri-Sanchez, P., Mazdab, F. K. (2019). Coarse muscovite veins and alteration in porphyry systems. *Ore Geology Reviews*, *113*. https://doi.org/10.1016/j.oregeorev.2019.103045

Runyon, S. E., Steele-MacInnis, M., Seedorff, E., Lecumberri-Sanchez, P., & Mazdab, F. K. (2017). Coarse muscovite veins and alteration deep in the Yerington batholith, Nevada: insights into fluid exsolution in the roots of porphyry copper systems. *Mineralium Deposita*, *52*(4), 463-470. https://doi.org/10.1007/s00126-017-0720-1

Ruzicka, V. (1996). Unconformity associated uranium. In *Geology of Canadian Mineral Deposit Types, 8*, 197-210.

Sack, P. J., Large, R. R., & Gregory, D. D. (2018). Geochemistry of shale and sedimentary pyrite as a proxy for gold fertility in the Selwyn basin area, Yukon. *Mineralium Deposita*, *53*(7), 997-1018. https://doi.org/10.1007/s00126-018-0793-5

Sanche, H., Jankovic, S. (2001). Report on a 1999 program of geological mapping, prospecting and rock sampling on the HART1 mineral claim, Sunrise Lake area, District of Mackenzie, NWT. Solid Resources LTD.

Sawlowicz, Z. (2013). REE and their relevance to the development of the Kupferschiefer copper deposit in Poland. *Ore Geology Reviews*, *55*, 176-186. https://doi.org/10.1016/j.oregeorev.2013.06.006

Sawkins, F. J ; Rye, R. O. (1980). Additional geochemical data on the Messina copper deposits, Transvaal, South Africa; reply. *Economic geology and the bulletin of the Society of Economic Geologists, 75 (3)*, 481-482.

Sawkins, F. J. (1977). Fluid inclusion studies of the Messina Copper deposits, Transvaal, South Africa. *Economic Geology, 72,* 619-631.

Schneider, J., Melcher, F., & Brauns, M. (2007). Concordant ages for the giant Kipushi base metal deposit (DR Congo) from direct Rb–Sr and Re–Os dating of sulfides. *Mineralium Deposita*, *42*(7), 791-797. https://doi.org/10.1007/s00126-007-0158-y

Schmidt, C., Bodnar, R. J., 2000. Synthetic fluid inclusions: XVI. PVTX properties in the system H2O-NaCl-CO2 at elevated temperatures, pressures, and salinities. *Geochimica et Cosmochimica Acta 64-22*, 3853-3869.

Selley, R. C., & Sonnenberg, S. A. (2015). Sedimentary Basins and Petroleum Systems. In *Elements of Petroleum Geology* (pp. 377-426). https://doi.org/10.1016/b978-0-12-386031-6.00008-4

Selby, D., Creaser, R. A., 2004. Macroscale NTIMS and microscale LA-MC-ICP-MS Re-Os isotopic analysis of molybdenite: Testing spatial restrictions for reliable Re-Os age determinations, and implications for the decoupling of Re and Os within molybdenite. *Geochimica et Cosmochimica Acta 68*, 3897-3908.

Shabaga, B. M., Fayek, M., Quirt, Jefferson, C. W. (2021). Geochemistry and geochronology of the Kiggavik uranium deposit, Nunavut, Canada. *Mineralium Deposita, 56(7),* 1-18. DOI:10.1007/s00126-020-01001-8

Shabaga, B. M., Fayek, M., Quirt, Ledru, P. (2020). Sources of sulphur for the Proterozoic Kiggavik uranium deposit, Nunavut, Canada. *Canadian Journal of Earth Sciences, 57(11)*, 1-12. DOI:10.1139/cjes-2018-0318

Shabaga, B. M., Fayek, M., Quirt, D., Jefferson, C. W., Camacho, A. (2017). Mineralogy, geochronology, and genesis of the Andrew Lake uranium deposit, Thelon Basin, Nunavut, Canada. *Canadian Journal of Earth Sciences*, *54*(8), 850-868. https://doi.org/10.1139/cjes-2017-0024

Sharp Z. D., Gibbons J. A., Maltsev, O., Atudorei, V., Pack, A., Sengupta, S., Shock, E. L., Knauth, L. P. (2016). A calibration of the triple oxygen isotope fractionation in the SiO2-H2O system and applications to natural samples. *Geochimica et Cosmochimica Acta 186*, 105-119.

Sharpe, R. Fayek, M., Quirt, D., Jefferson, C. W. (2015). Geochronology and Genesis of the Bong Uranium Deposit, Thelon Basin, Nunavut, Canada. *Economic Geology, 110,* 1759-1777.

Sillitoe, R., Harold, Jr. (1990). Sediment-hosted gold deposits: Distal products of magmatic-hydrothermal systems. *Geology, 18.* 10.1130/0091-7613

Smoliar, M. I., Richard J. Walker, R. J., Morgan, J. W., 1996. Re-Os ages of group IIA, IIIA, IVA, IVB iron meteorites. *Science, 271*,1099-1102.

Southard, J. 2007. 12.110 Sedimentary Geology. Massachusetts Institute of Technology: MIT openCourseWare, https://ocw.mit.edu. License: Creative Commons BY-NC-SA.

Steiger R.H., Jäger E. (1977). Subcommission on geochronology: convention on the use of decay constants in geo- and cosmochronology. *Earth Planet. Sci. Lett. 36*, 359-362.

Stein, H. J., Hannah, J. L., Zimmerman, A., Markey, R. J., Sarkar, S. C., & Pal, A. B. (2004). A 2.5 Ga porphyry Cu–Mo–Au deposit at Malanjkhand, central India: implications for Late Archean continental assembly. *Precambrian Research*, *134*(3-4), 189-226. https://doi.org/10.1016/j.precamres.2004.05.012

Steele-MacInnis, M. (2018). Fluid inclusions in the system H2O-NaCl-CO2: An algorithm to determine composition, density and isochore. *Chemical Geology*, *498*, 31-44. https://doi.org/10.1016/j.chemgeo.2018.08.022

Thiessen, E. J., Gibson, H. D., Regis, D., Pehrsson, S. J., Ashley, K. T., & Smit, M. A. (2020). The distinct metamorphic stages and structural styles of the 1.94–1.86 Ga Snowbird Orogen, Northwest Territories, Canada. *Journal of Metamorphic Geology*, *38*(9), 963-992. https://doi.org/10.1111/jmg.12556

Tombe, S. P., Richards, J. P., Greig, C. J., Board, W. S., Creaser, R. A., Muehlenbachs, K. A., Larson, P. B., DuFrane, S. A., & Spell, T. (2018). Origin of the high-grade Early Jurassic Brucejack epithermal Au-Ag deposits, Sulphurets Mining Camp,

northwestern British Columbia. *Ore Geology Reviews*, *95*, 480-517. https://doi.org/10.1016/j.oregeorev.2018.03.003

Tomlinson, Jr., Christiansen, E. H., Keith, J. D., Dorais, M. J., Ganske, R., Fernandez, D., Vetz, N., Sorensen, M., Gibbs, J. (2021). Nature and origin of zoned polymetallic (Pb-Zn-Cu-Ag-Au) veins from the Bingham Canyon porphyry Cu-Au-Mo deposit, Utah. *Economic geology and the bulletin of the Society of Economic Geologists, 116(3)*, 747-771.

Tremblay, L. P. (1982). Geology of the uranium deposits related to the sub-athabasca unconformity, Saskatchewan. Geological Survey of Canada, GSCAN-P--81-20.

Turner, E. C., Long, D. G. F. (2008). Basin architecture and syndepositional fault activity during deposition of the Neoproterozoic Mackenzie Mountains supergroup, Northwest Territories, Canada. *Canadian Journal of Earth Sciences*, *45(10),* 1159-1184. https://doi.org/10.1139/e08-062

Tuncer, V., Unsworth, M. J., Siripunvaraporn, W., Craven, J. A. (2006). Exploration for unconformity-type uranium deposits with audiomagnetotelluric data: A case study from the McArthur River mine, Saskatchewan, Canada. *Geophysics, 71(6).* DOI: 10.1190/1.2348780

Wagner, T., Okrusch, M., Weyer, S., Lorenz, J., Lahaye, Y., Taubald, H., & Schmitt, R. T. (2009). The role of the Kupferschiefer in the formation of hydrothermal base metal mineralization in the Spessart ore district, Germany: insight from detailed sulfur isotope studies. *Mineralium Deposita*, *45*(3), 217-239. https://doi.org/10.1007/s00126-009-0270-2

Weege, R.J., Pollock, J.P., and the Calumet Division Geological Staff. (1972) The geology of two new mines in the native copper district. *Economic Geology, 67,* 622-633.

White, N., Hedenquist, J. (1995). Epithermal gold deposits. Styles, characteristics and exploration. *Society of Economic Geologists, Newsletter. 23(1)*, 9-13. 10.5382/SEGnews.1995-23.fea.

White, W.S. (1968). The native copper deposits of northern Michigan. in Ridge, J.D., ed., *Ore Deposits of the United States*,(the Graton Sales volume). American Institute of Mining, Metallurgy, and Petroleum Engineering, New York, 303-325.

Wilson, A. J., Cooke, D. R., Harper, B. J., & Deyell, C. L. (2006). Sulfur isotopic zonation in the Cadia district, southeastern Australia: exploration significance and implications for the genesis of alkalic porphyry gold–copper deposits. *Mineralium Deposita*, *42*(5), 465-487. https://doi.org/10.1007/s00126-006-0071-9

Ireland, T., Cooke, D. R., Wilkinson, C. C., Wilkinson, J. J., Baker, M. J. (2020). Epidote trace element chemistry as an exploration tool in the Collahuasi District, Northern Chile. *Economic Geology, 115(4)*, 749-770. https://doi.org/10.5382/econgeo.4739

Wilkinson, J. J. (2010). A review of fluid inclusion constraints on mineralization in the Irish ore field and implications for the genesis of sediment-hosted Zn-Pb deposits. *Economic geology and the bulletin of the Society of Economic Geologists, 105(2),* 417-442.

Winter, J. (2001). *An Introduction to igneous and metamorphic petrology.* Pearson.

Wise, S. A., Watters, R. L., 2011. Reference Material 8599 Henderson Molybdenite. National Institute of Standards and Technology Report of Investigation.

Wohlgemuth-Ueberwasser, C. C., Fonseca, R. O. C., Ballhaus, C., Berndt, J. (2012). Sulfide oxidation as a process for the formation of copper-rich magmatic sulfides. *Mineralium Deposita, 48(1)*, 115-127. https://doi.org/10.1007/s00126-012-0420-9

Zeng, Q., Liu, J., Zhang, Z., Zhang, W., Chu, S., Zhang, S., Wang, Z., & Duan, X. (2011). Geology, Fluid Inclusion, and Sulfur Isotope Studies of the Chehugou Porphyry Molybdenum-Copper Deposit, Xilamulun Metallogenic Belt, NE China. *Resource Geology*, *61*(3), 241-258. https://doi.org/10.1111/j.1751-3928.2011.00161.x

Zentilli, M., Maksaev, V., Boric, R., & Wilson, J. (2018). Spatial coincidence and similar geochemistry of Late Triassic and Eocene–Oligocene magmatism in the Andes of northern Chile: evidence from the MMH porphyry type Cu–Mo deposit, Chuquicamata District. *International Journal of Earth Sciences*, *107*(3), 1097-1126. https://doi.org/10.1007/s00531-018-1595-9

Zhao, G., Sun, M., Wilde, S. A., & Li, S. (2004). A Paleo-Mesoproterozoic supercontinent: assembly, growth and breakup. *Earth-Science Reviews*, *67*(1-2), 91-123. https://doi.org/10.1016/j.earscirev.2004.02.003

Zhang, C., Sun, W., Wang, J., Zhang, L., Sun, S., Wu, K. (2017). Oxygen fugacity and porphyry mineralization: A zircon perspective of Dexing porphyry Cu deposit, China. *Geochimica et Cosmochimica Acta*, *206*, 343-363. https://doi.org/10.1016/j.gca.2017.03.013

Zhao, G., Cawood, P., Wilde, S., Sun, M. (2002). Review of global 2.1–1.8 Ga orogens: implications for a pre-Rodinia supercontinent. *Earth-Science Reviews, 59*, 125–162.

Appendices

Table 1. Normin mineral showings in the Nonacho Basin

Name	Principle commodity	Host lithology	Name	Principle commodity	Host lithology
KULT 13	Uranium	mylonite/gneiss	Maurice 6	Uranium	congl/arkose
Red	Uranium	sediment/granite	Bragon	Uranium	gabbro/gneiss
NP GRID B	Uranium	sediment/granite	Taltson 8771	Uranium	gneiss
Grant	Uranium	quartz/granite	KULT-59	Uranium	sediment
NP GRID A	Uranium	sediment/granite	Ugly Lake	Copper	congl/gneiss
Baseline and Slope	Lead	congl/arkose	Trench C	Uranium	sandstone
N80-135B	Uranium	conglomerate	Trenches A, B	Uranium	congl/mylonite
Mushroom	Uranium	congl/quartz	Trench D	Uranium	mylonite/congl
Jerome 78020	Uranium	granite/gneiss	Trench E	Uranium	mylonite/arkose
Point	Uranium	congl/arkose	Salkled Lake	Copper	akose/congl
Blue	Uranium	congl/carbonate	Lypka	Copper	granite/sediment
Steve	Uranium	congl/arkose	Taltson 78E8-9	Uranium	conglomerate
KULT 110	Uranium	gneiss/congl	Rutledge 11/12	Zinc	gneiss
Jerome Lake	Uranium	shale/arkose	Taltson 527	Uranium	gneiss
U2	Uranium	sediment/granite	Taltson 78025	Uranium	congl
KING1	Uranium	gneiss	Try Me	Uranium	greywacke
KING2	Uranium	gneiss	Taltson 481	Uranium	gneiss
KING3	Uranium	gneiss	Rutledge 10/21	Nickel	gneiss
KING4	Uranium	gneiss	Rutledge 13/22	Nickel	pelite/gneiss
KULT 6	Uranium	congl/sandstone	ZOBO	Uranium	congl
Shannon	Gold	granite/sediment	Rutledge 11/23	Copper	gneiss
341	Uranium	N/A	Joe Lake	Uranium	gneiss/sediment
Area3-3	Uranium	gneiss/congl	SES	Uranium	granite/gneiss
318	Uranium	N/A	Rutledge 10/25	Copper	gneiss
316	Uranium	N/A	Taltson 78030	Uranium	congl
Ring lake	Uranium	sediment/gneiss	Rutledge 9/27	Copper	gneiss
Mclaren	Lead	quartz/granite	Rutledge 10/27	Nickel	gneiss
Pyramid	Uranium	mylonite/amphib	Taltson 78031	Uranium	congl/gneiss
Anomaly 23	Uranium	gneiss	Rutledge 4	Copper	gneiss
Taltson 77E8-4	Uranium	sediment/granite	Rutledge 2	Copper	gneiss
KULT	Uranium	gneiss/granodiorite	Rut Conductor 9	Nickel	gneiss
MacInnis 2110	Thorium	mylonite/gneiss	Rutledge 9/31	Copper	quartz/gneiss
Maurice 14	Tantalum	arkose	Taltson 78032	Uranium	granite
MacInnis 2111	Thorium	gneiss	Rutledge 9/32	Copper	gneiss
MacInnis 1539	Uranium	mylonite/congl	Rutledge 10/34	Nickel	gneiss
Maurice 12	Tantalum	arkose	Rutledge 13/34	Copper	gneiss
MacInnis 1528	Uranium	mylonite	Rutledge 10/36	Zinc	arenite
Moffat	Tin	congl/arkose	Taltson 78034	Uranium	gneiss
KULT82	Uranium	mylonite/gneiss	Rutledge 8/38	Copper	gneiss
Cole West	Copper	mylonite/gneiss	Rutledge 8/40	Copper	gneiss
Cole	Uranium	congl/arkose	Rutledge Platinum	Platinum	gneiss
Maurice 2	Thorium	congl/arkose	Rutledge 13/43	Nickel	gneiss
MacInnis 2691	Uranium	gneiss	Rutledge 15/48	Copper	gneiss
MacInnis 2692	Uranium	congl/mylonite	Rut Conductor 13	Copper	breccia
Dussault	Uranium	arkose/siltstone	Rutledge 16/52	Nickel	gneiss
Maurice 3	Uranium	congl/arkose	CREST	Copper	quartz/greywacke
Welch	Uranium	arkose/shale	Rut Conductor 14	Copper	copper/gneiss
Laura Lake	Uranium	gneiss/sediment	ONA	Uranium	arkose
Island	Uranium	gabbro/gneiss	HOPE	Uranium	schist/gneiss
KULT-49	Uranium	sandstone/arkose	GIN	Copper	granite/gneiss
ACE	Uranium	arkose/gneiss			

Notes: congl=conglomerate; amphib=amphibolite; N/A=not available.

Table 2. Sample summary and locations

Sample No	Depth	Location	Description	Methods used
SAL-1	surface	stockwork zone	disseminated chalcopyrite in meta-sandstone	Pet;
SAL-2	surface	stockwork zone	disseminated chalcopyrite, bornite in metasandstone	Pet; CL; SEM-EDS;
SAL-3	surface	stockwork zone	disseminated chalcopyrite bornite in granitoid	Pet; CL; Ar-Ar age dating; SEM-EDS;
SAL-4	surface	shear-hosted zone	disseminated sulfides in granitic gneiss with muscovite	Pet; Ar-Ar age dating; SEM-EDS;
SAL-5	surface	shear-hosted zone	quartz breccia with chalcocite and bornite	Pet; CL, SIMS S; SEM-EDS; EPMA
SAL-6	surface	shear-hosted zone	granitic gneiss with disseminated chalcopyrite	Pet;
SAL-7	surface	shear-hosted zone	quartz vein in metasandstone with disseminated chalcopyrite	Pet; FI; Raman
SAL-8	surface	stockwork zone	quartz vein in metasandstone with disseminated chalcopyrite	Pet; Ar-Ar age dating;
SAL-9	surface	stockwork zone	sulfide-rich quartz breccia	Pet; CL; FI; SIMS O; SEM-EDS; Raman
SAL-10	surface	stockwork zone	disseminated chalcopyrite in biotite-gneiss	Pet; CL; SEM-EDS; EPMA
SAL-SA	surface	stockwork zone	sulfide-rich quartz breccia	Pet; CL; LA-ICP-MS sph; SIMS O; SEM-EDS; EPMA
HF2018-02	surface	stockwork zone	quartz vein in meta sandstone with carbonate	Pet; FI; SEM-EDS; Raman
HF2018-10	surface	stockwork zone	disseminated chalcocite and malachite in metasandstone	Pet; SEM-EDS;
HF2018-11	surface	stockwork zone	quartz vein in metasandstone with chalcopyrite replaced by bornite	Pet;
HF2018-14	surface	stockwork zone	quartz breccia with chalcocite and bornite	Pet; CL; Re-Os age dating; SEM-EDS
SLC-1	147 m	DDH sample	chalcoyrite in metasandstone with quartz and epidote	Pet; CL; FI; SIMS O; SEM-EDS; Raman
SLC-3	89 m	DDH sample	bornite and chalcocite in metasandstone with quartz veins and carbonate	Pet; CL; FI; SIMS O; SEM-EDS; Raman
SLC-12	106 m	DDH sample	disseminated chalcopyrite in red granitoid	Pet; CL

Notes: CL= cathodoluminescence; FI = fluid inclusion analyses, including petrography and microthermometry; Pet = petrography; sph = sphalerite.

Table 3a. Representative analyses (SEM-EDS) of selected major and accessory minerals

Analysis no (wt%)	1	2	3	4	5	6	7	8	9	10	11	12	13	14	15	16	17	18	19	20	21
Cu	55.5	54.0	50.7	53.6	35.8	63.7	58.5	54.1	60.9	33.5	62.0	72.6	76.5	78.3						34.6	33.7
S	32.6	32.6	29.3	32.9	34.8	25.5	26.5	27.0	23.7	36.0	38.0	27.4	23.5	21.7	38.9	38.9	39.2	14.8	14.6	27.3	27.4
Fe	11.9	14.2	19.8	13.5	29.5	10.7	11.6	12.3	7.2	28.3										5.9	5.8
Zn															60.0	60.0	60.8				
Pb																		85.2	85.4		
Cd															1.2	1.2				2.5	2.5
Sb																				28.7	28.8
Ag							3.4	6.6	8.2	2.2										1.0	2.0
Total	100.0	100.0	100.0	100.0	100.0	100.0	100.0	100.0	100.0	100.0	100.0	100.0	100.0	100.0	100.0	100.0	100.0	100.0	100.0	100.0	100.0

Notes: 1-4=idaite; 5=chalcopyrite; 6=bornite, 7-9=Ag-bornite; 10=Ag-chalcopyrite; 11=covellite; 12-13=spionkopite; 14=digenite; 15-16=Cd-sphalerite; 17=sphalerite; 18-19=galena; 20-21=tetrahedrite.

Table 3b. Representative analyses (SEM-EDS) of selected host rock mineral phases

Analysis no (wt%)	1	2	3	4	5	6	7	8	9	10	11	12
K_2O	14.5	14.2	15.8	14.5		0.2	9.5	9.9	11.1	11.0	10.7	10.9
Al_2O_3	18.1	17.9	17.9	17.9	23.1	22.3	15.9	16.0	29.3	30.4	30.4	29.5
MgO							12.4	12.9	2.8	1.8	2.0	2.1
FeO							17.5	17.2	4.7	4.8	4.9	6.7
SiO_2	65.6	65.6	66.3	66.1	63.5	64.5	42.1	41.9	52.1	51.7	52.0	50.8
Na_2O	0.7	1.0		0.8	8.6	9.3	0.4					
BaO	1.1	1.3		0.7								
TiO							1.2	1.2		0.3		
CaO					4.9	3.7						
Total	100.0	100.0	100.0	100.0	100.0	100.0	100.0	100.0	100.0	100.0	100.0	100.0

Notes: 1-4=Ba-feldspar (orthoclase); 5-6=albite; 7-8=biotite; 9-12=muscovite.

Table 4. Representative EPMA analysis of major sulfides

Sample	Mineral	Fe wt%	S wt%	Zn wt%	Cu wt%	Pb wt%	Cd wt%	Ag wt%	Total
10a-1	id	14.16	32.55	0.00	54.00	0.00	0.00	0.07	100.78
10a-2	id	14.23	32.60	0.00	54.01	0.00	0.00	0.06	100.90
10a-3	id	14.11	32.20	0.00	54.46	0.00	0.00	0.02	100.79
10a-4	id	14.24	32.41	0.00	54.15	0.02	0.00	0.08	100.91
10a-5	id	15.46	32.97	0.00	51.58	0.06	0.00	0.00	100.07
10a-6	id	13.26	32.22	0.00	54.89	0.00	0.00	0.09	100.46
10a-7	id	14.18	32.33	0.00	53.85	0.07	0.00	0.07	100.51
10a-8	id	13.53	32.20	0.00	54.81	0.00	0.00	0.05	100.60
10a-9	id	14.37	32.34	0.00	54.08	0.02	0.00	0.06	100.87
10a-10	id	13.34	31.88	0.00	55.93	0.06	0.00	0.02	101.23
10a-11	id	12.34	31.72	0.00	56.99	0.11	0.00	0.04	101.20
10a-13	id	13.53	31.82	0.00	55.29	0.00	0.00	0.06	100.69
10a-14	id	13.37	31.88	0.00	55.40	0.09	0.00	0.02	100.77
10a-15	id	14.32	32.18	0.00	54.25	0.05	0.00	0.03	100.83
10a-16	id	14.04	31.88	0.00	54.89	0.03	0.00	0.01	100.84
10a-17	id	14.71	32.40	0.00	53.56	0.11	0.00	0.00	100.79
10a-18	id	13.89	32.37	0.00	54.84	0.00	0.00	0.00	101.10
10a-19	id	14.02	32.48	0.00	54.43	0.00	0.00	0.02	100.95
10a-20	id	13.44	31.79	0.00	55.94	0.11	0.00	0.03	101.32
10a-21	id	13.52	31.90	0.00	55.52	0.01	0.02	0.04	101.01
10a-22	id	13.45	32.01	0.00	55.63	0.00	0.01	0.00	101.11
10a-23	id	14.71	32.37	0.00	54.31	0.08	0.00	0.05	101.52
10a-24	id	14.85	32.57	0.00	53.41	0.13	0.01	0.02	100.99
10a-25	id	13.92	31.70	0.00	55.54	0.00	0.00	0.07	101.23
10a-26	id	12.34	30.99	0.00	57.55	0.07	0.01	0.06	101.02
10a-27	id	14.31	31.82	0.00	54.59	0.10	0.01	0.09	100.92
10a-28	id	14.40	32.35	0.00	53.89	0.00	0.00	0.05	100.69
10a-29	id	13.73	31.86	0.00	55.35	0.00	0.00	0.00	100.94
10a-30	id	14.29	32.28	0.00	54.74	0.00	0.00	0.01	101.33
10a-31	id	14.34	31.53	0.00	55.00	0.12	0.00	0.00	100.99
10a-32	id	14.66	32.21	0.00	54.23	0.03	0.00	0.04	101.18
10a-33	id	14.17	31.78	0.00	54.24	0.00	0.00	0.09	100.28
10a-34	id	13.99	31.80	0.00	54.54	0.00	0.00	0.03	100.37
10a-35	id	12.41	31.21	0.00	57.12	0.07	0.03	0.05	100.89
10a-36	id	14.02	31.98	0.00	54.72	0.00	0.00	0.06	100.78
10a-37	id	13.39	31.31	0.00	56.31	0.00	0.00	0.00	101.01
10a-38	id	13.83	31.66	0.00	55.24	0.00	0.00	0.01	100.74
10a-39	id	13.41	31.50	0.00	55.16	0.03	0.00	0.07	100.17
10a-40	id	14.11	32.05	0.00	54.94	0.00	0.00	0.04	101.14
10a-41	id	15.25	32.54	0.00	52.51	0.07	0.00	0.02	100.39
10a-42	id	11.78	31.00	0.00	58.31	0.01	0.00	0.07	101.16
10a-43	id	13.23	31.55	0.00	55.86	0.02	0.00	0.03	100.71
10a-44	id	12.87	31.41	0.00	56.32	0.07	0.00	0.03	100.71
10a-45	id	14.07	31.61	0.00	54.85	0.00	0.00	0.06	100.58
10a-46	id	11.51	31.09	0.00	57.72	0.00	0.00	0.00	100.33
10a-47	id	13.98	31.70	0.00	54.07	0.05	0.00	0.01	99.81
SA-1	id	15.22	33.56	0.00	51.22	0.00	0.00	0.19	100.19
SA-2	id	14.50	33.59	0.00	51.48	0.00	0.00	0.35	99.92

Table 4 (continued)									
SA-3	id	15.57	33.31	0.00	50.78	0.00	0.00	0.27	99.93
SA-4	id	12.53	32.45	0.00	54.80	0.10	0.00	0.33	100.21
10a-67	id	13.66	31.70	0.00	54.79	0.12	0.00	0.00	100.27
10a-12	cpy	29.43	34.97	0.00	35.93	0.00	0.00	0.05	100.38
10a-48	cpy	30.16	34.84	0.00	34.83	0.08	0.00	0.00	99.91
10a-49	cpy	30.02	34.90	0.00	35.32	0.01	0.03	0.00	100.28
10a-50	cpy	30.22	34.60	0.00	35.24	0.05	0.00	0.00	100.11
10a-51	cpy	30.02	34.84	0.00	35.32	0.00	0.00	0.00	100.18
10a-52	cpy	30.11	34.66	0.00	35.26	0.01	0.00	0.00	100.04
10a-53	cpy	30.00	34.80	0.00	35.62	0.06	0.03	0.00	100.51
10a-54	cpy	30.20	34.89	0.00	35.25	0.04	0.00	0.00	100.39
10a-55	cpy	30.31	34.69	0.00	34.99	0.08	0.00	0.01	100.07
10a-56	cpy	30.42	35.02	0.00	35.13	0.00	0.00	0.01	100.58
10a-57	cpy	30.27	34.77	0.00	35.38	0.00	0.00	0.02	100.44
10a-58	cpy	30.16	34.69	0.00	35.06	0.08	0.00	0.05	100.04
10a-59	cpy	30.42	34.89	0.00	35.16	0.00	0.00	0.00	100.47
10a-60	cpy	30.16	34.71	0.00	35.27	0.00	0.00	0.00	100.15
10a-61	cpy	30.23	34.74	0.00	35.22	0.10	0.03	0.00	100.33
10a-62	cpy	29.92	34.75	0.00	35.44	0.00	0.00	0.01	100.13
10a-63	cpy	30.23	34.65	0.00	35.15	0.16	0.00	0.00	100.19
10a-64	cpy	30.29	34.55	0.00	35.19	0.00	0.00	0.02	100.06
10a-65	cpy	30.04	34.63	0.00	35.20	0.00	0.00	0.05	99.92
10a-66	cpy	30.19	34.56	0.00	35.10	0.12	0.02	0.00	99.98
10a-68	cpy	30.06	34.75	0.00	34.84	0.12	0.00	0.03	99.80
2a-1	cpy	30.07	34.48	0.00	35.04	0.00	0.00	0.00	99.59
2a-2	cpy	29.65	34.79	0.00	35.57	0.01	0.00	0.00	100.02
SA-5	cpy	30.43	34.90	0.00	34.77	0.04	0.00	0.00	100.14
SA-6	cpy	29.43	34.40	0.00	34.52	0.01	0.00	0.01	98.37
SA-7	cpy	29.14	33.98	0.00	34.42	0.01	0.00	0.12	97.68
SA-8	cpy	29.61	34.27	0.00	34.87	0.12	0.00	0.05	98.92
SLC1b-1	cpy	30.26	33.98	0.00	35.05	0.09	0.00	0.02	99.40
SLC1b-2	cpy	30.35	34.02	0.00	35.00	0.06	0.01	0.02	99.45
SLC1b-3	cpy	30.21	34.36	0.00	35.00	0.00	0.00	0.06	99.63
SLC1b-4	cpy	30.32	34.14	0.00	35.04	0.12	0.00	0.00	99.62
SLC1b-5	cpy	30.32	34.31	0.00	35.20	0.04	0.00	0.04	99.92
SLC1b-6	cpy	29.80	34.17	0.00	34.98	0.04	0.01	0.04	99.04
SLC1b-7	cpy	28.77	33.19	0.00	34.04	0.12	0.00	2.39	98.51
SLC1b-8	cpy	28.39	32.46	0.00	33.59	0.08	0.00	3.30	97.81
SLC1b-9	cpy	28.65	33.10	0.00	33.84	0.06	0.00	2.47	98.12
SLC1b-10	cpy	30.18	34.28	0.00	35.18	0.04	0.00	0.05	99.72
SLC1b-11	cpy	30.56	34.39	0.00	34.95	0.05	0.03	0.00	99.98
SLC1d-1	cpy	30.27	34.24	0.00	35.02	0.04	0.00	0.00	99.58
SLC1d-2	cpy	30.16	34.69	0.00	34.86	0.00	0.00	0.00	99.72
SLC1a-1	cpy	30.40	34.22	0.00	34.95	0.03	0.00	0.00	99.59
5b-1	bn	10.77	25.91	0.44	62.23	0.00	0.00	0.07	99.42
5b-2	bn	11.03	26.25	0.00	62.54	0.00	0.00	0.23	100.05
5b-3	bn	11.20	26.04	0.00	62.66	0.03	0.00	0.21	100.13
5b-4	bn	11.27	25.99	0.00	62.47	0.02	0.00	0.21	99.95

Table 4 (continued)									
5b-5	bn	10.98	25.88	0.00	62.85	0.06	0.00	0.24	100.01
5b-6	bn	11.12	25.92	0.00	62.45	0.03	0.00	0.26	99.78
5b-7	bn	11.15	25.80	0.00	62.66	0.00	0.00	0.23	99.84
5b-8	bn	10.84	26.05	0.00	62.18	0.00	0.00	0.16	99.23
5b-9	bn	10.88	26.09	0.00	61.82	0.13	0.00	0.15	99.06
5b-10	bn	10.77	25.66	0.00	62.78	0.05	0.00	0.12	99.38
5b-11	bn	10.90	25.77	0.00	63.04	0.00	0.00	0.12	99.83
2a-3	bn	11.12	25.56	0.00	64.07	0.09	0.00	0.03	100.87
2a-4	bn	11.08	25.64	0.00	63.32	0.09	0.00	0.02	100.16
2a-5	bn	11.09	25.68	0.00	63.70	0.10	0.00	0.02	100.59
2a-6	bn	11.07	25.89	0.00	63.91	0.09	0.00	0.05	101.02
2a-7	bn	11.37	25.90	0.00	63.28	0.00	0.00	0.01	100.55
5b-12	bn	10.69	25.67	0.00	62.31	0.00	0.00	0.11	98.78
SLC1a-2	bn	11.28	25.73	0.00	63.29	0.00	0.01	0.00	100.32
SLC1a-3	bn	11.24	26.00	0.00	63.58	0.05	0.00	0.00	100.87
SLC1a-4	bn	11.25	26.12	0.00	62.81	0.02	0.00	0.04	100.22
SLC1a-5	bn	11.10	25.56	0.00	63.49	0.09	0.00	0.06	100.30
SLC1a-6	bn	10.89	25.71	0.00	63.92	0.00	0.00	0.04	100.56
SLC1a-7	bn	11.10	25.89	0.00	63.49	0.03	0.00	0.11	100.61
SLC1a-8	bn	10.77	26.16	0.00	62.17	0.01	0.00	0.09	99.20
SLC1a-9	bn	11.04	25.58	0.00	64.39	0.00	0.00	0.14	101.15
SLC1a-10	bn	10.91	25.39	0.00	64.53	0.08	0.00	0.10	101.02
SLC1a-11	bn	11.12	26.11	0.00	62.59	0.00	0.00	0.04	99.85
5b-13	bn	10.66	25.74	0.00	62.06	0.00	0.00	0.12	98.58
5b-14	bn	10.74	25.66	0.00	62.24	0.02	0.00	0.14	98.81
5b-15	bn	10.42	25.84	0.00	60.90	0.00	0.00	0.14	97.31
5b-16	bn	10.98	25.76	0.00	62.71	0.00	0.00	0.10	99.55
5b-17	bn	10.85	25.81	0.00	62.21	0.09	0.00	0.14	99.10
5b-18	bn	10.70	25.77	0.00	62.75	0.08	0.00	0.10	99.41
5b-19	bn	10.58	25.84	0.00	62.37	0.00	0.00	0.22	99.01
5b-20	bn	10.69	25.78	0.00	62.17	0.00	0.00	0.17	98.81
5b-21	bn	9.19	25.09	0.00	64.64	0.00	0.00	0.13	99.05
HF10a-1	bn	11.05	25.55	0.00	63.91	0.00	0.00	0.06	100.56
HF10a-2	bn	11.01	25.52	0.00	64.48	0.13	0.00	0.00	101.14
HF10a-3	bn	10.91	25.79	0.00	63.46	0.03	0.00	0.03	100.22
HF10a-4	bn	10.85	25.48	0.00	63.95	0.05	0.00	0.00	100.33
HF10a-5	bn	10.92	25.76	0.00	63.85	0.00	0.01	0.05	100.58
SLC1b-12	bn	11.47	25.79	0.00	63.37	0.01	0.00	0.01	100.65
SLC1b-13	bn	11.07	25.67	0.00	62.94	0.07	0.00	0.02	99.76
SLC1b-14	bn	10.93	25.67	0.00	62.80	0.00	0.00	0.00	99.41
SLC1b-15	bn	11.64	25.93	0.00	63.25	0.12	0.00	0.01	100.95
SLC1b-16	bn	10.69	26.13	0.00	61.47	0.05	0.00	1.06	99.39
SLC1b-17	bn	10.84	25.60	0.00	64.08	0.19	0.00	0.05	100.76
SLC1b-18	bn	11.83	26.25	0.00	62.64	0.00	0.00	0.04	100.77
SLC1b-19	bn	11.51	25.93	0.00	62.77	0.00	0.00	0.06	100.27
SLC1b-20	bn	11.23	25.60	0.00	63.55	0.00	0.00	0.06	100.43
SLC1b-21	bn	11.30	25.95	0.00	62.86	0.07	0.00	0.03	100.20
SLC1b-22	bn	10.94	25.65	0.00	64.93	0.01	0.00	0.03	101.57

Table 4 (continued)									
SLC1b-23	bn	10.06	25.55	0.00	64.99	0.00	0.00	0.03	100.63
SLC1b-24	bn	10.15	25.20	0.00	65.01	0.14	0.00	0.05	100.55
SLC1b-25	bn	10.91	25.46	0.00	64.38	0.06	0.00	0.05	100.87
SLC1b-26	bn	10.89	25.43	0.00	64.82	0.00	0.00	0.02	101.16
SLC1b-27	bn	10.88	25.48	0.00	64.90	0.05	0.00	0.00	101.31
SLC1b-28	bn	11.08	25.64	0.00	63.71	0.05	0.00	0.01	100.50
SLC1b-29	bn	10.88	25.59	0.00	64.28	0.00	0.00	0.02	100.77
SLC1b-30	bn	11.01	25.45	0.00	64.48	0.07	0.00	0.06	101.07
SLC1d-2	bn	10.78	25.11	0.00	62.89	0.00	0.00	0.01	98.79
SLC1d-3	bn	11.18	25.63	0.00	63.16	0.00	0.00	0.00	99.97
SLC1d-4	bn	11.09	25.54	0.00	63.39	0.08	0.00	0.00	100.10
SLC1d-5	bn	11.19	25.81	0.00	63.00	0.00	0.00	0.04	100.04
SLC1d-6	bn	11.03	25.44	0.00	63.50	0.00	0.00	0.07	100.04
SLC1d-7	bn	11.09	25.54	0.00	63.94	0.09	0.00	0.05	100.70
SLC1d-8	bn	10.63	25.15	0.00	64.70	0.07	0.00	0.01	100.56
SLC1d-9	bn	11.20	25.94	0.00	62.87	0.01	0.00	0.00	100.03
SLC1d-10	bn	11.46	25.84	0.00	62.64	0.00	0.00	0.00	99.94
SLC1d-11	bn	11.30	25.99	0.00	63.14	0.05	0.00	0.02	100.50
SLC1a-6	bn	11.35	26.17	0.00	62.94	0.00	0.00	0.00	100.46
SLC1a-7	bn	10.67	26.28	0.00	62.94	0.00	0.00	0.00	99.89
2a-8	cc	1.41	22.71	0.00	77.09	0.00	0.00	0.05	101.25
HF10a-6	cc	0.65	22.63	0.00	78.14	0.02	0.00	0.04	101.48
HF10a-7	cc	0.07	22.71	0.00	79.23	0.00	0.01	0.00	102.03
HF10a-8	cc	0.12	22.54	0.00	79.13	0.00	0.00	0.09	101.87
HF10a-9	cc	0.93	22.56	0.00	77.64	0.04	0.00	0.02	101.21
HF10a-10	cc	0.07	22.30	0.00	79.10	0.00	0.02	0.00	101.48
HF10a-11	cc	0.02	22.45	0.00	79.73	0.01	0.00	0.02	102.24
HF10a-12	cc	0.15	22.63	0.00	78.91	0.12	0.00	0.09	101.90
HF10a-13	cc	0.03	22.76	0.00	78.89	0.00	0.00	0.00	101.68
HF10a-14	cc	0.38	22.26	0.00	78.90	0.00	0.00	0.06	101.60
HF10a-15	cc	0.27	22.77	0.00	78.49	0.00	0.00	0.00	101.53
SLC1b-31	cc	0.07	20.48	0.00	81.14	0.00	0.00	0.10	101.79
SLC1b-32	cc	0.03	20.65	0.00	81.10	0.00	0.01	0.07	101.87
SLC1b-33	cc	0.04	20.88	0.00	80.99	0.00	0.01	0.05	101.98
SLC1b-34	cc	0.02	20.76	0.00	80.66	0.00	0.00	0.11	101.56
SLC1b-35	cc	0.01	20.71	0.00	78.24	0.00	0.06	0.01	99.03
SLC1b-36	cc	0.09	20.76	0.00	80.35	0.12	0.00	0.07	101.39
SLC1b-37	cc	0.00	20.61	0.00	80.98	0.12	0.00	0.44	102.15
SLC1b-38	cc	0.05	20.92	0.00	81.46	0.00	0.00	0.01	102.44
SLC1b-39	cc	0.08	22.29	0.00	79.68	0.00	0.00	0.10	102.15
SLC1b-40	cc	0.14	22.53	0.00	79.34	0.06	0.00	0.15	102.22
SLC1d-12	cc	0.00	20.78	0.00	80.67	0.00	0.00	0.09	101.54
SLC1d-13	cc	0.04	20.73	0.00	81.12	0.13	0.01	0.07	102.09
SLC1a-8	cc	0.04	20.71	0.00	80.82	0.05	0.00	0.46	102.08
5b-12	ga	0.00	14.14	0.13	0.36	84.36	0.00	0.04	99.02
5b-13	ga	0.00	14.53	0.32	0.14	86.60	0.00	0.02	101.61
SA-9	ga	0.01	14.18	0.10	0.07	87.21	0.03	0.08	101.68
SA-10	ga	0.00	14.33	1.36	0.05	86.58	0.03	0.02	102.37

Table 4 (continued)									
SA-11	ga	0.00	14.26	0.07	0.08	85.28	0.02	0.08	99.79
SA-12	ga	0.00	14.13	0.12	0.10	86.32	0.00	0.04	100.70
SA-13	ga	0.00	14.39	0.01	0.05	86.95	0.07	0.00	101.47
SA-14	ga	0.00	14.09	0.15	0.07	86.23	0.02	0.00	100.56
SA-15	ga	0.00	14.23	0.57	0.04	85.70	0.00	0.03	100.57
SA-16	ga	0.00	14.03	0.37	0.04	86.27	0.05	0.01	100.78
SA-17	ga	0.00	14.32	0.07	0.05	87.26	0.04	0.00	101.74
SA-18	ga	0.00	14.67	0.22	0.03	86.27	0.00	0.07	101.25
SA-19	ga	0.00	14.35	0.04	0.06	86.44	0.00	0.00	100.88
SA-20	ga	0.00	14.35	0.11	0.02	87.34	0.03	0.02	101.87
SA-21	ga	0.00	13.96	0.49	0.06	84.97	0.07	0.00	99.55
SA-22	ga	0.00	14.49	0.08	0.01	85.50	0.00	0.04	100.11
5b-14	sph	0.02	32.44	63.48	0.02	0.08	1.08	0.00	97.11
SA-23	sph	0.13	32.59	65.33	0.10	0.05	0.82	0.00	99.02
5b-15	sph	0.08	32.62	63.37	0.03	0.05	1.04	0.00	97.20
5b-16	sph	0.11	32.64	63.69	0.48	0.00	1.11	0.00	98.04
5b-17	sph	0.03	32.66	63.43	0.04	0.04	1.13	0.00	97.33
5b-18	sph	0.05	32.38	63.76	0.06	0.00	0.95	0.01	97.21
5b-19	sph	0.03	32.50	63.57	0.06	0.16	1.27	0.00	97.59
5b-20	sph	0.02	32.37	63.59	0.07	0.02	1.07	0.00	97.15
SAL-5a-1	sph	0.04	33.03	63.70	0.00	0.00	1.07	0.02	97.90
SAL-5a-2	sph	0.03	33.23	63.49	0.00	0.00	1.10	0.01	97.87
SAL-5a-3	sph	0.04	32.51	63.82	0.00	0.01	1.17	0.00	97.55
SAL-5a-4	sph	0.05	33.03	64.25	0.00	0.05	0.93	0.01	98.32
SAL-5a-5	sph	0.08	32.44	64.24	0.01	0.10	0.95	0.00	97.85
SAL-5a-6	sph	0.13	33.39	65.10	0.13	0.04	0.87	0.02	99.71
SAL-5a-7	sph	0.03	33.01	65.31	0.00	0.12	0.95	0.00	99.42
SAL-5a-8	sph	0.01	32.77	65.59	0.00	0.00	0.88	0.00	99.24
SAL-5a-9	sph	0.00	32.77	65.71	0.01	0.03	0.94	0.02	99.49
SAL-5a-10	sph	0.00	32.65	65.60	0.00	0.14	0.99	0.00	99.40
SAL-5a-11	sph	0.01	32.84	65.58	0.01	0.00	0.96	0.04	99.49
SAL-5a-12	sph	0.05	32.96	65.68	0.02	0.00	1.01	0.05	99.77
SAL-5a-13	sph	0.02	32.88	65.69	0.09	0.00	0.84	0.04	99.57
SAL-5a-14	sph	0.02	32.98	66.02	0.00	0.00	0.90	0.03	99.98
SAL-5a-15	sph	0.03	33.05	66.19	0.01	0.02	0.91	0.04	100.26
SAL-5a-16	sph	0.04	32.94	65.82	0.00	0.00	0.97	0.00	99.76
SAL-5a-17	sph	0.01	32.83	66.03	0.00	0.00	0.91	0.00	99.78
SAL-5a-18	sph	0.03	33.04	65.36	0.00	0.00	0.89	0.03	99.35
SAL-5a-19	sph	0.03	32.83	65.68	0.09	0.04	0.98	0.02	99.70
SAL-5a-20	sph	0.03	32.89	65.60	0.03	0.01	0.95	0.00	99.51
SLC1b-41	ag-bn	10.22	22.03	0.00	31.55	0.00	0.05	32.62	96.47
SLC1b-42	ag-bn	10.24	21.87	0.01	32.72	0.01	0.09	31.81	96.76
SLC1b-43	silver	0.00	0.10	0.00	0.31	0.03	0.00	98.93	99.37
SLC1b-44	silver	0.01	0.08	0.00	0.21	0.00	0.00	99.03	99.33
SLC1b-45	silver	0.00	0.07	0.07	0.61	0.00	0.04	99.07	99.87
SLC1b-46	silver	0.00	0.17	0.00	0.33	0.00	0.00	98.11	98.62

Notes: cpy=chalcopyrite; id=idaite; bn=bornite; chlc=chalcocite; sph=sphalerite; ga=galena; ag=silver.

Table 5. Fluid inclusion microthermometry and salinity determinations

Sample	FIA	FI Type	Phases (21℃)	Host	Th_{carb}	T_m^{clath}	T_m^{carb}	T_m^{ice}	Th_{total}	Salinity (NaCl eq. wt%)	L_{aq} : carb
HF-02-D	2D_Fia1a	Type I	L_{aq}, L_{carb}, V_{carb}	qtz	30.2	6.5	-57.1			4.4	56.8
HF-02-D	2D_Fia1b	Type I	L_{aq}, L_{carb}, V_{carb}	qtz	29.7	6.5	-57.1			4.9	66.7
HF-02-D	2D_Fia1c	Type I	L_{aq}, L_{carb}, V_{carb}	qtz	29.0	6.5	-57.1			4.6	61.4
HF-02-D	2D_Fia1d	Type I	L_{aq}, L_{carb}, V_{carb}	qtz	29.3	6.5	-57.1			4.5	60.7
HF-02-D	2D_Fia1e	Type I	L_{aq}, L_{carb}, V_{carb}	qtz	28.7	6.5	-57.1			4.6	63.2
HF-02-D	2D_Fia1f	Type I	L_{aq}, L_{carb}, V_{carb}	qtz	31.1	6.5	-57.1			5.9	74.4
HF-02-D	2D_Fia1g	Type I	L_{aq}, L_{carb}, V_{carb}	qtz	29.1	6.5	-57.1			4.7	63.1
HF-02-D	2D_Fia1h	Type I	L_{aq}, L_{carb}, V_{carb}	qtz	29.3	6.5	-57.1			4.5	60.0
HF-02-D	2D_Fia1i	Type I	L_{aq}, L_{carb}, V_{carb}	qtz	29.2	6.5	-57.1			4.9	68.7
HF-02-D	2D_Fia2a	Type I	L_{aq}, L_{carb}, V_{carb}	qtz	28.6	6	-57.0			5.4	66.7
HF-02-D	2D_Fia2b	Type I	L_{aq}, L_{carb}, V_{carb}	qtz	29.0	6	-57.0			5.5	67.1
HF-02-D	2D_Fia2c	Type I	L_{aq}, L_{carb}, V_{carb}	qtz	28.8	6	-57.0			5.8	73.2
HF-02-D	2D_Fia2d	Type I	L_{aq}, L_{carb}, V_{carb}	qtz	29.1	6	-57.0			5.3	63.1
HF-02-D	2D_Fia3a	Type I	L_{aq}, L_{carb}, V_{carb}	qtz	29.1	6.3	-56.8			4.9	63.3
HF-02-D	2D_Fia3b	Type I	L_{aq}, L_{carb}, V_{carb}	qtz	28.9	6.3	-56.8			4.6	57.4
HF-02-D	2D_Fia3c	Type I	L_{aq}, L_{carb}, V_{carb}	qtz	28.9	6.3	-56.8			4.8	62.0
HF-02-D	2D_Fia3d	Type I	L_{aq}, L_{carb}, V_{carb}	qtz	29.0	6.3	-56.8			5.1	67.2
HF-02-D	2D_Fia3e	Type I	L_{aq}, L_{carb}, V_{carb}	qtz	29.8	6.3	-56.8			5.0	64.9
HF-02-D	2D_Fia4a	Type I	L_{aq}, L_{carb}, V_{carb}	qtz	29.1	6.3	-56.6			4.9	63.9
HF-02-D	2D_Fia4b	Type I	L_{aq}, L_{carb}, V_{carb}	qtz	29.6	6.3	-56.6			5.1	66.8
HF-02-D	2D_Fia4c	Type I	L_{aq}, L_{carb}, V_{carb}	qtz	29.9	6.3	-56.6			4.9	62.7
HF-02-D	2D_Fia4d	Type I	L_{aq}, L_{carb}, V_{carb}	qtz	29.7	6.3	-56.6			4.5	54.7
HF-02-D	2D_Fia4e	Type I	L_{aq}, L_{carb}, V_{carb}	qtz	29.3	6.3	-56.6			5.3	70.9
HF-02-D	2D_Fia4f	Type I	L_{aq}, L_{carb}, V_{carb}	qtz	29.0	6.3	-56.6			4.8	61.7
HF-02-D	2D_Fia5a	Type I	L_{aq}, L_{carb}, V_{carb}	qtz	30.7	6.3	-57.3			5.9	75.4
HF-02-D	2D_Fia5b	Type I	L_{aq}, L_{carb}, V_{carb}	qtz	30.5	6.3	-57.3			5.6	67.1
HF-02-D	2D_Fia5c	Type I	L_{aq}, L_{carb}, V_{carb}	qtz	30.5	6.3	-57.3			5.6	65.1
HF-02-D	2D_Fia5d	Type I	L_{aq}, L_{carb}, V_{carb}	qtz	30.6	6.3	-57.3			5.8	71.6
HF-02-D	2D_Fia5e	Type I	L_{aq}, L_{carb}, V_{carb}	qtz	30.6	6.3	-57.3			5.4	61.3
HF-02-D	2D_Fia5f	Type I	L_{aq}, L_{carb}, V_{carb}	qtz	30.6	6.3	-57.3			5.5	63.4
HF-02-D	2D_Fia6	Type I	L_{aq}, L_{carb}, V_{carb}	qtz	31.1	6.3	-57.3		288.1	6.2	74.1
HF-02-D	2D_Fia7a	Type I	L_{aq}, L_{carb}, V_{carb}	qtz	28.2	5.5	-57.1		293.9	6.3	71.7
HF-02-D	2D_Fia7b	Type I	L_{aq}, L_{carb}, V_{carb}	qtz	27.7	5.5	-57.1		293.9	5.1	53.5
HF-02-D	2D_Fia7c	Type I	L_{aq}, L_{carb}, V_{carb}	qtz	28.3	5.5	-57.1		293.9	5.5	58.3
SAL-7Db	7Db_Fia8a	Type I	L_{aq}, L_{carb}, V_{carb}	qtz	31.2	5.5	-57.9		286.9	7.5	82.4
SAL-7Db	7Db_Fia8b	Type I	L_{aq}, L_{carb}, V_{carb}	qtz	31.2	5.5	-57.9		300.1	7.4	75.3
SAL-7Db	7Db_Fia8c	Type I	L_{aq}, L_{carb}, V_{carb}	qtz	31.2	5.5	-57.9		319.4	7.1	63.1
SAL-7Db	7Db_Fia9a	Type I	L_{aq}, L_{carb}, V_{carb}	qtz	30.6	5.8	-57.9		325.8	5.7	64.6

Table 5 (continued)										
SAL-7Db	7Db_Fia9b	Type I	L_{aq}, L_{carb}, V_{carb}	qtz	30.6	5.8	-57.9	267.4	6.4	77.2
SAL-7Db	7Db_Fia9c	Type I	L_{aq}, L_{carb}, V_{carb}	qtz	30.0	5.8	-57.9	299.4	6.2	74.5
SAL-7Db	7Db_Fia10a	Type I	L_{aq}, L_{carb}, V_{carb}	qtz	30.6	6	-58.0		6.1	76.9
SAL-7Db	7Db_Fia10b	Type I	L_{aq}, L_{carb}, V_{carb}	qtz	30.6	6	-58.0		5.9	72.3
SAL-7Db	7Db_Fia10c	Type I	L_{aq}, L_{carb}, V_{carb}	qtz	30.6	6	-58.0		5.5	64.0
SAL-7Db	7Db_Fia10d	Type I	L_{aq}, L_{carb}, V_{carb}	qtz	30.6	6	-58.0		5.0	55.2
SAL-7Db	7Db_Fia11a	Type I	L_{aq}, L_{carb}, V_{carb}	qtz	28.7	6.7	-58.0		3.8	51.7
SAL-7Db	7Db_Fia11b	Type I	L_{aq}, L_{carb}, V_{carb}	qtz	27.7	6.7	-58.0		3.7	51.5
SAL-7Db	7Db_Fia11c	Type I	L_{aq}, L_{carb}, V_{carb}	qtz	28.7	6.7	-58.0		4.1	56.8
SAL-7Db	7Db_Fia12a	Type I	L_{aq}, L_{carb}, V_{carb}	qtz	30.9	5.5	-57.5	375.4	5.9	59.9
SAL-7Db	7Db_Fia12b	Type I	L_{aq}, L_{carb}, V_{carb}	qtz	31.2	5.5	-57.5	346.9	7.2	67.5
SAL-7Db	7Db_Fia12c	Type I	L_{aq}, L_{carb}, V_{carb}	qtz	27.9	5.5	-57.5	345.5	6.4	73.7
SAL-7Db	7Db_Fia13a	Type I	L_{aq}, L_{carb}, V_{carb}	qtz	30.4	5.6	-57.5	326.9	5.7	60.3
SAL-7Db	7Db_Fia13b	Type I	L_{aq}, L_{carb}, V_{carb}	qtz	29.9	5.6	-57.5	357.4	5.9	64.2
SAL-7Db	7Db_Fia13c	Type I	L_{aq}, L_{carb}, V_{carb}	qtz	30.8	5.6	-57.5	367.5	6.2	67.5
SAL-7Db	7Db_Fia14a	Type I	L_{aq}, L_{carb}, V_{carb}	qtz	27.0	5	-57.0	370.1	5.7	54.8
SAL-7Db	7Db_Fia14b	Type I	L_{aq}, L_{carb}, V_{carb}	qtz	28.8	5	-57.0	370.1	6.0	58.4
SAL-7Db	7Db_Fia14c	Type I	L_{aq}, L_{carb}, V_{carb}	qtz	31.1	5	-57.0		7.8	64.0
SAL-7Db	7Db_Fia14d	Type I	L_{aq}, L_{carb}, V_{carb}	qtz	28.4	5	-57.0		5.2	47.9
SAL-7Db	7Db_Fia14e	Type I	L_{aq}, L_{carb}, V_{carb}	qtz	28.2	5	-57.0		6.1	59.6
SAL-7Db	7Db_Fia18a	Type I	L_{aq}, L_{carb}, V_{carb}	qtz	29.5	3.5	-56.7		9.0	74.8
SAL-7Db	7Db_Fia18b	Type I	L_{aq}, L_{carb}, V_{carb}	qtz	25.2	3.7	-56.7	353.4	6.9	55.7
SAL-7Db	7Db_Fia18c	Type I	L_{aq}, L_{carb}, V_{carb}	qtz	28.3	5	-56.7	361.2	5.9	56.9
SAL-7Db	7Db_Fia18d	Type I	L_{aq}, L_{carb}, V_{carb}	qtz	28.0	5	-56.7	340.2	6.5	65.7
SAL-7Db	7Db_Fia18e	Type I	L_{aq}, L_{carb}, V_{carb}	qtz	29.3	5	-56.7		6.3	60.7
SAL-7Db	7Db_Fia18f	Type I	L_{aq}, L_{carb}, V_{carb}	qtz	29.7	5	-57.0		7.1	72.5
SAL-7Dc	7Dc_Fia19a	Type I	L_{aq}, L_{carb}, V_{carb}	qtz	30.6	4.5	-56.7		8.0	75.2
SAL-7Dc	7Dc_Fia19b	Type I	L_{aq}, L_{carb}, V_{carb}	qtz	30.4	5.2	-56.7		6.9	72.6
SAL-7Dc	7Dc_Fia19c	Type I	L_{aq}, L_{carb}, V_{carb}	qtz	29.9	5.8	-56.8		5.6	64.6
SAL-7Dc	7Dc_Fia19d	Type I	L_{aq}, L_{carb}, V_{carb}	qtz	30.4	4.5	-56.7		7.8	73.0
SAL-7Dc	7Dc_Fia19e	Type I	L_{aq}, L_{carb}, V_{carb}	qtz	30.4	4.5	-56.7		8.1	78.2
SAL-7Dc	7Dc_Fia19f	Type I	L_{aq}, L_{carb}, V_{carb}	qtz	30.4	4.5	-56.7		8.0	76.4
SAL-7Dc	7Dc_Fia20a	Type I	L_{aq}, L_{carb}, V_{carb}	qtz	30.5	6	-56.7		5.8	71.8
SAL-7Dc	7Dc_Fia20b	Type I	L_{aq}, L_{carb}, V_{carb}	qtz	30.0	6	-56.7		6.2	79.2
SAL-7Dc	7Dc_Fia20c	Type I	L_{aq}, L_{carb}, V_{carb}	qtz	27.7	6	-56.7		6.1	80.0
SAL-7Dc	7Dc_Fia21a	Type I	L_{aq}, L_{carb}, V_{carb}	qtz	29.6	5.8	-56.5	471.1	4.8	51.5
SAL-7Dc	7Dc_Fia21b	Type I	L_{aq}, L_{carb}, V_{carb}	qtz	29.6	5.8	-56.5	341.6	5.2	57.5
SAL-7Dc	7Dc_Fia21c	Type I	L_{aq}, L_{carb}, V_{carb}	qtz	30.6	6.3	-56.5	341.8	5.1	65.0
SAL-7Dc	7Dc_Fia21d	Type I	L_{aq}, L_{carb}, V_{carb}	qtz	30.5	6.3	-56.5	326.3	5.1	65.0

Table 5 (continued)											
SAL-7Dc	7Dc_Fia21e	Type I	L_{aq}, L_{carb}, V_{carb}	qtz	31.0	6.3	-56.5		307.3	5.9	61.0
SAL-7Dc	7Dc_Fia22a	Type I	L_{aq}, L_{carb}, V_{carb}	qtz	29.3	6.7	-56.5		348.8	4.8	71.3
SAL-7Dc	7Dc_Fia22b	Type I	L_{aq}, L_{carb}, V_{carb}	qtz	28.8	7.5	-56.5		363.9	3.0	53.8
SAL-7Dc	7Dc_Fia22c	Type I	L_{aq}, L_{carb}, V_{carb}	qtz	29.6	6.7	-56.5			3.9	51.9
SAL-7Dc	7Dc_Fia22d	Type I	L_{aq}, L_{carb}, V_{carb}	qtz	30.0	6.3	-56.5			4.9	61.6
SAL-7Dc	7Dc_Fia22e	Type I	L_{aq}, L_{carb}, V_{carb}	qtz	31.3	6.3	-56.5			5.6	51.4
SAL-7Dc	7Dc_Fia23a	Type I	L_{aq}, L_{carb}, V_{carb}	qtz	30.6	6	-56.6			6.1	76.6
SAL-7Dc	7Dc_Fia23b	Type I	L_{aq}, L_{carb}, V_{carb}	qtz	30.4	6	-56.6			5.9	73.2
SAL-7Dc	7Dc_Fia23c	Type I	L_{aq}, L_{carb}, V_{carb}	qtz	30.6	6	-56.6			5.8	71.2
SAL-7Dc	7Dc_Fia23d	Type I	L_{aq}, L_{carb}, V_{carb}	qtz	30.5	6	-56.6			5.3	61.3
SAL-7Dc	7Dc_Fia23e	Type I	L_{aq}, L_{carb}, V_{carb}	qtz	30.7	6	-56.5			5.5	64.4
SAL-7Dc	7Dc_Fia23f	Type I	L_{aq}, L_{carb}, V_{carb}	qtz	30.7	6	-56.5			6.1	76.1
SAL-7Dc	7Dc_Fia23g	Type I	L_{aq}, L_{carb}, V_{carb}	qtz	30.7	6	-56.5			5.7	68.7
SAL-7Dc	7Dc_Fia24a	Type I	L_{aq}, L_{carb}, V_{carb}	qtz	30.9	6	-56.5			6.1	75.6
SAL-7Dc	7Dc_Fia24b	Type I	L_{aq}, L_{carb}, V_{carb}	qtz	30.9	6	-56.5			5.7	66.5
SAL-7Dc	7Dc_Fia24c	Type I	L_{aq}, L_{carb}, V_{carb}	qtz	30.9	6	-56.5			5.8	69.8
SAL-7Dc	7Dc_Fia24d	Type I	L_{aq}, L_{carb}, V_{carb}	qtz	30.9	6	-56.5			5.7	67.3
SAL-7Dc	7Dc_Fia24e	Type I	L_{aq}, L_{carb}, V_{carb}	qtz	30.9	6	-56.5			6.0	72.6
SAL-7Dc	7Dc_Fia24f	Type I	L_{aq}, L_{carb}, V_{carb}	qtz	30.9	6	-56.5			4.7	49.1
SAL-7Dc	7Dc_Fia24g	Type I	L_{aq}, L_{carb}, V_{carb}	qtz	30.9	6	-56.5			6.1	75.8
SAL-7Dc	7Dc_Fia24h	Type I	L_{aq}, L_{carb}, V_{carb}	qtz	30.9	6	-56.5			5.8	69.1
SAL-7Dc	7Dc_Fia26a	Type I	L_{aq}, L_{carb}, V_{carb}	qtz	27.2	6	-56.5			6.0	78.1
SAL-7Dc	7Dc_Fia26b	Type I	L_{aq}, L_{carb}, V_{carb}	qtz	27.2	6	-56.5			4.5	52.0
SAL-7Dc	7Dc_Fia26c	Type I	L_{aq}, L_{carb}, V_{carb}	qtz	27.4	6	-56.5			3.8	42.7
SAL-7Dc	7Dc_Fia26d	Type I	L_{aq}, L_{carb}, V_{carb}	qtz	29.4	6	-56.5			5.4	65.2
SAL-7Dc	7Dc_Fia26e	Type I	L_{aq}, L_{carb}, V_{carb}	qtz	30.6	6	-56.5			5.7	68.0
SAL-7Dc	7Dc_Fia26f	Type I	L_{aq}, L_{carb}, V_{carb}	qtz	26.1	6	-56.5			3.9	44.9
SAL-7Dc	7Dc_Fia27a	Type I	L_{aq}, L_{carb}, V_{carb}	qtz	29.6	6.2	-56.5			5.2	65.9
SAL-7Dc	7Dc_Fia27b	Type I	L_{aq}, L_{carb}, V_{carb}	qtz	29.6	6.2	-56.5			5.2	64.8
SAL-7Dc	7Dc_Fia27c	Type I	L_{aq}, L_{carb}, V_{carb}	qtz	30.7	6.2	-56.5			5.7	73.3
SAL-9C	9C_Fia2a	Type II	L_{aq}, V	qtz				-3.4	182.9	5.6	86.0
SAL-9C	9C_Fia2b	Type II	L_{aq}, V	qtz				-3.4	191.5	5.6	88.5
SAL-9C	9C_Fia2c	Type II	L_{aq}, V	qtz				-3.4	182.5	5.6	85.2
SAL-9C	9C_Fia4a	Type II	L_{aq}, V	qtz				-2.7	306.7	4.5	69.8
SAL-9C	9C_Fia4b	Type II	L_{aq}, V	qtz				-2.7	294.3	4.5	74.0
SAL-9C	9C_Fia4c	Type II	L_{aq}, V	qtz				-2.7	321.4	4.5	66.9
SAL-9C	9C_Fia4d	Type II	L_{aq}, V	qtz				-2.7	311.6	4.5	67.2
SAL-9C	9C_Fia5a	Type II	L_{aq}, V	qtz				-2.6	237.1	4.3	70.3
SAL-9C	9C_Fia5b	Type II	L_{aq}, V	qtz				-2.6	239.4	4.3	75.3

Table 5 (continued)								
SAL-9C	9C_Fia6a	Type II	L_{aq}, V	qtz	-2.2	263.4	3.7	75.0
SAL-9C	9C_Fia6b	Type II	L_{aq}, V	qtz	-2.4	285.4	4.0	69.9
SAL-9C	9C_Fia6c	Type II	L_{aq}, V	qtz	-2.3	258.8	3.9	73.9
SAL-9C	9C_Fia6d	Type II	L_{aq}, V	qtz	-2.0	208.4	3.4	74.0
SAL-9C	9C_Fia7a	Type II	L_{aq}, V	qtz	-2.3	246.8	3.9	84.2
SAL-9C	9C_Fia7b	Type II	L_{aq}, V	qtz	-2.3	281.3	3.9	65.6
SAL-9C	9C_Fia7c	Type II	L_{aq}, V	qtz	-2.3	246.8	3.9	64.9
SAL-9C	9C_Fia7d	Type II	L_{aq}, V	qtz	-2.3	295.3	3.9	71.5
SAL-9C	9C_Fia7e	Type II	L_{aq}, V	qtz	-2.3	249.9	3.9	72.4
SAL-9C	9C_Fia7f	Type II	L_{aq}, V	qtz	-2.3	266.3	3.9	71.4
SAL-9C	9C_Fia10a	Type II	L_{aq}, V	qtz	-1.9	239.2	3.2	82.2
SAL-9C	9C_Fia10b	Type II	L_{aq}, V	qtz	-2.4	262.6	4.0	72.8
SAL-9C	9C_Fia10c	Type II	L_{aq}, V	qtz	-2.1	277.4	3.6	79.5
SAL-7D	7D_Fia11a	Type II	L_{aq}, V	qtz	-3.5	158.9	5.7	84.6
SAL-7D	7D_Fia11b	Type II	L_{aq}, V	qtz	-3.5	163.7	5.7	84.2
SAL-7D	7D_Fia11c	Type II	L_{aq}, V	qtz	-3.5	165.2	5.7	89.4
SAL-7D	7D_Fia12a	Type II	L_{aq}, V	qtz	-0.5	206.2	0.9	85.2
SAL-7D	7D_Fia12b	Type II	L_{aq}, V	qtz	-0.5	208.4	0.9	83.9
SAL-7D	7D_Fia13a	Type II	L_{aq}, V	qtz	-2.7	159.5	4.5	90.3
SAL-7D	7D_Fia13b	Type II	L_{aq}, V	qtz	-2.6	152.6	4.3	83.5
SAL-7D	7D_Fia13c	Type II	L_{aq}, V	qtz	-2.7	165.3	4.5	89.4
SAL-7D	7D_Fia14a	Type II	L_{aq}, V	qtz	-2.9	189.7	4.8	86.9
SAL-7D	7D_Fia14b	Type II	L_{aq}, V	qtz	-2.7	206.4	4.5	85.5
SAL-7D	7D_Fia15a	Type II	L_{aq}, V	qtz	-1.2	168.5	2.1	89.9
SAL-7D	7D_Fia15b	Type II	L_{aq}, V	qtz	-1.1	167.0	1.9	85.0
SAL-7D	7D_Fia15c	Type II	L_{aq}, V	qtz	-1.0	165.8	1.7	84.5
SAL-7D	7D_Fia15d	Type II	L_{aq}, V	qtz	-1.0	168.1	1.7	90.1
SAL-7D	7D_Fia17a	Type II	L_{aq}, V	qtz	-1.1	160.9	1.9	87.6
SAL-7D	7D_Fia17b	Type II	L_{aq}, V	qtz	-1.1	163.5	1.9	83.3
SAL-9D	9D_Fia18a	Type II	L_{aq}, V	qtz	-0.5	168.3	0.9	83.5
SAL-9D	9D_Fia18b	Type II	L_{aq}, V	qtz	-0.5	163.7	0.9	85.6
SAL-9D	9D_Fia18c	Type II	L_{aq}, V	qtz	-0.5	183.1	0.9	78.8
SAL-9D	9D_Fia18d	Type II	L_{aq}, V	qtz	-0.5	189.5	0.9	81.2
SAL-9D	9D_Fia18e	Type II	L_{aq}, V	qtz	-0.5	163.5	0.9	82.9
SAL-9D	9D_Fia18f	Type II	L_{aq}, V	qtz	-0.5	186.0	0.9	79.5
SAL-9D	9D_Fia18g	Type II	L_{aq}, V	qtz	-0.5	215.2	0.9	81.0
SAL-9D	9D_Fia20a	Type II	L_{aq}, V	qtz	-0.4	202.7	0.7	84.0
SAL-9D	9D_Fia20b	Type II	L_{aq}, V	qtz	-0.4	198.9	0.7	82.9
SAL-9D	9D_Fia20c	Type II	L_{aq}, V	qtz	-0.4	198.1	0.7	80.8

Table 5 (continued)								
SAL-9D	9D_Fia20d	Type II	L_{aq}, V	qtz	-0.4	194.4	0.7	84.9
SAL-9D	9D_Fia20e	Type II	L_{aq}, V	qtz	-0.4	177.6	0.7	73.9
SAL-9D	9D_Fia20f	Type II	L_{aq}, V	qtz	-0.4	197.2	0.7	82.6
SAL-9D	9D_Fia20g	Type II	L_{aq}, V	qtz	-0.4	185.9	0.7	83.6
SAL-9D	9D_Fia21a	Type II	L_{aq}, V	qtz	-0.6	305.3	1.1	71.8
SAL-9D	9D_Fia21b	Type II	L_{aq}, V	qtz	-0.5	327.2	0.9	75.5
SAL-9D	9D_Fia21c	Type II	L_{aq}, V	qtz	-0.4	319.6	0.7	66.9
SAL-9B	9B_Fia23a	Type II	L_{aq}, V	qtz	-3.0	158.2	5.0	81.0
SAL-9B	9B_Fia23b	Type II	L_{aq}, V	qtz	-3.0	166.3	5.0	83.0
SAL-9B	9B_Fia23c	Type II	L_{aq}, V	qtz	-3.0	164.9	5.0	87.5
SAL-9B	9B_Fia24a	Type II	L_{aq}, V	qtz	-3.0	225.8	5.0	76.6
SAL-9B	9B_Fia24b	Type II	L_{aq}, V	qtz	-3.0	246.1	5.0	77.9
SAL-9B	9B_Fia24c	Type II	L_{aq}, V	qtz	-2.3	224.6	3.9	83.3
SAL-9B	9B_Fia25a	Type II	L_{aq}, V	qtz	-2.8	289.8	4.7	76.7
SAL-9B	9B_Fia25b	Type II	L_{aq}, V	qtz	-0.5	290.1	0.9	75.6
SAL-9B	9B_Fia25c	Type II	L_{aq}, V	qtz	-0.5	291.7	0.9	76.4
SAL-9B	9B_Fia25d	Type II	L_{aq}, V	qtz	-0.5	259.4	0.9	74.1
SAL-9B	9B_Fia27a	Type II	L_{aq}, V	qtz	-1.7	215.4	2.9	83.8
SAL-9B	9B_Fia27b	Type II	L_{aq}, V	qtz	-1.8	233.5	3.1	82.3
SAL-9B	9B_Fia27c	Type II	L_{aq}, V	qtz	-1.8	216.8	3.1	79.1
SAL-9B	9B_Fia27d	Type II	L_{aq}, V	qtz	-2.0	189.8	3.4	82.5
SLC-3C	3C_Fia28a	Type II	L_{aq}, V	qtz	-0.2	148.5	0.4	90.3
SLC-3C	3C_Fia28b	Type II	L_{aq}, V	qtz	-0.2	159.2	0.4	86.0
SLC-3C	3C_Fia28c	Type II	L_{aq}, V	qtz	-0.2	206.0	0.4	84.3
SLC-3C	3C_Fia28d	Type II	L_{aq}, V	qtz	-0.2	148.5	0.4	84.4
SLC-3C	3C_Fia28e	Type II	L_{aq}, V	qtz	-0.2	157.3	0.4	81.0
SLC-3C	3C_Fia28f	Type II	L_{aq}, V	qtz	-0.2	206.0	0.4	83.5
SLC-3C	3C_Fia28g	Type II	L_{aq}, V	qtz	-0.2	160.4	0.4	86.8
SLC-3C	3C_Fia28h	Type II	L_{aq}, V	qtz	-0.2	186.1	0.4	80.5
SLC-3C	3C_Fia28i	Type II	L_{aq}, V	qtz	-0.2	156.3	0.4	88.9
SLC-3C	3C_Fia29a	Type II	L_{aq}, V	qtz	-0.1	158.1	0.2	83.8
SLC-3C	3C_Fia29b	Type II	L_{aq}, V	qtz	-0.1	173.5	0.2	87.2
SLC-3C	3C_Fia29d	Type II	L_{aq}, V	qtz	-0.1	184.3	0.2	90.1
SLC-3C	3C_Fia29e	Type II	L_{aq}, V	qtz	-0.1	172.7	0.2	81.6
SLC-3C	3C_Fia30a	Type II	L_{aq}, V	qtz	-0.1	205.8	0.2	86.4
SLC-3C	3C_Fia30b	Type II	L_{aq}, V	qtz	-0.1	184.1	0.2	81.5
SLC-3C	3C_Fia30c	Type II	L_{aq}, V	qtz	-0.1	206.1	0.2	79.1
SLC-3C	3C_Fia30d	Type II	L_{aq}, V	qtz	-0.1	239.0	0.2	84.2
SLC-3C	3C_Fia30e	Type II	L_{aq}, V	qtz	-0.1	177.0	0.2	83.8

Table 5 (continued)								
SLC-3C	3C_Fia30f	Type II	L_{aq}, V	qtz	-0.1	228.4	0.2	81.9
SLC-3C	3C_Fia30g	Type II	L_{aq}, V	qtz	-0.1	188.5	0.2	84.7
SLC-3C	3C_Fia31a	Type II	L_{aq}, V	qtz	-0.2	213.6	0.4	82.8
SLC-3C	3C_Fia31b	Type II	L_{aq}, V	qtz	-0.2	200.0	0.4	79.4
SLC-3C	3C_Fia31c	Type II	L_{aq}, V	qtz	-0.2	201.4	0.4	81.8
SLC-3C	3C_Fia31d	Type II	L_{aq}, V	qtz	-0.2	237.5	0.4	81.8
SLC-3C	3C_Fia31e	Type II	L_{aq}, V	qtz	-0.2	219.6	0.4	80.4
SLC-1D	1D_Fia1a	Type II	L_{aq}, V	cal	-1.1	179.1	1.9	81.8
SLC-1D	1D_Fia1b	Type II	L_{aq}, V	cal	-1.3	172.9	2.2	81.7
SLC-1D	1D_Fia1c	Type II	L_{aq}, V	cal	-1.8	184.9	3.1	81.0
SLC-1D	1D_Fia2a	Type II	L_{aq}, V	cal	-0.4	241.4	0.7	79.6
SLC-1D	1D_Fia2b	Type II	L_{aq}, V	cal	-0.5	251.2	0.9	83.0
SLC-1D	1D_Fia2c	Type II	L_{aq}, V	cal	-0.5	174.1	0.9	89.5
SLC-1D	1D_Fia2d	Type II	L_{aq}, V	cal	-0.5	174.4	0.9	84.1
SLC-1D	1D_Fia4a	Type II	L_{aq}, V	cal	-13.2	106.9	17.1	81.0
SLC-1D	1D_Fia4b	Type II	L_{aq}, V	cal	-13.2	117.9	17.1	87.1
SLC-1D	1D_Fia4c	Type II	L_{aq}, V	cal	-13.2	112.9	17.1	87.2
SLC-1D	1D_Fia4d	Type II	L_{aq}, V	cal	-13.2	111.0	17.1	80.1
SLC-1D	1D_Fia4e	Type II	L_{aq}, V	cal	-13.2	119.5	17.1	80.3
SAL-SC	sph_1	Type II	L_{aq}, V	sph	-21.1	63.1	23.1	90.5
SAL-SC	sph_2	Type II	L_{aq}, V	sph	-20.6	58.9	22.8	90.5
SAL-SC	sph_3	Type II	L_{aq}, V	sph	-18.9	61.5	21.6	90.5
SAL-SC	sph_4	Type II	L_{aq}, V	sph	-20.1	62.7	22.4	90.5
SAL-SC	sph_5	Type II	L_{aq}, V	sph	-20.6	62.8	22.8	90.5
SAL-SC	sph_6	Type II	L_{aq}, V	sph	-20.3	63.4	22.6	90.5
SAL-SC	sph_7	Type II	L_{aq}, V	sph	-21.4	60.9	23.2	90.5
SAL-SC	sph_8	Type II	L_{aq}, V	sph	-22.3	61.9	23.2	90.5
SAL-SC	sph_9	Type II	L_{aq}, V	sph	-21.6	64.1	23.2	90.5
SAL-SC	sph_10	Type II	L_{aq}, V	sph	-16.3	63.1	19.7	90.5
SAL-SC	sph_11	Type II	L_{aq}, V	sph	-19.8	66.1	22.4	90.5

Notes: All measurements are shown in °C. FIA = fluid inclusion assemblage; FI = fluid inclusion; Th_{carb} = homogenization temperature of the carbonic phase; T_m^{clath} = clathrate melting temperature; T_m^{ice} = ice melting temperature; T_m^{carb} = melting temperature of the carbonic phase; Th_{total} = total homogenization temperature; L_{aq}: carb = liquid to vapour ratio; wt% = weight percent; L_{aq} = aqueous liquid, L_{carb} = carbonic liquid, V_{carb} = carbonic vapour; sph = sphalerite; cal = calcite; qtz = quartz.

Table 6. Whole-rock chemistry of representative mineralized samples (ppm)											
	1	**2**	**3**	**4**	**5**	**6**	**7**	**8**	**9**	**10**	**11**
Ore and accessory metals											
Ag	204	127	93.5	598	59.5	66.9	41.6	25.1	89.0	74.9	150
As	0.70	0.80	<0.7	<0.7	<0.7	<0.7	<0.7	<0.7	<0.7	<0.7	<0.7
Au	0.39	0.20	0.043	1.24	0.26	0.14	0.054	0.006	0.12	0.081	0.44
Be	0.12	0.58	0.76	0.09	0.39	0.72	0.38	2.42	0.42	0.24	0.19
Bi	19.8	12.5	0.46	10.5	8.6	14.0	1.86	0.26	13.1	11.6	40.1
Cd	>300	7.00	44.0	>300	2.33	16.5	17.6	0.20	0.45	0.25	1.14
Co	21.1	1.80	2.00	16.10	0.70	14.5	2.90	5.60	3.60	2.80	3.90
Cu	89833	34451	6719	95366	58283	50585	9461	15144	59256	48227	125025
Hg	2.10	0.20	0.20	1.50	<0.08	<0.08	0.10	0.10	0.10	0.10	0.10
In	0.11	0.01	0.01	0.08	0.09	0.04	0.01	0.02	0.02	0.01	0.02
Ir	<0.003	<0.003	<0.003	<0.003	<0.003	<0.003	<0.003	<0.003	<0.003	0.00	0.00
Mo	379	193	13.28	213	64.6	1.93	34.05	1.05	85.5	92.8	419
Ni	4.60	1.90	1.90	8.10	2.50	18.8	5.70	3.90	5.10	3.50	3.70
Pb	33513	209	547	10297	23.0	47.0	21.9	4.7	18.0	21.0	24.0
Pd	0.02	<0.02	<0.02	0.04	<0.02	<0.02	<0.02	<0.02	<0.02	<0.02	0.04
Pt	<0.005	0.01	0.01	0.01	0.01	0.01	<0.005	0.01	0.01	0.01	<0.005
Rh	0.17	0.00	0.01	0.09	0.01	0.01	<0.003	0.00	0.01	0.01	0.01
Sb	31.54	0.20	6.97	22.79	2.30	0.48	0.34	0.13	0.10	0.08	0.34
Se	54.80	3.40	0.70	27.30	3.00	6.30	1.20	0.60	3.30	3.30	7.40
Sn	0.45	1.10	0.50	0.45	0.69	2.12	0.53	0.83	0.65	0.54	1.29
Te	11.4	4.50	0.16	4.52	4.34	3.90	0.89	0.10	2.03	2.06	7.33
Tl	0.03	0.08	0.42	0.04	0.02	0.56	0.07	0.53	0.06	0.05	0.14
W	0.05	1.65	0.67	0.07	0.41	1.04	4.64	2.18	1.32	0.84	0.75
Zn	201132	446	2982	137315	99.0	767	547	140	72.0	59.0	46.0
Th	0.25	8.23	5.78	0.41	2.60	0.74	3.95	8.96	6.98	2.94	1.65
U	0.56	1.79	1.42	0.32	0.83	0.97	1.34	2.20	1.90	1.09	0.64

Table 6. (Continued)

	1	2	3	4	5	6	7	8	9	10	11
REE + Y											
La	0.80	15.3	11.8	1.7	5.6	22.4	8.5	21.0	19.3	11.9	5.7
Ce	1.33	30.4	22.2	3.24	11.4	44.2	17.0	42.4	37.9	22.9	11.8
Pr	0.15	3.41	2.47	0.35	1.36	4.93	1.89	4.99	4.11	2.47	1.27
Nd	0.52	12.7	8.80	1.23	5.01	18.2	7.02	18.5	15.3	8.58	4.51
Sm	0.086	2.15	1.34	0.16	0.81	3.05	1.17	2.94	2.46	1.32	0.65
Eu	0.013	0.42	0.20	0.033	0.15	0.57	0.25	0.71	0.46	0.28	0.15
Gd	0.046	1.77	0.87	0.11	0.59	2.07	0.79	1.93	1.84	0.99	0.50
Tb	0.008	0.25	0.12	0.015	0.077	0.23	0.11	0.24	0.26	0.13	0.066
Dy	0.060	1.38	0.72	0.077	0.41	1.17	0.67	1.28	1.61	0.81	0.36
Ho	0.011	0.28	0.13	0.014	0.084	0.19	0.13	0.23	0.31	0.15	0.070
Er	0.039	0.89	0.40	0.043	0.25	0.50	0.39	0.65	0.98	0.45	0.21
Tm	0.006	0.12	0.060	0.008	0.034	0.067	0.0611	0.0869	0.14	0.0706	0.031
Yb	0.038	0.87	0.38	0.051	0.25	0.38	0.44	0.59	0.95	0.42	0.21
Y	0.33	8.04	3.98	0.48	2.28	5.16	3.45	6.73	9.11	4.46	2.00
Lu	0.005	0.13	0.055	0.006	0.037	0.061	0.065	0.091	0.147	0.063	0.03
LILE											
Li	2.70	5.40	19.5	3.60	3.90	24.6	9.10	18.8	4.20	3.50	4.60
Cs	0.11	0.72	2.84	0.13	0.39	2.19	0.91	0.89	0.71	0.55	0.69
Rb	4.61	79.1	105	3.98	35.2	101	157	122	201	138	40.2
Sr	3.00	58.0	33.7	3.10	15.1	49.6	82.2	403	62.9	55.2	11.7
Ba	9.10	1002	446	10.8	394	142	>1740	>1740	>1740	>1740	596
HFSE											
Zr	<6	151	59.0	6.00	32.0	40.0	63.0	192	145	58.0	33.0
Hf	<0.14	3.82	1.41	0.15	0.84	0.96	1.68	4.79	3.61	1.45	0.85
Nb	0.19	5.706	2.353	0.246	1.83	3.6	3.141	6.399	4.638	2.093	1.297
Ta	0.018	0.517	0.182	0.033	0.14	0.131	0.268	0.39	0.471	0.198	0.13
Other											
Cr	22.0	51.0	26.0	46.0	36.0	48.0	87.0	22.0	97.0	39.0	35.0
Ga	1.37	4.62	7.67	1.53	3.01	12.9	5.17	16.6	3.39	2.80	1.73
Sc	<1.1	3.60	3.10	<1.1	1.10	5.50	2.70	4.80	2.70	1.40	<1.1
Ti	40.0	1142	766	64.0	392	1256	716	2024	903	431	274
V	1.40	15.6	20.8	1.90	5.10	36.6	13.1	32.8	10.2	7.20	5.20

Notes: 1=sulphide-quartz breccia (SAL-SA); 2=sulphide-rich sandstone (SAL-2); 3=sulphide-granitic gneiss (SAL-4);4=sulphide-quartz breccia (SAL-5); 5=sulphide-granitic gneiss (SAL-6); 6=sulphide-sandstone (SAL-7); 7=sulphide-rich sandstone (SAL-8); 8=sulphide-rich sandstone (SAL-10); 9=sulphide-rich sandstone (HF-2018-10); 10=sulphide-rich sandstone (HF-2018-10b); 11=sulphide-rich sandstone (HF-2018-11).

Table 7. Geochronological data from laser Ar-Ar age dating of muscovite and biotite

Sample	Mineral	Age (Ma)	±1σ (Ma)	Ca/K	±1σ	Cl/K	±1σ	$\%^{40}Ar^*$ (%)	$^{40}Ar^*/^{39}Ar_K$	±1σ
SAL-4F-2	musc	1836.0	5.1	-0.04	0.06	0.00	0.01	99.95	182.51	0.81
SAL-4F-2	musc	1815.2	3.4	0.11	0.05	0.01	0.01	99.91	179.24	0.52
SAL-4F-2	musc	1824.5	3.4	0.02	0.04	0.01	0.01	99.99	180.70	0.53
SAL-4F-2	musc	1822.7	3.6	0.16	0.04	-0.01	0.01	99.98	180.42	0.57
SAL-4F-2	musc	1823.9	2.6	-0.08	0.03	0.01	0.01	100.03	180.60	0.40
SAL-4F-2	musc	1827.2	5.5	-0.12	0.07	0.01	0.02	100.09	181.12	0.86
SAL-4F-2	musc	1823.9	4.4	-0.02	0.05	0.01	0.01	99.89	180.60	0.69
SAL-4F-2	musc	1829.9	2.7	-0.08	0.03	-0.01	0.01	100.00	181.55	0.43
SAL-4F-1	musc	1834.4	5.8	0.06	0.07	-0.02	0.02	100.00	182.25	0.91
SAL-4F-1	musc	1815.6	4.5	0.07	0.06	-0.02	0.01	100.01	179.31	0.71
SAL-4F-1	musc	1826.5	3.9	-0.01	0.05	-0.02	0.01	99.94	181.01	0.60
SAL-4F-1	musc	1827.6	3.8	-0.02	0.05	-0.01	0.01	99.97	181.19	0.60
SAL-4F-1	musc	1835.4	4.2	0.02	0.05	0.02	0.01	99.92	182.40	0.66
SAL-4F-1	musc	1818.2	6.8	0.04	0.08	0.00	0.02	100.05	179.72	1.06
SAL-4F-1	musc	1840.0	3.1	0.01	0.04	0.01	0.01	100.02	183.13	0.48
SAL-4F-1	musc	1824.9	4.3	0.00	0.05	-0.01	0.01	99.56	180.77	0.67
SAL-4F-3	musc	1828.2	3.9	0.05	0.05	0.00	0.01	99.76	181.28	0.62
SAL-4F-3	musc	1827.7	2.9	0.03	0.04	0.00	0.01	99.81	181.20	0.46
SAL-4F-3	musc	1826.3	3.1	0.03	0.04	-0.01	0.01	99.86	180.98	0.49
SAL-4F-3	musc	1819.5	3.7	0.00	0.05	0.00	0.01	99.68	179.92	0.57
SAL-4F-3	musc	1841.1	3.1	0.06	0.04	0.00	0.01	99.76	183.30	0.50
SAL-8A-1	musc	1822.6	4.4	-0.14	0.06	0.02	0.01	98.57	180.39	0.69
SAL-8A-1	musc	1834.8	3.6	-0.11	0.04	0.01	0.01	99.60	182.31	0.57
SAL-8A-2	musc	1829.0	4.3	-0.02	0.06	-0.01	0.01	99.33	181.39	0.67
SAL-8A-2	musc	1823.2	4.5	0.05	0.06	0.03	0.01	99.69	180.49	0.70
SAL-8A-2	musc	1817.4	6.7	-0.01	0.09	0.01	0.02	99.20	179.59	1.04
SAL-8A-2	musc	1830.9	4.6	0.09	0.07	0.03	0.02	99.78	181.71	0.73
SAL-8A-2	musc	1832.4	2.7	0.05	0.04	-0.01	0.01	99.83	181.93	0.42
SAL-8A-2	musc	1822.7	7.2	0.14	0.10	-0.02	0.02	99.65	180.42	1.12
SAL-8A-3	musc	1839.7	4.7	-0.09	0.06	-0.02	0.01	99.68	183.09	0.75
SAL-8A-3	musc	1829.3	6.1	-0.07	0.08	0.01	0.02	99.30	181.44	0.96
SAL-8A-3	musc	1835.5	3.4	0.02	0.04	0.00	0.01	99.76	182.42	0.54
SAL-8BC-3	musc	1827.8	4.2	-0.09	0.05	0.00	0.01	99.55	180.82	0.66
SAL-8BC-3	musc	1850.5	7.0	0.09	0.10	-0.03	0.02	99.55	184.40	1.10
SAL-8BC-3	musc	1831.2	5.8	-0.17	0.09	0.00	0.02	99.60	181.36	0.91
SAL-8BC-3	musc	1839.6	4.5	-0.10	0.07	0.02	0.01	99.62	182.68	0.72
SAL-8BC-3	musc	1830.7	4.6	0.06	0.06	0.00	0.01	99.27	181.28	0.72
SAL-8BC-3	musc	1840.8	4.4	-0.10	0.06	0.01	0.01	99.68	182.86	0.69
SAL-8BC-3	musc	1836.1	4.5	-0.09	0.06	-0.01	0.01	99.66	182.12	0.71
SAL-8BD	musc	1836.8	5.0	-0.04	0.07	0.00	0.01	99.04	182.23	0.79
SAL-8BD	musc	1840.6	4.4	0.13	0.06	-0.02	0.01	99.76	182.84	0.69
SAL-8BD	musc	1844.7	4.9	-0.03	0.07	0.00	0.01	99.60	183.48	0.77
SAL-8BD	musc	1840.4	4.4	-0.01	0.06	-0.02	0.01	99.69	182.81	0.69
SAL-8BD	musc	1821.2	4.6	-0.03	0.06	-0.01	0.01	99.35	179.79	0.72

Table 7 (continued)										
SAL-8BC-3	musc	1680.2	10.9	0.24	0.15	0.00	0.03	99.03	158.65	1.57
SAL-8BC-3	musc	1622.5	6.1	-0.31	0.08	-0.02	0.02	99.28	150.45	0.85
SAL-4I-1	musc	1597.8	7.5	0.03	0.11	0.02	0.02	98.54	147.01	1.03
SAL-4I-1	musc	1762.6	6.7	0.25	0.09	0.00	0.02	99.55	170.81	1.01
SAL-4I-1	musc	1839.9	12.1	0.25	0.16	-0.03	0.04	99.60	182.72	1.91
SAL-4I-1	musc	1839.5	8.7	0.06	0.11	-0.03	0.03	99.78	182.67	1.37
SAL-4I-1	musc	1826.1	11.3	0.19	0.13	-0.01	0.03	99.43	180.55	1.77
SAL-4I-1	musc	1812.8	6.4	0.01	0.09	0.00	0.02	99.77	178.49	0.99
SAL-4I-1	musc	1837.6	5.8	0.15	0.07	0.02	0.02	99.65	182.36	0.91
SAL-4I-1	musc	1823.9	6.3	-0.10	0.09	0.02	0.02	99.70	180.21	0.99
SAL-4I-1	musc	1834.1	7.2	-0.03	0.10	0.00	0.02	99.84	181.82	1.13
SAL-4I-2	musc	1837.9	3.8	0.09	0.05	-0.01	0.01	99.75	182.41	0.59
SAL-4I-2	musc	1842.9	6.2	0.26	0.08	-0.03	0.02	99.12	183.20	0.98
SAL-4I-2	musc	1833.6	4.1	-0.10	0.05	0.00	0.01	99.72	181.74	0.65
SAL-4I-2	musc	1838.3	5.8	-0.27	0.08	-0.02	0.02	99.64	182.48	0.91
SAL-4I-2	musc	1831.7	4.4	-0.09	0.05	0.00	0.01	99.75	181.43	0.68
SAL-4E	musc	1825.1	4.2	-0.01	0.05	0.01	0.01	99.62	180.41	0.66
SAL-4E	musc	1831.4	5.6	-0.01	0.07	-0.01	0.01	99.66	181.39	0.88
SAL-4E	musc	1835.4	4.3	-0.04	0.05	0.01	0.01	99.69	182.02	0.68
SAL-4E	bt	1838.0	4.8	-0.08	0.06	-0.02	0.01	99.32	182.42	0.75
SAL-4E	bt	1834.8	4.6	0.01	0.07	0.01	0.01	99.70	181.92	0.72
SAL3B	bt	1806.1	3.5	0.01	0.02	-0.01	0.01	99.71	178.70	0.55
SAL3B	bt	1819.0	4.3	0.01	0.03	0.00	0.01	99.84	180.72	0.67
SAL3B	bt	1814.7	4.7	0.11	0.02	0.00	0.01	99.92	180.03	0.73
SAL3B	bt	1814.1	5.3	-0.01	0.03	0.01	0.02	99.72	179.95	0.83
SAL3B	bt	1810.3	4.8	-0.01	0.03	-0.01	0.01	99.91	179.35	0.75
SAL3B	bt	1755.5	4.8	0.14	0.03	0.03	0.01	99.90	170.94	0.73
SAL3B	bt	1790.8	4.8	0.05	0.03	0.01	0.02	99.84	176.33	0.74
SAL3B	bt	1810.7	4.1	0.01	0.02	-0.01	0.01	99.66	179.42	0.65
SAL3B	bt	1822.1	4.8	0.00	0.03	-0.01	0.01	99.82	181.19	0.75
SAL3B	bt	1813.2	5.5	-0.03	0.03	0.03	0.01	99.67	179.81	0.86
SAL3B	bt	1813.2	4.7	0.02	0.03	-0.03	0.01	99.88	179.80	0.73
SAL3B	bt	1816.5	4.5	-0.03	0.02	-0.03	0.01	99.86	180.33	0.71
SAL3B	bt	1823.6	4.0	-0.03	0.03	0.02	0.01	99.82	181.43	0.63
SAL3B	bt	1741.4	6.0	0.04	0.04	-0.02	0.02	99.74	168.80	0.90
SAL3B	bt	1816.2	4.5	-0.09	0.03	-0.01	0.01	99.85	180.28	0.71
SAL3B	bt	1779.7	7.1	0.12	0.04	-0.03	0.02	99.89	174.61	1.08
SAL3B	bt	1807.3	4.5	0.01	0.03	-0.02	0.01	99.73	178.89	0.71
SAL3B	bt	1821.7	4.6	0.05	0.03	0.00	0.01	99.77	181.14	0.73
SAL3B	bt	1803.0	6.1	0.05	0.03	-0.03	0.02	99.85	178.21	0.95
SAL3B	bt	1815.8	5.0	-0.01	0.03	-0.02	0.01	99.89	180.22	0.79
SAL-4F-3	bt	1835.8	2.3	-0.01	0.03	0.00	0.01	99.89	182.47	0.36
SAL-4F-3	bt	1842.9	2.4	-0.04	0.03	0.00	0.01	99.86	183.60	0.38
SAL-4F-3	bt	1837.7	2.3	-0.03	0.03	0.01	0.01	99.88	182.78	0.36
SAL-4F-3	bt	1833.8	2.6	0.02	0.03	0.01	0.01	99.74	182.16	0.41

Notes: 1Corrected: Isotopic intensities corrected for blank, baseline, radioactivity decay and detector intercalibration, not for interfering reactions. Errors quoted for individual analyses include analytical error only, without interfering reaction or J uncertainties. Ages calculated relative to FCT-1 Fish Canyon Tuff sanidine interlaboratory standard at 28.201+/-0 Ma. musc=muscovite; bt=biotite.

Table 8. LA-ICP-MS analyses of sphalerite from sample SAL-5

Output	Mn (ppm)	Fe (ppm)	Co (ppm)	Ni (ppm)	Cu (ppm)	Zn (ppm)	Ga (ppm)	Ge (ppm)	As (ppm)	Se (ppm)
SPH-UNK - 1	12.68	209.60	53.39	<LOD	10.97	658908.2	0.77	<LOD	<LOD	3.19
SPH-UNK - 2	12.61	199.65	53.41	<LOD	8.99	661474.5	0.63	<LOD	<LOD	3.88
SPH-UNK - 3	8.23	157.44	53.42	<LOD	7.73	659091.7	0.68	<LOD	<LOD	7.95
SPH-UNK - 4	9.38	190.01	52.97	<LOD	25.17	656259.1	0.84	<LOD	<LOD	9.47
SPH-UNK - 5	8.49	142.36	51.23	<LOD	4.84	657447.3	1.22	<LOD	<LOD	4.95
SPH-UNK - 6	14.77	324.53	57.47	<LOD	234.71	657136.2	0.63	0.09	<LOD	12.57
SPH-UNK - 7	13.49	211.19	56.81	<LOD	14.45	657490.3	1.26	<LOD	<LOD	7.12
SPH-UNK - 8	21.02	248.38	58.60	<LOD	130.50	656601.2	1.28	<LOD	<LOD	15.03
SPH-UNK - 9	7.08	246.31	53.32	<LOD	363.92	657880.9	1.07	<LOD	<LOD	6.27
SPH-UNK - 10	9.18	172.47	54.30	0.04	11.48	656293.7	1.19	<LOD	0.13	7.72
SPH-UNK - 11	8.44	163.43	53.98	<LOD	10.16	657991.4	1.17	<LOD	0.13	6.92
SPH-UNK - 12	6.67	138.87	51.88	<LOD	9.43	658883.5	1.51	<LOD	<LOD	4.62
SPH-UNK - 13	2.44	185.20	49.39	<LOD	15.08	658469.1	1.13	<LOD	0.14	2.42
SPH-UNK - 15	15.53	223.28	59.91	0.05	28.33	660805.8	1.07	<LOD	<LOD	5.36
SPH-UNK - 16	13.05	234.81	58.85	<LOD	22.90	662296.5	0.97	<LOD	<LOD	8.57
SPH-UNK - 17	4.64	158.96	52.94	<LOD	7.12	664207.5	1.74	0.09	<LOD	4.99
SPH-UNK - 18	4.62	183.25	49.96	<LOD	6.88	663190.6	0.99	<LOD	<LOD	4.49
SPH-UNK - 19	4.31	163.65	51.07	<LOD	16.60	665533.6	1.12	<LOD	<LOD	7.42
SPH-UNK - 20	4.71	191.38	50.54	<LOD	146.42	665771.8	0.98	<LOD	<LOD	5.78
SPH-UNK - 21	12.02	199.97	54.18	<LOD	7.93	666961.9	0.79	<LOD	0.11	5.89
SPH-UNK - 22	8.92	157.12	53.38	<LOD	6.19	667534.0	1.33	0.13	<LOD	5.88
SPH-UNK - 23	11.57	203.19	55.74	<LOD	10.39	668088.0	1.02	<LOD	<LOD	5.68

	Ag	Cd	In	Sn	Sb	Te	Au	Hg	Pb	Bi
SPH-UNK - 1	5.04	11827.6	0.12	0.09	0.12	<LOD	<LOD	20.98	1.03	<LOD
SPH-UNK - 2	4.74	12113.1	0.17	0.11	<LOD	0.03	<LOD	22.29	0.93	<LOD
SPH-UNK - 3	3.19	12034.2	0.19	0.29	0.08	0.05	<LOD	22.43	0.97	0.01
SPH-UNK - 4	7.06	11794.0	0.10	0.06	<LOD	<LOD	<LOD	23.89	1.56	0.01
SPH-UNK - 5	1.31	11838.1	0.03	0.07	<LOD	<LOD	<LOD	22.96	0.89	0.00
SPH-UNK - 6	10.57	11680.5	0.10	0.05	0.07	<LOD	<LOD	24.10	2.98	0.01
SPH-UNK - 7	6.57	12185.0	0.07	0.05	<LOD	<LOD	<LOD	23.57	0.91	<LOD
SPH-UNK - 8	8.25	12409.1	0.11	0.02	0.03	<LOD	<LOD	24.45	1.18	0.02
SPH-UNK - 9	5.29	11904.4	0.21	0.07	<LOD	<LOD	<LOD	23.27	1.38	0.03
SPH-UNK - 10	9.19	12164.8	0.20	0.09	<LOD	<LOD	<LOD	24.70	1.07	<LOD
SPH-UNK - 11	9.26	12807.1	0.10	0.06	<LOD	0.02	0.00	16.88	0.89	<LOD
SPH-UNK - 12	5.85	11843.4	0.09	0.15	0.05	<LOD	<LOD	17.78	0.78	<LOD
SPH-UNK - 13	1.38	11599.3	0.06	0.16	0.06	<LOD	<LOD	18.19	1.51	0.03
SPH-UNK - 15	10.64	13640.2	0.25	0.27	0.03	<LOD	<LOD	18.88	0.75	<LOD
SPH-UNK - 16	7.32	13348.5	0.07	0.19	<LOD	<LOD	<LOD	18.89	0.74	<LOD
SPH-UNK - 17	2.07	12551.7	0.19	0.12	<LOD	<LOD	<LOD	18.38	0.71	<LOD
SPH-UNK - 18	2.78	12921.4	0.34	0.31	<LOD	<LOD	<LOD	18.50	0.82	<LOD
SPH-UNK - 19	2.13	12860.7	0.17	0.11	0.03	<LOD	<LOD	18.59	0.84	<LOD
SPH-UNK - 20	4.08	13429.7	0.07	0.06	<LOD	<LOD	<LOD	18.25	0.95	0.01
SPH-UNK - 21	4.96	14751.7	0.07	0.10	<LOD	<LOD	<LOD	15.16	0.59	<LOD
SPH-UNK - 22	4.31	14649.0	0.17	0.16	0.05	<LOD	0.00	16.61	0.73	<LOD
SPH-UNK - 23	6.06	14720.3	0.29	0.13	<LOD	<LOD	<LOD	15.81	0.79	<LOD

Notes: <LOD=below detection limits.

Table 9. Sulfur isotope composition of chalcopyrite

Sample	$\delta^{34}S_{V\text{-}CDT}$ (‰)	1σ (‰)
Suph-1-1-Cpy	-10.9	0.3
Suph-1-3-Cpy	-11.3	0.3
Suph-1-5-Cpy	-10.3	0.3
Suph-1-21-Cpy	-10.9	0.3
Suph-1-23-Cpy	-11.1	0.3
Suph-2-2-Cpy	-10.7	0.3
Suph-2-4-Cpy	-11.4	0.3
Suph-2-6-Cpy	-11.4	0.3
Suph-2-8-Cpy	-10.4	0.3
Suph-2-9-Cpy	-10.8	0.3
Suph-2-11-Cpy	-10.3	0.3
Suph-2-13-Cpy	-10.3	0.3
Suph-2-16-Cpy	-10.1	0.3
Suph-2-18-Cpy	-10.3	0.3
Suph-2-20-Cpy	-10.2	0.3
Suph-2-22-Cpy	-11.0	0.3
Suph-2-23-Cpy	-10.3	0.3
Suph-2-25-Cpy	-10.0	0.3
Suph-2-27-Cpy	-10.2	0.3
Suph-2-29-Cpy	-9.8	0.3
Suph-2-31-Cpy	-10.3	0.3
Suph-2-33-Cpy	-10.5	0.3

Notes: Spot-to-spot reproducibility on the chalcopyrite reference material = 0.3‰

Table 10. Oxygen isotopic composition of quartz and calcite, and estimated fluid O isotope compositions, from mineralized veins

Sample	Mineral	$\delta^{18}O_{V\text{-}SMOW}$ (‰)	Reproducibility	$\delta^{18}O_{V\text{-}SMOW}^{fluid\ min}$ (‰)	$\delta^{18}O_{V\text{-}SMOW}^{fluid\ max}$ (‰)
1-Qbl-02	Type I qtz	12.1	0.8		
1-Qbl-04	Type I qtz	11.2	0.8		
1-Qbl-05	Type I qtz	12.0	0.8		
1-Qbk-01	Type II qtz distal	10.2	0.8	2.0	5.4
1-Qbk-02	Type II qtz distal	10.0	0.8	1.8	5.2
1-Qbk-03	Type II qtz distal	9.9	0.8	1.7	5.1
1-Qbk-04	Type II qtz distal	8.9	0.8	0.7	4.1
1-Qbk-05	Type II qtz distal	7.8	0.8	-0.4	3.0
2-Qbk-3	Type II qtz distal	7.9	0.7	-0.3	3.1
2-Qbk-4	Type II qtz distal	8.8	0.7	0.6	4.0
2-Qbk-5	Type II qtz distal	8.1	0.7	-0.1	3.3
2-Qbk-6	Type II qtz distal	10.8	0.7	2.6	6.0
2-Qbk-7	Type II qtz distal	9.9	0.7	1.7	5.1
2-Qbl-18	Type II qtz distal	9.0	0.7	0.8	4.2
2-Qbl-19	Type II qtz distal	9.2	0.7	1.0	4.4
2-Qbl-20	Type II qtz distal	10.6	0.7	2.4	5.8
2-Qbl-22	Type II qtz distal	9.3	0.7	1.1	4.5
2-Qbl-24	Type II qtz distal	8.2	0.7	0.0	3.4
1-Qbk-1	Type II qtz distal	11.5	0.5	3.3	6.7
1-Qbk-2	Type II qtz distal	10.1	0.5	1.9	5.3
1-Qbk-3	Type II qtz distal	10.7	0.5	2.5	5.9
1-Qbk-4	Type II qtz distal	12.4	0.5	4.2	7.6
1-Qbk-5	Type II qtz distal	13.3	0.5	5.1	8.5
1-Qbk-6	Type II qtz distal	12.0	0.5	3.8	7.2
3-Qbk-01	Type II qtz distal	8.9	0.7	0.7	4.1
3-Qbk-02	Type II qtz distal	12.0	0.7	3.8	7.2
3-Qbk-03	Type II qtz distal	12.6	0.7	4.4	7.8
3-Qbk-04	Type II qtz distal	11.5	0.7	3.3	6.7
3-Qbk-05	Type II qtz distal	11.9	0.7	3.7	7.1
Puck4-C5-Qtz-1	Type II qtz adjacent	8.9	0.8	-4.8	0.0
Puck4-C5-Qtz-2	Type II qtz adjacent	7.9	0.8	-5.8	-1.0
Puck4-C5-Qtz-3	Type II qtz adjacent	8.2	0.8	-5.5	-0.7
Puck4-C5-Qtz-4	Type II qtz adjacent	9.4	0.8	-4.3	0.5
Puck4-C5-Qtz-5	Type II qtz adjacent	6.8	0.8	-6.9	-2.1
Puck4-C5-Qtz-6	Type II qtz adjacent	8.5	0.8	-5.2	-0.4
Puck4-C5-Qtz-7	Type II qtz adjacent	8.4	0.8	-5.3	-0.5
Puck4-C5-Qtz-8	Type II qtz adjacent	10.6	0.8	-3.1	1.7
Puck4-C5-Qtz-9	Type II qtz adjacent	8.5	0.8	-5.2	-0.4
Puck4-C5-Qtz-10	Type II qtz adjacent	7.2	0.8	-6.5	-1.7

Table 10 (continued)					
Puck4-C5-Qtz-11	Type II qtz adjacent	8.3	0.8	-5.4	-0.6
Puck4-C5-Qtz-12	Type II qtz adjacent	7.4	0.8	-6.3	-1.5
Puck4-C5-Qtz-13	Type II qtz adjacent	10.2	0.8	-3.5	1.3
Puck4-C5-Qtz-14	Type II qtz adjacent	8.5	0.8	-5.2	-0.4
Puck4-C5-Qtz-15	Type II qtz adjacent	7.2	0.8	-6.5	-1.7
Puck4-C5-Qtz-4a	Type II qtz adjacent	8.7	0.8	-5.0	-0.2
Puck4-C5-Qtz-5a	Type II qtz adjacent	8.4	0.8	-5.3	-0.5
Puck4-C5-Qtz-6a	Type II qtz adjacent	7.7	0.8	-6.0	-1.2
Puck4-C5-Qtz-7a	Type II qtz adjacent	7.3	0.8	-6.4	-1.6
Puck4-C5-Qtz-8a	Type II qtz adjacent	7.9	0.8	-5.8	-1.0
3-Qyl-1	Type III qtz	10.4	0.7	-5.0	-2.4
3-Qyl-2	Type III qtz	10.2	0.7	-5.2	-2.6
3-Qyl-3	Type III qtz	8.2	0.7	-7.2	-4.6
3-Qyl-4	Type III qtz	11.8	0.7	-3.6	-1.0
3-Qyl-5	Type III qtz	10.2	0.7	-5.2	-2.6
3-Qyl-6	Type III qtz	12.6	0.7	-2.8	-0.2
3-Qyl-7	Type III qtz	12.2	0.7	-3.2	-0.6
1-Qyl-1	Type III qtz	9.3	0.5	-6.1	-3.5
1-Qyl-2	Type III qtz	9.7	0.5	-5.7	-3.1
1-Qyl-3	Type III qtz	9.5	0.5	-5.9	-3.3
1-Qyl-4	Type III qtz	12.1	0.5	-3.3	-0.7
1-Qyl-5	Type III qtz	13.3	0.5	-2.1	0.5
1-Qyl-6	Type III qtz	11.4	0.5	-4.0	-1.4
1-Qyl-7	Type III qtz	11.2	0.5	-4.2	-1.6
2-Qy-01	Type III qtz	9.7	0.5	-5.7	-3.1
2-Qy-02	Type III qtz	9.0	0.5	-6.4	-3.8
2-Qy-03	Type III qtz	9.3	0.5	-6.1	-3.5
2-Qy-04	Type III qtz	8.7	0.5	-6.7	-4.1
2-Qy-05	Type III qtz	11.0	0.5	-4.4	-1.8
2-Qy-06	Type III qtz	7.4	0.5	-8.0	-5.4
2-Qy-07	Type III qtz	8.6	0.5	-6.8	-4.2
2-Qy-08	Type III qtz	7.4	0.5	-8.0	-5.4
2-Qy-09	Type III qtz	11.3	0.5	-4.1	-1.5
2-Qy-10	Type III qtz	8.2	0.5	-7.2	-4.6
1-Qyl-01	Type III qtz	9.8	0.5	-5.6	-3.0
1-Qyl-04	Type III qtz	9.6	0.5	-5.8	-3.2
1-Qyl-02	Type IV qtz	10.3	0.5		
1-Qyl-03	Type IV qtz	11.3	0.5		
1-Qyl-05	Type IV qtz	12.0	0.5		
1-Qbl-01	Type IV qtz	12.5	0.5		
1-Qbl-02	Type IV qtz	12.2	0.5		

Table 10 (continued)					
1-Qbl-03	Type IV qtz	12.3	0.5		
1-Qbl-04	Type IV qtz	12.8	0.5		
1-Qbl-05	Type IV qtz	13.7	0.5		
1-Qbl-06	Type IV qtz	14.0	0.5		
1-Qbl-07	Type IV qtz	12.9	0.5		
1-Qbl-08	Type IV qtz	13.3	0.5		
3-Qbl-01	Type IV qtz	13.3	0.7		
3-Qbl-02	Type IV qtz	12.3	0.7		
3-Qbl-03	Type IV qtz	12.0	0.7		
3-Qbl-05	Type IV qtz	13.9	0.7		
3-Qbl-06	Type IV qtz	15.3	0.7		
Puck4-C5-Crb-1	calcite	7.6	0.7	0.3	-3.5
Puck4-C5-Crb-2	calcite	6.0	0.7	-1.3	-5.1
Puck4-C5-Crb-3	calcite	6.4	0.7	-0.9	-4.7
Puck4-C5-Crb-4	calcite	8.0	0.7	0.7	-3.1
Puck4-C5-Crb-5	calcite	7.5	0.7	0.2	-3.6
Puck4-C5-Crb-6	calcite	5.0	0.7	-2.3	-6.1
Puck4-C5-Crb-7	calcite	8.7	0.7	1.4	-2.4
Puck4-C5-Crb-8	calcite	4.9	0.7	-2.4	-6.2
Puck4-C5-Crb-9	calcite	5.0	0.7	-2.3	-6.1
Puck4-C5-Crb-10	calcite	9.8	0.7	2.5	-1.3
Puck4-C5-Crb-11	calcite	7.5	0.7	0.2	-3.6
Puck4-C5-Crb-12	calcite	5.3	0.7	-2.0	-5.8
Puck4-C5-Crb-13	calcite	5.9	0.7	-1.4	-5.2
Puck4-C5-Crb-14	calcite	5.2	0.7	-2.1	-5.9
Puck4-C5-Crb-15	calcite	7.0	0.7	-0.3	-4.1
Puck4-C5-Crb-2a	calcite	7.6	0.7	0.3	-3.5
Puck4-C5-Crb-3a	calcite	6.3	0.7	-1.0	-4.8
Puck4-C5-Crb-4a	calcite	4.7	0.7	-2.6	-6.4
Puck4-C5-Crb-5a	calcite	7.6	0.7	0.3	-3.5
Puck4-C5-Crb-7a	calcite	7.6	0.7	0.3	-3.5
Puck4-C5-Crb-8a	calcite	9.5	0.7	2.2	-1.6
Puck4-C5-Crb-9a	calcite	8.4	0.7	1.1	-2.7
Puck4-C5-Crb-11a	calcite	6.0	0.7	-1.3	-5.1

Notes: proximal/distal to cal = calcite; qtz = quartz; min = minimum calculated value; max = maximum calculated value.